UNITED NATIONS UNIVERSITY
GEOTHERMAL TRAINING PROGRAMME

ORKUSTOFNUN

Öskurhóll, Hveravellir at Kjölur

Manuel Alejandro Rivera Ayala

COUPLED GEOTHERMAL RESERVOIR-WELLBORE SIMULATION WITH A CASE STUDY FOR THE NÁMAFJALL FIELD, N-ICELAND

Report 2
December 2010

UNITED NATIONS UNIVERSITY
GEOTHERMAL TRAINING PROGRAMME
Orkustofnun, Grensásvegur 9,
IS-108 Reykjavík, Iceland

Reports 2010
Number 2

COUPLED GEOTHERMAL RESERVOIR-WELLBORE SIMULATION WITH A CASE STUDY FOR THE NÁMAFJALL FIELD, N-ICELAND

MSc thesis
School of Engineering and Natural Sciences
Faculty of Mechanical Engineering
University of Iceland

by

Manuel Alejandro Rivera Ayala
LaGeo S.A de C.V.
15 Av. Sur, Colonia Utila
Santa Tecla, La Libertad
EL SALVADOR
marivera@lageo.com.sv

United Nations University
Geothermal Training Programme
Reykjavík, Iceland
Published in December 2010

ISBN 978-9979-68-284-4
ISSN 1670-7427

This MSc thesis has also been published in March 2010 by the
School of Engineering and Natural Sciences, Faculty of Mechanical Engineering
University of Iceland

INTRODUCTION

The Geothermal Training Programme of the United Nations University (UNU) has operated in Iceland since 1979 with six month annual courses for professionals from developing countries. The aim is to assist developing countries with significant geothermal potential to build up groups of specialists that cover most aspects of geothermal exploration and development. During 1979-2010, 452 scientists and engineers from 47 countries have completed the six month courses. They have come from Asia (42%), Africa (29%), Central America (15%), and Central and Eastern Europe (14%). There is a steady flow of requests from all over the world for the six month training and we can only meet a portion of the requests. Most of the trainees are awarded UNU Fellowships financed by the UNU and the Government of Iceland.

Candidates for the six month specialized training must have at least a BSc degree and a minimum of one year practical experience in geothermal work in their home countries prior to the training. Many of our trainees have already completed their MSc or PhD degrees when they come to Iceland, but several excellent students who have only BSc degrees have made requests to come again to Iceland for a higher academic degree. In 1999, it was decided to start admitting UNU Fellows to continue their studies and study for MSc degrees in geothermal science or engineering in co-operation with the University of Iceland. An agreement to this effect was signed with the University of Iceland. The six month studies at the UNU Geothermal Training Programme form a part of the graduate programme.

It is a pleasure to introduce the 22nd UNU Fellow to complete the MSc studies at the University of Iceland under the co-operation agreement. Mr. Manuel A. Rivera, BSc in Mechanical and Electrical Engineering, of LaGeo S.A de C.V., El Salvador completed the six month specialized training in Geothermal Utilization at the UNU Geothermal Training Programme in October 2007. His research report was entitled: "Design considerations for reliable electrical, control and instrumentation systems in geothermal power plants with emphasis on hydrogen sulphide related problems". After a year of geothermal research work in El Salvador, he came back to Iceland for MSc studies in Reservoir Engineering at the Faculty of Mechanical Engineering of the University of Iceland in August 2008. In March 2010, he defended his MSc thesis presented here, entitled "Coupled geothermal reservoir-wellbore simulation with a case study for the Námafjall field, N-Iceland". His studies in Iceland were financed by the Government of Iceland through a UNU-GTP Fellowship from the UNU Geothermal Training Programme. We congratulate him on his achievements and wish him all the best for the future. We thank the Faculty of Mechanical Engineering at the School of Engineering and Natural Sciences of the University of Iceland for the co-operation, and his supervisors for the dedication.

Finally, I would like to mention that Manuel´s MSc thesis with the figures in colour is available for downloading on our website *www.unugtp.is* under publications.

With warmest wishes from Iceland,

Ingvar B. Fridleifsson, director
United Nations University
Geothermal Training Programme

ACKNOWLEDGEMENT

I would like to express my gratitude to the beautiful country of Iceland and the United Nations University Geothermal Training Programme (UNU-GTP) through its Director Dr. Ingvar B. Fridleifsson for funding my Master's studies at the University of Iceland. I feel deeply thankful for the fine education and training I have received during this time.

I would also like to thank my supervisors Dr. Gudni Axelsson and Dr. Halldór Pálsson for their wise guidance, support and patience, as well as for the encouragement throughout the project. I extend my gratitude to Ms. Saeunn Halldórsdóttir and Mr. Hédinn Björnsson for providing me with data and useful information, as well as for their useful comments and suggestions along the project.

I wish to thank the people at UNU-GTP: Mr. Lúdvík S. Georgsson, Ms. Thórhildur Ísberg, Ms. Dorthe Holm and Mr. Markús A.G. Wilde for their enthusiastic help and support during this period.

My gratitude goes to Landsvirkjun for allowing me to use the data on the Námafjall geothermal field. Also I want to thank Dr. Andri Arnaldsson for his help with the pre- and post-processing Linux Shell scripts.

Finally, I want to thank my employer LaGeo S.A de C.V. in El Salvador for allowing me to receive the UNU-GTP scholarship under such favourable conditions.

ABSTRACT

A distributed-parameter numerical model of the Námafjall-Bjarnarflag geothermal reservoir has been developed. Instead of following the most common approach of modeling the wellbores as constant wellbottom pressure sinks, they are modeled as variable wellbottom pressure sinks, with constant wellhead pressure, through the use of coupled reservoir-wellbore simulation. The purpose of the work is to study the efficiency of this kind of coupling and to predict the reservoir response to three different exploitation scenarios: 40 MWe, 60 MWe and 90 MWe. The flow of mass and heat in the reservoir is modeled through the theory of non-isothermal multiphase flow in porous media implemented by the TOUGH2 code, and an inverse estimation of reservoir parameters is made through the use of automatic parameter estimation capabilities available in the iTOUGH2 code, using a least-squares objective function and the Levenberg-Marquardt minimization algorithm. The HOLA wellbore simulator is used to model the flow within the wells, and the pre- and post-processing tools were based on Linux Shell scripts using freely available software. The automatic parameter estimation was found very useful in finding a set of parameters which produced a reasonable match with available field data for both the natural state and the production response data. The model derived can be regarded as almost closed, and hence pessimistic since the natural fluid recharge into the reservoir is only 14% to 25% of the extracted mass. For the 90 MWe scenario, simulations predict extended boiling throughout the reservoir, pressure drawdown values close to 44 bar and cooling of 35 to 40 C around the wells. An average decline rate in electrical output of 7.55 MW/yr is expected and by year 2045, 30 wells will be required to maintain 90 MW electrical production. Differences between 15% and 20% were found in the reservoir electrical output if variations in well bottomhole pressures are taken into account through the use of coupled reservoir-wellbore simulation. The coupling method employed in this work is relatively simple and computationally inexpensive, but has the disadvantage that only single feedzone wells can be modeled.

TABLE OF CONTENTS

LIST OF FIGURES

LIST OF TABLES

NOMENCLATURE

C_{zz}	Covariance matrix of measurement errors
F^h	Heat flux (J/m^2·s)
F^w	Mass flux of water (kg/ m^2·s)
g	Gravitational acceleration (m/s)
g_k	Gradient of the objective function at iteration k
H	Hessian matrix
n	Normal unit vector (-)
r	Residuals vector
u	Darcy velocity (m/s)
$\dot{m}\_$	Mass flowrate (kg/s)
Γ	Surface area (m2)
λ	Thermal conductivity (W/m·°C) or Levenberg parameter (-)
μ	Dynamic viscosity (kg/m·s)
v	Marquardt parameter (-)
φ	Rock porosity (-)
ρ	Density (kg/m^3)
σ_{zj}^2	Variance of measurement error in observation zj
A	Area (m^2)
C	Specific heat (J/kg·°C)
D	Distance (m)
E	Energy per unit volume (J/m^3)
E_ρ	Total energy ux in a well (J/s)
h	Enthalpy (J/kg)
k	Absolute permeability (m^2)
k_r	Relative permeability (-)
M	Specific mass (kg/m^3)
P	Pressure (Pa)
p_n^*	Prior information of parameter n (permeability, porosity, etc.)
p_n	Estimated value of parameter n
P_r	Reservoir pressure (Pa)
P_{wb}	Wellbottom pressure at feedzone (Pa)
PI	Productivity index (m^3)
q	Mass flowrate (kg/s)
q^h	Heat generation (J/m^3·s)
q^w	Mass generation (kg/s)
R	Residual (kg/m^3 or J/m^3 or kg/s)
r_e	Effective radius (m)
r_w	Well radius (m)
S	Saturation (m^3/m^3) or objective function
T	Temperature (°C)
t	Time (s)
u	Speci_c internal energy (J/kg)
V	Volume (m^3)
z	Vertical coordinate (m)
z_m^*	Measured value of observable variable m (pressure, temperature, etc.)
z_m	Estimated value of observable variable m

1. INTRODUCTION

Geothermics is a very eclectic discipline that makes use of diverse areas of science from the early stages of exploration to production and management: geology, geochemistry, geophysics, drilling engineering, reservoir engineering all provide tools and criteria that aid in the characterization and optimal use of geothermal resources. One such tool used by reservoir engineers is numerical modeling, simulating the flow of mass and heat within a reservoir.

Detailed numerical models, sometimes called distributed-parameter models in the literature, of geothermal reservoirs have become a standard tool used as an important input to the development and exploitation strategy in the geothermal industry (O'Sullivan et al., 2001). Some of the key questions about the reservoir management to which a good numerical model can provide useful guidance are (Bödvarsson and Witherspoon, 1989):

- What is the generating capacity of the field?
- What well spacing should be used to minimize well interference and how fast will the production rates decline?
- How will the average enthalpy change due to boiling or inflow of cooler fluids?
- How many replacement wells will have to be drilled to sustain plant capacity?
- How will reinjection affect well performance, where should the reinjection wells be located and how should they be completed?

Experience with these models in recent years has demonstrated that predictions about the reservoir response to exploitation can be produced that match with a reasonable accuracy the observed response. Nevertheless, setting up a model requires considerable amounts of data from different disciplines, from geology, geochemistry to geophysics and reservoir engineering. Therefore, the "art" of computer modeling involves the synthesis of conflicting opinions, interpretation and extrapolation of data to set up a coherent and sensible conceptual model that can be developed into a computer model (O'Sullivan et al., 2001).

According to O'Sullivan et al. (2001) the creation of geothermal reservoir simulators started in the 1980's, both in the public and private sectors. The computer power available at the time forced the models to have significant limitations: some of them were 1D or 2D models, or some assumed radial symmetry in order to limit the number of discretization cells in the domain, but still the models were able to provide useful information about the reservoir response. As the computer power available increased in the following two decades, the models increased in complexity and left behind some of the previous limitations in the number of elements. Nowadays, even standard off-the-shelf desktop computers provide enough computing power to operate a 3D model with a relatively large number of cells and even to perform inverse parameter estimation with the use of observed field data. Furthermore, the increasing availability of parallel computing clusters has made it possible to include a very large number of parameters in the inverse models and to obtain results in a relatively short time.

In these models, geothermal wells are mathematically represented using a deliverability model, in which the force driving the fluid from the reservoir into the wellbore is related the pressure difference between them. To our knowledge, most of the numerical models created up to date assume that the wellbottom pressure remains constant in time, but the physics involved state that this approximation may not be applicable in two phase fields. It can be hypothesized that the wellbore response in terms of enthalpy, flow rate and pressure drawdown can be simulated with greater adherence to the physical laws governing the fluid flow, therefore expecting a greater accuracy in the modeled wellbore production response. The goal of this work is to explore and compare the differences between the two types of models using real data from an actual Icelandic geothermal field. Modeling the changes of the wellbottom pressure in time requires the use of a wellbore simulator.

The simulations of the non-isothermal, two phase flow within the reservoir are made with the iTOUGH2 code (Finsterle, 2007), using its inverse parameter estimation capabilities, and the wellbore simulator used is HOLA (Aunzo et al., 1991). The pre- and post-processing of data was made with

Linux Shell scripts, some of them belonging to a collection of scripts created by Andri Arnaldsson at Vatnaskil Consulting for Reykjavík Energy.

Chapter 1 contains a general introduction to the work. The second chapter of the thesis presents the theory underlying the simulators used, from the non-isothermal transport of multiphase flow in porous media, the deliverability model, to the flow inside the wellbore and the theory of inverse modeling, with particular reference to the algorithms used.

Chapter 3 presents a case study for the Námafjall geothermal field in North Iceland. A review of the available geological, geophysical, geochemical, drilling and exploitation data is presented in the "Review of available data" section and synthesized into a conceptual model of the field. The "Numerical model" section describes the details of the model created in the natural state, history match and forecast stages. The outcome of the simulations in presented and discussed in the "Analysis of results" section . Finally, the overall findings of the work and recommendations are presented in the "Conclusions" chapter.

2. THEORETICAL BACKGROUND

In the following paragraphs the physical theory and numerical techniques implemented in the simulators TOUGH2, iTOUGH2 and HOLA used in this work are presented, as explained by their authors Pruess et al. (1999), Finsterle (2007) and Björnsson (1987) respectively.

2.1 Forward model

2.1.1 Non-isothermal flow in porous media

The flow in a geothermal reservoir is a problem of non-isothermal, multiphase flow through porous media. The so called forward model calculates the reservoir thermodynamic conditions based on a fixed set of parameters given by the modeler. Assuming a single component (pure water) and neglecting diffusion transport mechanism and capillary pressure, the basic equations solved by the TOUGH2 simulator used in this work are a mass and energy balance for each discrete element in the reservoir domain. In the following paragraphs these equations of the integral finite differences, or finite volume method are presented.

The mass balance in an arbitrary sub-domain with volume V_n and surface area Γ_n can be written as:

$$\frac{d}{dt}\int MdV = \int_{Vn} \mathbf{F}^w \cdot \mathbf{n} d\Gamma_n + \int_{Vn} q^w dV_n \tag{1}$$

where **F** is the mass flux through the surface element $d\Gamma_n$ and **n** is a normal vector pointing inwards on this surface element; *q* represents the mass generation inside the volume (sinks and sources). The superscript *w* stands for "water" and is used to make a distinction from the heat fluxes and heat sources presented later.

The mass accumulation term has the form:

$$M = \phi \sum_{\beta} S_\beta \rho_\beta \tag{2}$$

The sum is done for all phases (β: liquid, gas); φ is the rock porosity and ϱ is density of phase β. *S* is the saturation of phase β, and is defined as the faction of void volume in the element occupied by a given phase:

$$S_\beta = \frac{V_\beta}{V_{void}} = \frac{V_\beta}{\phi V_n} \tag{3}$$

The advective mass flow vector is the sum of the individual fluxes of both phases:

$$\mathbf{F}^w_{adv} = \sum_{\beta} \mathbf{F}^w_\beta \tag{4}$$

Where the individual phase flux is given by the multiphase version of Darcy's law:

$$\mathbf{F}^w_\beta = \rho_\beta \mathbf{u}_\beta = -k \frac{k_{r\beta}\rho_\beta}{\mu_\beta}(\nabla P + \rho_\beta \mathbf{g}) \tag{5}$$

The $\mathbf{u}_\beta$ term is the Darcy velocity vector, *k* is the absolute permeability of the volume and *P* is fluid pressure; $k_{r\beta}$ is the relative permeability of phase β, which is used to represent the reduction of the effective permeability relative to single phase conditions experienced by each of the flowing phases due to the fact that they are sharing the available pore space. The relative permeability is regarded to be a function of the liquid phase saturation (Pruess, 2002). In simpler terms, it is a way to represent how both phases, liquid and gas, split among them the available absolute permeability in the porous

medium. μ is the dynamic viscosity and ***g*** is the vector of gravitational acceleration, defined to be positive in the positive *z* direction. In the literature, the relative permeability, density and dynamic viscosity are sometimes grouped into a single term called the mobility of phase β.

The energy balance equation has a quite similar shape as the mass balance. Neglecting radiation heat transfer it can be written as:

$$\frac{d}{dt}\int_{Vn} E dV_n = \int_{\Gamma_n} \mathbf{F}^h \cdot \mathbf{n} d\Gamma_n + \int_{Vn} q^h dV_n \tag{6}$$

Here, E is the energy per unit mass contained in volume V_n, and the superscript *h* denotes "heat".

The energy accumulation term has the form:

$$E = (1-\phi)\rho_R C_R T + \phi \sum_\beta S_\beta \rho_\beta u_\beta \tag{7}$$

Where ρ_R and C_R are the rock density and specific heat, respectively, and u_β is the specific internal energy of phase β.

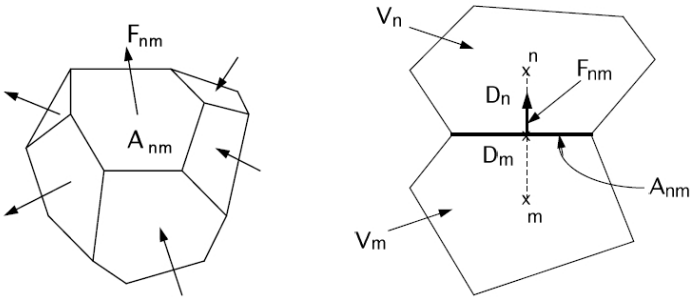

FIGURE 1: Space discretization and geometry data in the integral finite difference method (Pruess et al., 1999).

The heat flux vector contains both conductive and advective fluxes:

$$\mathbf{F}^h = -\lambda \nabla T + \sum_\beta h_\beta \mathbf{F}_\beta^w \tag{8}$$

Where λ is the formation thermal conductivity under fully liquid-saturated conditions, *T* is temperature and h is enthalpy. $\mathbf{F}^w$ is the advective mass flow described previously.

2.1.2 Space and time discretization

Due to the significant commonalities between the mass and heat balance equations, we will let *M* denote either mass or energy content per unit volume. The accumulation term in equation 1 is discretized as:

$$\int_{Vn} M dV = V_n M_n \tag{9}$$

where M_n is the average of the property (i.e. specific mass or energy) inside volume . The surface integral term can be approximated as a discrete sum of averages over the *m* surface segments enclosing element *n* (Figure 1):

$$\int_{\Gamma_n} \mathbf{F}^\kappa \cdot \mathbf{n} d\Gamma = \sum_m A_{nm} F_{nm} \tag{10}$$

Where is the average flux from element m into element *n* perpendicularly crossing surface. The κ (kappa) superscript is used to distinguish between mass (of water, *w*) and heat (*h*) fluxes.
Combining the two equations above into the balance equation we get:

$$\frac{d}{dt} M_n^\kappa = \frac{1}{V_n} \sum_m A_{nm} F_{nm}^\kappa + q_n^\kappa \tag{11}$$

The Darcy flux term is discretized as:

$$F_{\beta,nm} = -k_{nm} \left[\frac{k_{r\beta}\rho_\beta}{\mu_\beta} \right]_{nm} \left[\frac{P_n - P_m}{D_{nm}} - \rho_{\beta,nm} g_{nm} \right] \tag{12}$$

Where subindex β distinguishes between the liquid and gas phases, while subindex *nm* denotes a suitable average between the *m* and *n* elements, like interpolation, harmonic weighting, or upstream weighting as used in this work.

The time discretization is made using a fully implicit method, since it provides the numerical stability required for an efficient calculation of multiphase flow (Pruess, 1999). In this method, the right hand side of equation 11 is expressed in terms of the unknown thermodynamic conditions at time step *k*+1:

$$R_n^{\kappa,k+1} = M_n^{\kappa,k} - \frac{\Delta t}{V_n}\left[\sum_m A_{nm} F_{nm}^{\kappa,k+1} + V_n q_n^{\kappa,k+1}\right] = 0 \tag{13}$$

where the residual for each volume element R_n has been introduced. This system of equations is solved by a Newton-Raphson iteration, implemented as follows:

At time step *k*+1 and Newton-Raphson iteration *p*, a linear Taylor expansion can be used to approximate the residuals at iteration *p*+1:

$$R_n^{\kappa,k+1}(x_{i,p+1}) = R_n^{\kappa,k+1}(x_{i,p}) + \sum_i \left.\frac{\partial R_n^{\kappa,k+1}}{\partial x_i}\right|_p (x_{i,p+1} - x_{i,p}) = 0 \tag{14}$$

where $x_{i,p}$ stores the value of the independent primary variable *i* at iteration *p* (x_i: pressure, temperature).

Then,
$$-\sum_i \left.\frac{\partial R_n^{\kappa,k+1}}{\partial x_i}\right|_p (x_{i,p+1} - x_{i,p}) = 0 \tag{15}$$

All the terms $\frac{\partial R_n}{\partial x_i}$ of the so-called Jacobian matrix are evaluated by numerical differentiation. The iteration is continued until the residuals are reduced below a specified convergence tolerance.

In iTOUGH2, a relative convergence criterion is used:

$$\left|\frac{R_{n,p+1}^{\kappa,k+1}}{M_{n,p+1}^{\kappa,k+1}}\right| \le \varepsilon_1 \tag{16}$$

The default value of this tolerance is $\varepsilon_1 \le 1\text{x}10^{-5}$. If the accumulation terms are smaller than ε_2, which has a default value of 1, the convergence criterion imposed is:

$$\left|R_n^{\kappa,k+1}\right| \le \varepsilon_1 \cdot \varepsilon_2 \tag{17}$$

The default Lanczos-type conjugate gradient squared (CGS) solver with incomplete LU factorization preconditioning was used to solve the linear equation system.

2.1.3 The deliverability model

The equations above describe the mass and heat flow throughout the reservoir. Now, to describe the flow from the porous reservoir into any particular sink we can use the deliverability model, which calculates the flow of individual phases as:

$$q_\beta = \frac{k_{r\beta}\rho_\beta}{\mu_\beta} \times PI \times (P_r - P_{wb}) \tag{18}$$

where P_r is the reservoir pressure at the element where the sink is located and P_{wb} is the pressure inside

the sink (e.g., pressure inside the well at the feedzone depth, or wellbottom pressure). *PI* is the productivity index of the feedzone, defined as:

$$PI_l = \frac{2\pi k \Delta z_l}{\ln(\frac{r_e}{r_w}) + s - 0.5} \tag{19}$$

A geothermal well may, and usually has, two or more individual feedzones, each having its own productivity index. Here, the product $k\Delta z$ is known as the permeability-thickness product in layer l, which can be estimated through injection or other pressure transient tests, r_w is the well radius and s the skin factor. r_e is the grid block radius, but if the block is not cylindrical, the equivalent effective radius can be approximated as:

$$r_e = \sqrt{\frac{A}{\pi}} \tag{20}$$

where $A=\Delta x \Delta y$ for an areal cartesian grid.

In general, the simulation of well behaviour in geothermal reservoir modeling can be made in three ways:

- Declaring a fixed flowrate: This flowrate is withdrawn from the sink regardless of reservoir pressure. It is the simplest method, but it cannot reproduce changes in production with time due to changes in reservoir pressure commonly observed in geothermal wells unless the declared flowrate is manually changed.
- Specifying a constant wellbottom pressure and a productivity index in the deliverability model: It reproduces the flowrate changes in time due to the change in reservoir pressures, but assumes that the wellbottom pressure does not change.
- Specifying a constant wellhead pressure and a productivity index: This method is in theory more accurate than the previous for the simulation of geothermal wells; the wellhead pressure is fixed at some value and a wellbore simulator is used to calculate pressure and temperature along the length of the well. This method takes into account the wellbottom pressure changes experienced in geothermal wells due to different reasons: change in the water level in the wellbore, change in the steam/liquid mass fractions (often called dryness) of the extracted fluid, change in the well flowrate, etc. It becomes very useful in forecasting models, since in theory it should help predicting more accurately the discharge rate of each well and its power output.

2.1.4 Flow within the wellbore

The only part that remains to be described is the flow inside the wellbore itself. In this work we used the HOLA wellbore simulator by Aunzo et al. (1991), which is a modification of a code originally created by Björnsson (1987). The basic equations solved are (Björnsson, 1987):
Mass balance:

$$\frac{d\dot{m}}{dz} = 0 \tag{21}$$

Where $\dot{m}$ is the mass flowrate within the well. The momentum balance calculates the pressure gradient taking into consideration the pressure losses due to wall friction, fluid acceleration and change in gravitational load over a differential well length dz:

$$\frac{dP}{dz} - \left(\frac{dP}{dz}\right)_{fri} + \left(\frac{dP}{dz}\right)_{acc} + \left(\frac{dP}{dz}\right)_{pot} = 0 \tag{22}$$

The energy balance is denoted by:

$$\frac{dE_t}{dz} \pm Q = 0 \tag{23}$$

Where Q denotes the ambient heat loss over a unit distance. E_t is the total energy flux in the well and includes enthalpy, kinetic and potential energy. For further details on the equations solved by the HOLA wellbore simulator refer to Björnsson (1987).

In this application, the simulator is given a required wellhead pressure, enthalpy, reservoir pressure and productivity index at the feedzone, and wellbore geometry and roughness of the casings and liners. The simulator then calculates the flowrate inside the wellbore and the wellbottom pressure that satisfy the above equations. Additionally, the temperature profile and thermal parameters of the surrounding rock can be given in order to take into account the conductive heat losses.

2.1.5 Coupled reservoir-wellbore simulation

Now, the question is how to couple the two different simulators, the reservoir simulator and the wellbore simulator. The first option is a direct coupling, in which the reservoir simulator calculates the pressure and enthalpy at the wellbore element and an explicit call is made to the wellbore simulator in each timestep and for each well to calculate the mass flow rate at a given wellhead pressure. The calculated mass flow rate is then used as the mass generation of the subsequent time step and so forth (Tokita et al., 2005).

The second approach is an indirect coupling: the wellbore simulator is run in advance to calculate bottomhole pressures for different combinations of well flow rates and flowing enthalpies. The results are stored in a wellbore table which is fed into the reservoir simulator. Several tables can be provided for different well designs and wellhead pressures. Starting from some initial guess for the flow rate, the reservoir simulator then iterates for the flow rate to calculate the one that satisfies the equation:

$$R(q) = q - \sum_{\beta} \frac{k_{r\beta}\rho_{\beta}}{\mu_{\beta}} \times PI \times \left(P_r - P_{wb}\right) = 0 \tag{24}$$

where q is the wellbore flow rate for a particular time step. An iterative solver is used to find the solution, where in each iteration the reservoir simulator performs a tabular interpolation in the wellbore table supplied. In the case of the TOUGH2 simulator, a Newton-Raphson method is used as solver.

Tokita et al. (2005) suggest that the advantages of the indirect coupling are a faster execution than the direct coupling because of the use of precalculated values, as well as less convergence difficulties. On the negative side, the indirect coupling through wellbore tables is for now limited to wells with a single feedzone (Pruess et al., 1999). On the other hand, the direct coupling has the advantage of greater accuracy since the well flow rate is calculated for the exact reservoir conditions, not the product of an interpolation as in the indirect case, as well as the possibility to model several feedzones in the wellbores. The disadvantages are that it requires modifications to be made to the reservoir simulator, and probably to the wellbore simulator too, to make the coupling, and that convergence difficulties are introduced in the reservoir simulator. In this work the indirect coupling through wellbore tables will be used.

2.2 Inverse parameter estimation

2.2.1 Objective function and covariance matrix

Inverse modeling consist of estimating the parameters of the forward model described previously, from measurements in the reservoir made at discrete points in space and time. Automatic model calibration can be formulated as an optimization problem, which has to be solved in the presence of uncertainty because the available observations are incomplete and exhibit random measurement errors (Finsterle, 2007).

The parameter vector $\boldsymbol{p}$ of lenght n contains the TOUGH2 input parameters to be estimated by inverse

modeling. These parameters may represent hydrogeologic characteristics, thermal properties, initial or boundary conditions of the model.

An observations vector contains the data measured at the calibration points $z^*_{n+1},...,z^*_m$ for the variables we want to match (temperature, pressure, enthalpy, etc.). This vector can also contain, if available, prior information consisting of independently measured or guessed parameter values ($p^*_1,...,p^*_n$) used to constrain the parameters to be estimated:

$$\mathbf{z}^{*T} = \left[p^*_1,...,p^*_n,z^*_{n+1},...,z^*_m\right] \tag{25}$$

Differences between measured parameter values (prior information) and the corresponding estimates are treated in the same manner as the differences between the observed and calculated system state.
The observed data points and prior information stored in vector *z** are measurements that have been made with some instrument which has a certain accuracy; a reasonable assumption about these measurements would be that the measurement errors are uncorrelated, normally distributed random variables with mean zero. The a priori distributional assumption about the residuals can be summarized in a covariance matrix *Czz*, an *m*×*m* diagonal matrix in which the j^{th} diagonal element stores the variance representing the measurement error of observation z^*_j:

$$\mathbf{C}_{zz} = \begin{bmatrix} \sigma^2_{z1} & 0 & 0 & 0 & \cdots & 0 \\ 0 & \sigma^2_{z2} & 0 & 0 & \cdots & 0 \\ 0 & 0 & \sigma^2_{zn} & 0 & \cdots & 0 \\ 0 & 0 & 0 & \sigma^2_{zj} & \cdots & 0 \\ \vdots & \vdots & \vdots & \vdots & \ddots & \vdots \\ 0 & 0 & 0 & 0 & \cdots & \sigma^2_{zm} \end{bmatrix} \tag{26}$$

This observation covariance matrix is used to scale data of different quality, so that an accurate measurement is weighted higher in the inversion than a poor or highly uncertain measurement. It contains the data used to scale observations with different units (e.g. Pascals vs. Â°C) in a way that they can be unitless and comparable. Additionally, it is used to weigh the fitting errors (Finsterle, 2007).

In the same way that observed data is stored in vector *z**, the corresponding model output is stored in vector *z*:

$$\mathbf{z}(\mathbf{p})^T = [p_1,..., p_n, z_{n+1},..., z_m] \tag{27}$$

The residuals vector is the difference between observed and calculated system response:

$$\mathbf{r} = (\mathbf{z}^* - \mathbf{z}(\mathbf{p})) \tag{28}$$

In order to have a measure of the difference or misfit between the model and the observed data, an objective function is defined. The purpose of the optimization algorithm is to find a set of parameters by which this difference between model response and observation is minimized, effectively by minimizing the value of this objective function.

As mentioned before, we are assuming that the measurement errors are uncorrelated and normally distributed with mean zero and covariance matrix *Czz*, which is valid only if sufficient number of data points exist. In this case, minimizing a least squares objective function *S* would lead to finding the set of parameters which is most likely to have produced the observed data, or maximum likelihood estimates:

$$S = \mathbf{r}^T \mathbf{C}^{-1}_{zz} \mathbf{r} \tag{29}$$

or in an equivalent form, the objective function is the sum of the squared residuals weighted by the

inverse of the a-priori variances σ_i^2 contained in the covariance matrix:

$$S = \sum_{i=1}^{m} \frac{r_i^2}{\sigma_{zi}^2} \tag{30}$$

2.2.2 Minimization algorithm

Even though the iTOUGH2 code used in this work has several options for the minimization algorithm, we chose to use the default Levenberg-Marquardt algrithm, which has been found to perform well for most iTOUGH2 applications (Finsterle, 2007).

This method is iterative, i.e., starts with an initial parameter set, and an update vector is calculated at each iteration. A step is successful if the new parameter set at iteration (k+1), $\mathbf{p}_{k+1} = \mathbf{p}_k + \Delta\mathbf{p}_k$ leads to a reduction in the objective function $S(\mathbf{p}_{k+1}) < S(\mathbf{p}_k)$.

The Levenberg-Marquardt method is an improved version of the Gauss-Newton method; both of them belong to a family of methods based on a quadratic approximation of the objective function S. Using a Taylor-series expansion of S, the quadratic approximation is:

$$S(\mathbf{p}_{k+1}) \approx S(\mathbf{p}_k) + \mathbf{g}_k^T \Delta\mathbf{p}_k + \tfrac{1}{2}\Delta\mathbf{p}_k^T \mathbf{H}_k \Delta\mathbf{p}_k \tag{31}$$

The minimum of the objective function in equation 31 is obtained if $\Delta\mathbf{p}_k$ minimizes the quadratic function:

$$\Phi(\Delta\mathbf{p}) = \mathbf{g}_k^T \Delta\mathbf{p}_k + \tfrac{1}{2}\Delta\mathbf{p}_k^T \mathbf{H}_k \Delta\mathbf{p}_k \tag{32}$$

At the minimum of equation 32, the following system is satisfied:

$$\mathbf{H}_k \Delta\mathbf{p}_k = -\mathbf{g}_k \tag{33}$$

The gradient vector is

$$\mathbf{g}_k = -2\mathbf{J}_k^T \mathbf{C}_{zz}^{-1} \mathbf{r}_k \tag{34}$$

And where is the Hessian matrix, with size $n \times n$:

$$\mathbf{H}_k = 2\left(\mathbf{J}_k^T \mathbf{C}_{zz}^{-1} \mathbf{J}_k + \sum_{i=1}^{m} r_i \mathbf{G}_i \right) \tag{35}$$

$\mathbf{J}_k$ is the Jacobian matrix defined as:

$$\mathbf{J} = -\frac{\partial \mathbf{r}}{\partial \mathbf{p}} = \frac{\partial \mathbf{z}}{\partial \mathbf{p}} = \begin{bmatrix} \frac{\partial z_1}{\partial p_1} & \cdots & \frac{\partial z_1}{\partial p_n} \\ \vdots & \ddots & \vdots \\ \frac{\partial z_m}{\partial p_1} & \cdots & \frac{\partial z_m}{\partial p_n} \end{bmatrix} \tag{36}$$

And $G_i = \nabla^2 \, r_i / \sigma_{zi}$ is the Hessian of the weighted residuals.

Substituting equations 34 and 35 into 33, and calling **B** the sum in 33, we get the Newton's method parameter update:

$$\Delta\mathbf{p}_k = (\mathbf{J}_k^T \mathbf{C}_{zz}^{-1} \mathbf{J}_k + \mathbf{B})^{-1} \mathbf{J}_k^T \mathbf{C}_{zz}^{-1} \mathbf{r}_k \tag{37}$$

In the Levenberg-Marquardt method the Hessian is made positive definite by replacing **B** by an $n \times n$ diagonal matrix $\lambda_k D_k$, and the update to the parameter vector becomes

$$\Delta \mathbf{p}_k = (\mathbf{J}_k^T \mathbf{C}_{zz}^{-1} \mathbf{J}_k + \lambda_k D_k)^{-1} \mathbf{J}_k^T \mathbf{C}_{zz}^{-1} \mathbf{r}_k \tag{38}$$

where

$$D_{jj} = (\mathbf{J}_k^T \mathbf{C}_{zz}^{-1} \mathbf{J}_k)_{jj}; \quad j = 1,..., n \tag{39}$$

The updated parameter becomes:

$$\mathbf{p}_{k+1} = \mathbf{p}_k + \Delta \mathbf{p}_k \tag{40}$$

Far away from the solution, in the first steps, the algorithm starts with a relatively large value of λ , the Levenberg parameter, taking steps along the steepest-descent direction. Each time a successful step (i.e. a step leading to a reduction in the objective function) is taken, λ is reduced by a factor of $1/\nu$, where ν (> 1) is called the Marquardt parameter; however, if the step is unsuccessful, λ is increased by a factor of ν. As λ becomes small, the algorithm approaches the Gauss-Newton step with its quadratic convergence rate. The size of a scaled step, or parameter update, can be calculated as:

$$|\Delta p| = \left[\sum_{i=1}^{n} \left(\frac{\Delta p_i}{p_1} \right)^2 \right]^{1/2} \tag{41}$$

The minimization algorithm will continue taking new steps to minimize the value of the objective function until a stopping criterion is met. The stopping criteria can be any of the following (Finsterle, 2007):

- Number of iterations (steps), k, exceeding a specified number;
- Scaled step size smaller that a specified tolerance;
- Number of forward runs exceeding a specified number;
- Number of unsuccessful uphill steps exceeding a specified number;
- Norm of the gradient vector smaller that a specified tolerance;
- Objective function smaller than a specified tolerance.

3. CASE STUDY FOR NÁMAFJALL GEOTHERMAL FIELD

3.1 Review of available data

3.1.1 Geological data

The Námafjall geothermal field is located in the southern half of the Krafla fissure swarm, in the region where it intersects the boundary of the Krafla central volcano (Figure 2). The Krafla field, which lies inside the Krafla caldera, is thought to be related to a magma chamber located below 3-7 km under the caldera (Gudmundsson and Arnórsson, 2002). The fissure swarm that intersects the Krafla central volcano is part of the neovolcanic zone of axial rifting in N-Iceland. It is about 100 km long and 5-8 km wide. Námafjall is thought to be a parasitic field to the Krafla field (Arnórsson, 1995): magma from the Krafla caldera is likely to have travelled horizontally in the SSW direction along the fissures and fractures all the way down to Námafjall, serving as the heat source for the hydrothermal system. Supporting evidence for this is that during the Krafla eruption in 1977, well B4 in Námafjall discharged magma (Larsen 1978 cited in Isabirye, 1994). This magma, as suggested above, could have traveled along the fractures which had coincidentally been intersected by the well, leading to the magma discharge.

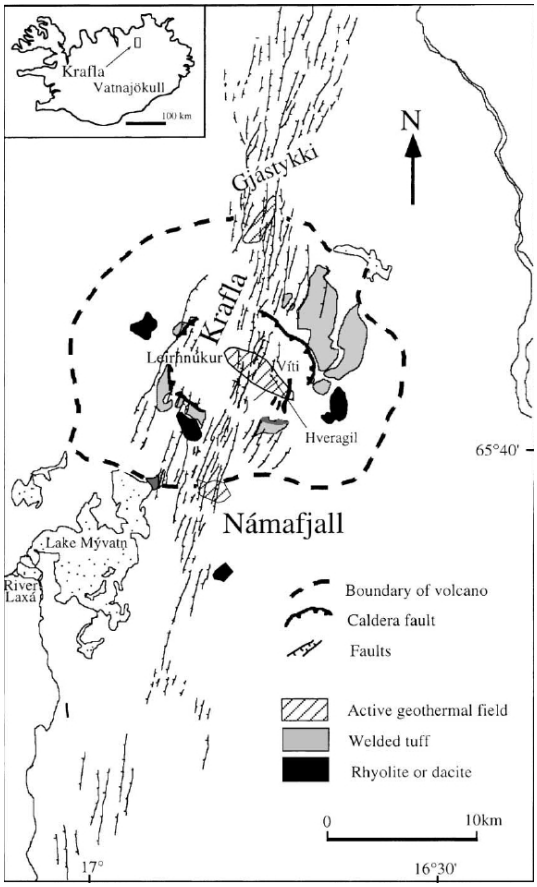

FIGURE 2: Location of the Námafjall field, N-Iceland (Gudmundsson and Arnórsson, 2002)

In the following paragraphs we will present a description of the geological characteristics of the Námafjall field, as presented by Gudmundsson and Arnórsson (2002) and other autors. The Námafjall ridge is part of the Námafjall-Dalfjall-Leirhnjúkur ridge, having an overall length of about 15 km and a width of about 1 km. The Námafjall ridge itself is about 2.5 km long and 0.5 km wide. This ridge is composed of hyaloclastites formed during the last glaciation period as a product of subglacial eruptions (Figure 3). The sides of the Námafjall ridge are covered with postglacial basaltic flows, coming from fissure volcanoes in the area.

Surface manifestations of geothermal activity in the Námafjall area are distributed over an area of 3-4 km. These manifestations include steaming grounds, mud pools, fumaroles and sulphur deposits. The hot springs are mostly located along the fractures and faults, while the altered grounds are located mainly on both sides of the Krummaskard fault.

The geological layers in the area can be divided in an upper and a lower succesion. The upper succession extends from the surface to about 1100 m depth, and is composed mainly of hyaloclastites (70%) and lava flow interlayers. The lower succession is composed mainly of lava from shield volcanoes intercalated with hyaloclastite layers. Below 1700 m, intrusives constitute about 50% of the formation. Some of the intrusives exhibit considerable degree of alteration, especially the hyaloclastites, but some of them are also fresh.

The area is marked by several fractures and faults, like Krummaskard and Grjótagja, and often the surface manifestations are clearly aligned with these fractures. Tectonic movements during the Krafla eruptions of 1977 were confined between the Krummaskard and Grjótagja faults, and in contrast to the rest of the wells, well B2 which is located outside these 2 faults, was not damaged by the movements (Isabirye 1994). Nevertheless, the system seems to be bounded by 2 main faults, namely the Krummaskard and Grjótagja faults, which are part of a graben (Mortensen et al., 2008).

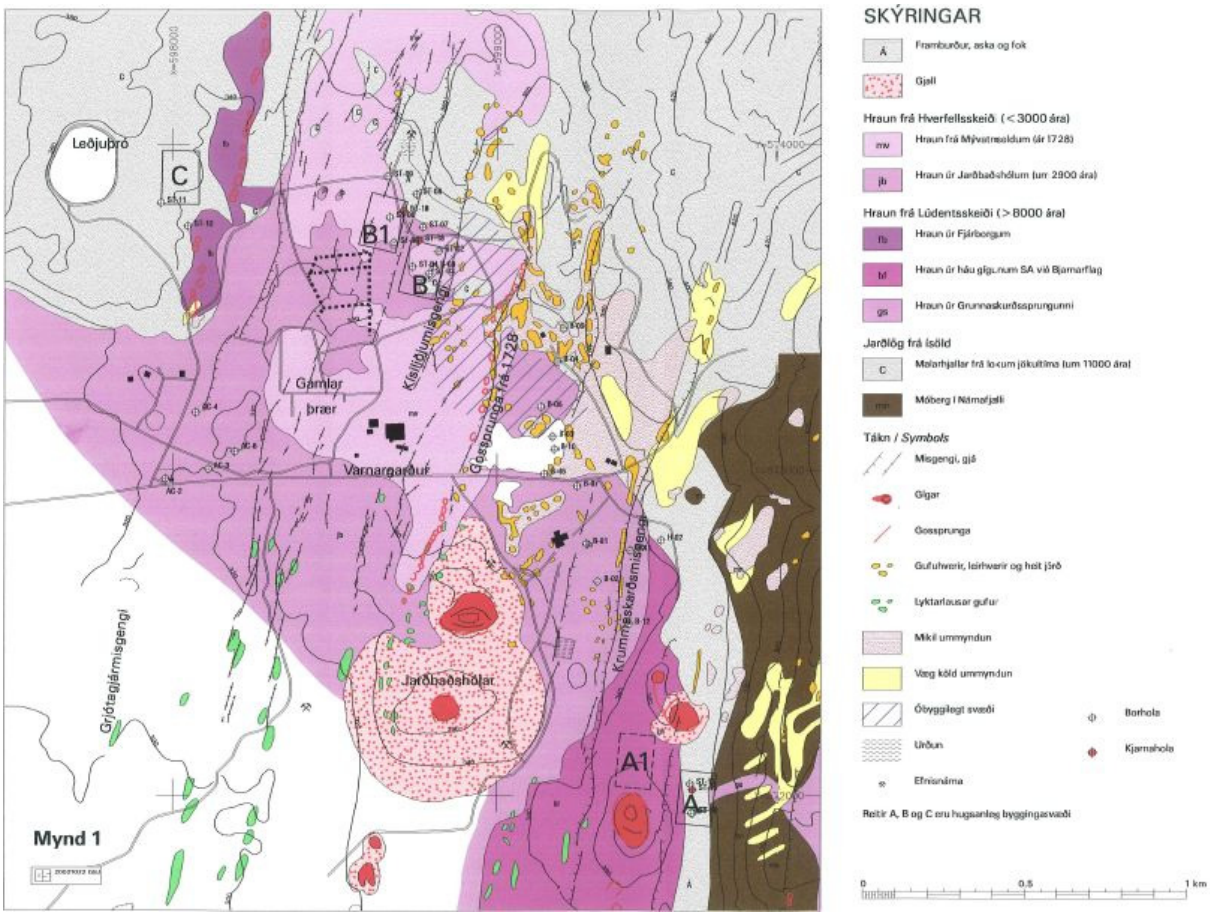

FIGURE 3: Geological map of Námafjall-Bjarnarflag (Hafstad and Saemundsson, 2002)

3.1.2 Geochemical data

The geochemistry of fluids in Námafjall has been studied by Ármannsson (1993) and later by Gudmundsson and Arnórsson (2002). The former author studied fluid samples taken from surface manisfestations such as fumaroles and mud pools in the period 1952-1993, and several geothermo-methers such as CO, HS, H and CO/H were used to estimate the temperatures of the fluids in the reservoir. The results for each geothermometer were averaged, and they are presented in Figure 4 . We can see that the highest reservoir

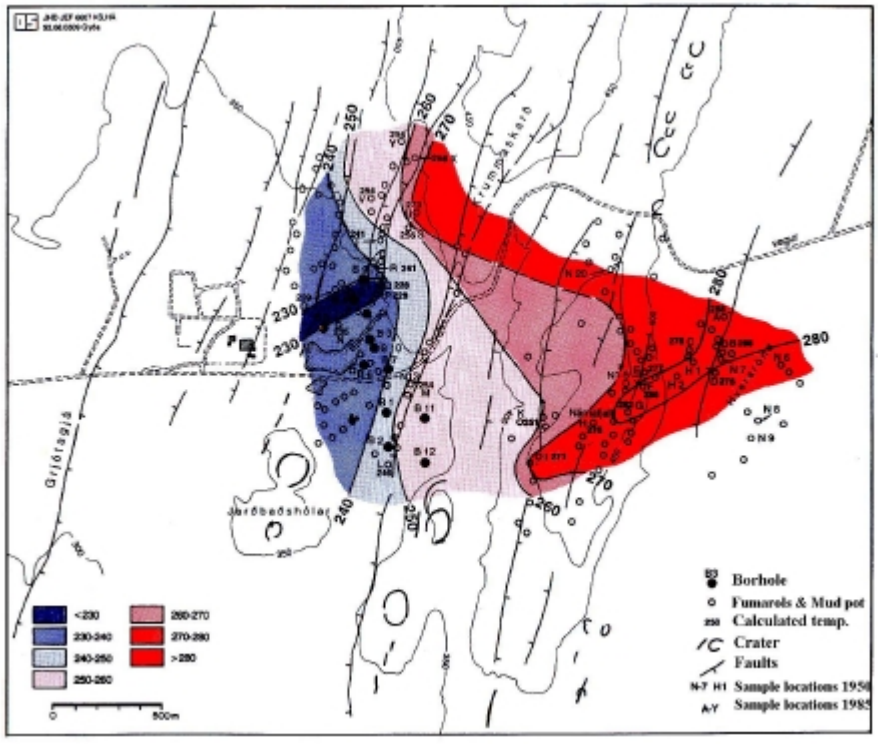

FIGURE 4: Reservoir temperature contours based on geothermometry (Ármannsson, 1993)

temperatures are expected to occur below the Námafjall ridge, east of the Krummaskard fault, with values close to 280 °C, gradually decreasing towards the west. In the area where most wells are drilled, the geothermometers predict temperatures of 240-260 °C.

Gudmundsson and Arnórsson (2002) did later geochemical studies in the Námafjall area, analyzing the fluids collected from wells B-4, B-11 and B-12. Based on the chloride, sulphate, silica concentrations, Na/K ratio and magmatic gas concentrations (HS, CO and H), they have concluded that the volcanic-rifting event occurring in 1977 was followed by an enhanced recharge of cold water into the reservoir, possibly because the tectonic movements caused an opening of fractures and fissures that allowed surface groundwater to enter the reservoir. After 1988, the groundwater incursion seems to have decreased.

Regarding the origin of the reservoir fluid, Arnórsson (1995) proposes that, since the Námafjall field is located in a low point in the fissure swarm, the recharge to the system could come from the local groundwater in the vicinity of the system seeping through the fissures and fractures into the reservoir.

3.1.3 Geophysical data

The currently accepted general resistivity structure of Icelandic geothermal systems has been presented by Árnason et al. (2000). By analyzing several geothermal fields in Iceland, they have found that all of them present the same basic structure consisting of a low resistivity cap wrapping a more resistive reservoir, with the surrounding rocks outside the cap also having high resistivity.

There appears to be no correlation of resistivity with lithology or porosity of the formation, but there is a clear correlation with the alteration mineralogy. The structure for a fresh water system like Námafjall is summarized in Table 1. For saline systems the structure is in general similar, but the temperature ranges for the cap region extends to around 300 °C.

TABLE 1: Resistivity structure and correlation to alteration mineralogy and temperature ranges in a fresh water system (Árnason et al., 2000)

Region	Resistivity	Alteration minerals	Temperature range
Surrounding rock	>10 ohm-m	No alteration	T <100 °C
Cap	<10 ohm-m	Smectite-zeolite	T <220 °C
Reservoir	<10 ohm-m, increasing	Chlorite-smectite	250 <T <260-270 °C
	>10 ohm-m	Chlorite-epidote	T >260-270 °C

A TEM resistivity survey was carried out in year 2001 described by Karlsdóttir (2002). The resistivity structure of the Námafjall field is shown in Figures 5-8.

In agreement with the model for the resistivity structure of the Icelandic geothermal fields presented above, we can first of all identify the outer 10 ohm-m contour in the pictures, which delineates the cap of the reservoir, and therefore we can use this contour to get an approximate idea of the size of the reservoir. Judging by the resistivity at 1000 m depth (600 m below sea level), we can say that the reservoir seems to have an area of some 20 to 25 km. Also we can note that the reservoir has a “bell” shape, being narrow in the upper parts and wider at the base.

Inside the reservoir, the location of the main upflow zone is indicated by the area of higher resistivity; this is a consequence of the high temperature fluids rising due to convection, and therefore, causing alteration in the formations at shallower depths. In our case, we can see that the upflow zone is located under Námafjall, and we could even speculate that it is being intersected by the Krummaskard fracture. Additionally there seems to be a smaller secondary upflow northwest of the main upflow zone. Furthermore, as the resistivity model suggests, the surroundings outside the cap of the reservoir, composed of unaltered rock, show high resistivity.

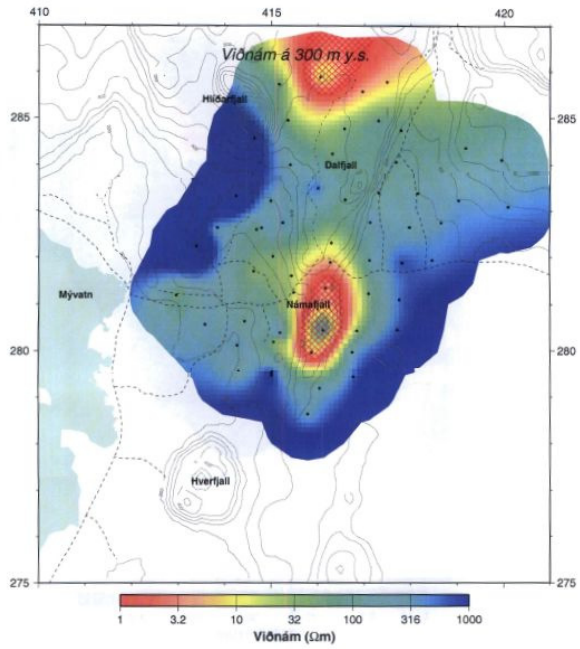

FIGURE 5: Resistivity 300 m above sea level (Karlsdóttir, 2002)

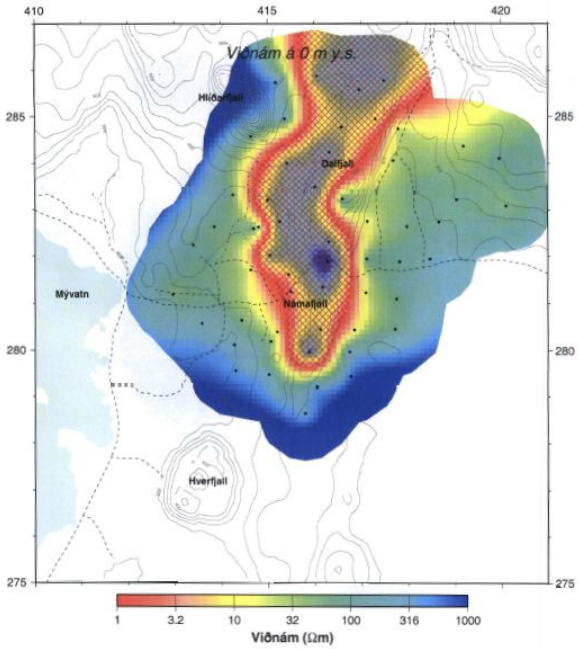

FIGURE 6: Resistivity 0 m above sea level (Karlsdóttir, 2002)

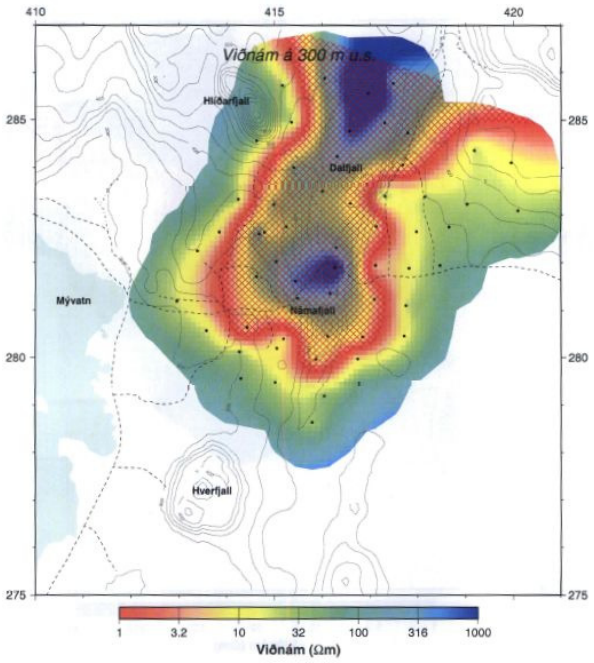

FIGURE 7: Resistivity 300 m below sea level (Karlsdóttir, 2002)

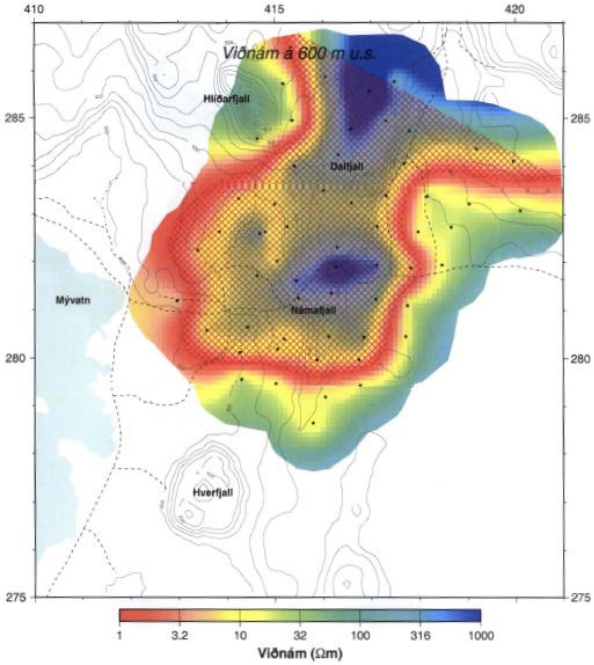

FIGURE 8: Resistivity 600 m below sea level (Karlsdóttir, 2002)

Inside the reservoir, the location of the main upflow zone is indicated by the area of higher resistivity; this is a consequence of the high temperature fluids rising due to convection, and therefore, causing alteration in the formations at shallower depths. In our case, we can see that the upflow zone is located under Námafjall, and we could even speculate that it is being intersected by the Krummaskard fracture. Additionally there seems to be a smaller secondary upflow northwest of the main upflow zone. Furthermore, as the resistivity model suggests, the surroundings outside the cap of the reservoir, composed of unaltered rock, show high resistivity.

Bearing in mind that the Krafla geothermal field is located about 10 km to the north of Námafjall, it would be interesting to draw some conclusions about the hydrological connection between the two

fields. By looking at the resistivity contours in the 600-1000 m depth range, we note that there is a region of lower resistivity, and therefore lower grade alteration, at the interface between Námafjall and Dalfjall. This has two possible interpretations: one would be that the hot upflow there is not as strong as under Námafjall, either because the permeability is lower or the temperature is lower. This might indicate some sort of flow barrier, and that the two fields are not hydrologically connected. The other interpretation would include some kind of cold water inflow cooling down the area.

3.1.4 Wells data

Drillings in the Námafjall field were initially done in the period 1947-1953, when exploratory wells were drilled mainly in the east part of the field. These wells were intended to produce steam, from which sulfur could be extracted. Later, in 1963, a diatomite processing plant was installed which used not only the steam directly in the process, but also included a 2.5 MW geothermal pilot power plant. Additionally, the fluids have been used for space heating. In 1975 10 wells had been drilled, all of them vertical, and the power plant operated successfully until 1977, when the 1974-1984 Krafla eruptions caused tectonic movements which damaged most of the wells. Wells B4 and B9 are the only original wells that have been able to produce afterwards. Two more wells were successfully drilled in 1978 and 1979, namely wells B11 and B12. Starting from 2006, 3 more wells have been drilled, all of them deviated: wells B13, B14 and B15.

Figure 9 (Gudmundsson and Arnórsson, 2002) shows the location of the producing aquifers and the permeable horizons encountered during the drilling of the wells and, in some of them, the corresponding temperatures as inferred from downhole measurements. The interpreted pivot point is shown with a circle, and the number enclosed in a box at the bottom of each well shows the average geothermometry temperature.

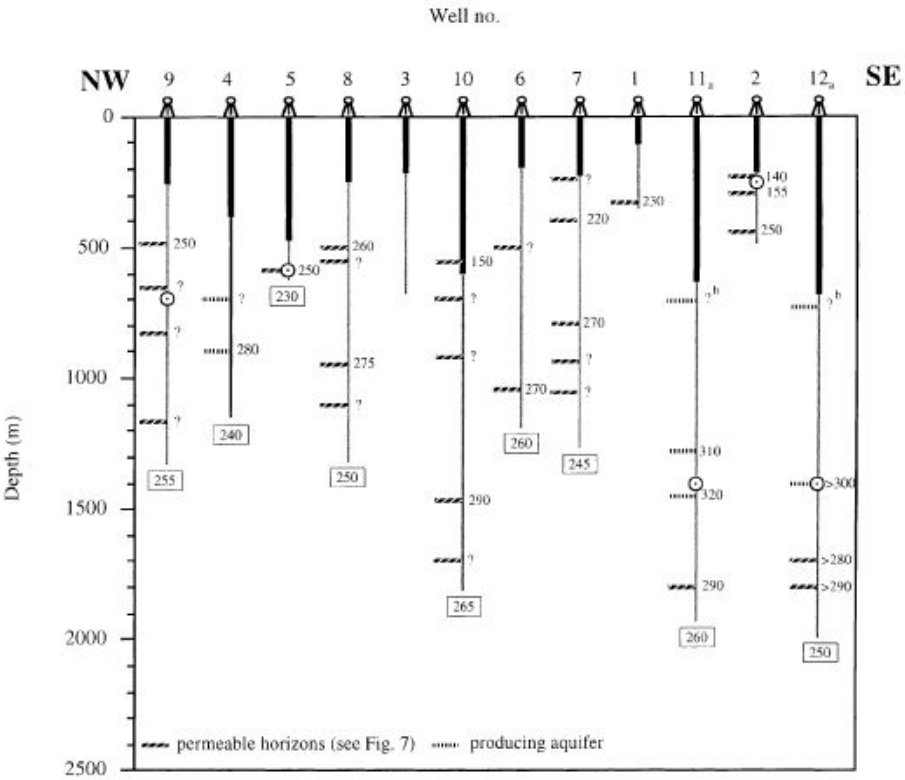

FIGURE 9: Aquifers and permeable horizons penetrated by wells in Námafjall. The circles indicate the position of the pivot point (Gudmundsson and Arnórsson, 2002)

Figure 10 shows a vertical cross-section of the estimated formation temperature contours in the field. In general, the conductive temperature gradient, indicating the thickness of the caprock, is observed down to depths 0-600 m in the region between wells B9 and B7, and 0-700 m close to wells B11 and B12. This observation is in agreement with the resistivity model discussed above, which predicts that the reservoir should start at temperatures close to 240-250 °C. Cold areas are observed in the shallower 500 m of wells B11 and B12, possibly caused by the downward seepage of colder surface groundwater.

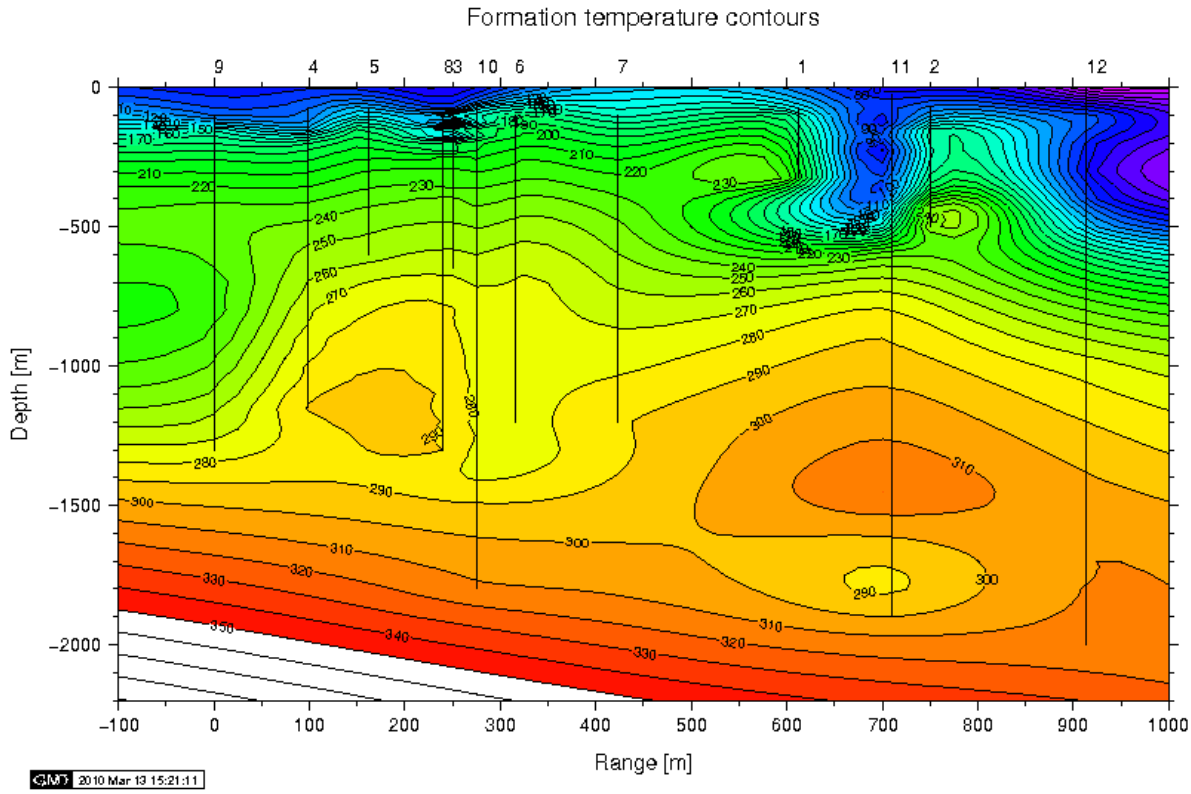

FIGURE 10: Reservoir formation temperatures estimated from temperature logs

3.2 Conceptual model

Synthesizing the above data, we can say that the geothermal system at Námafjall is centered under the Námafjall mountain, where the main upflow zone occurs. Temperatures up to 340 °C have been measured in the wellbores in that zone, and there is good agreement between resistivity data and geothermometry data for this. Secondary upflow zones may be present in the west part of the field. The heat source may be magma injections coming from the Krafla volcano in the north, nevertheless, the system will be treated as being hydrologically independent from the Krafla geothermal field. The permeability in the system in mainly due to the fractured formations found between the Krummaskard and Grjótagja fractures. The water recharge into the system is thought to come from the seepage of surface groundwater surrounding the field, sinking through the numerous fractures present. The movement of the fluids may have a preferential orientation NNE-SSW, corresponding to the orientation of the fissure swarm. The caprock of the system is located at variable depths, but in general extends down to 500 m depth.

3.3 Numerical model

A computer-based numerical model constitutes the main part of this work. It will ultimately be used to predict the reservoir response to different exploitation scenarios. The model is split into three stages:

1. The natural state of the field prior to any exploitation, corresponding to the reservoir conditions approximately in year 1963.
2. The second stage is the historical production data matching, where the available field data is to be matched by varying the reservoir forward model parameters; this will be done with the aid of automatic parameter matching capabilities of the iTOUGH2 code.
3. The last stage is the forecast, where different exploitation scenarios are simulated in order to get an estimation of the reservoir response. The general features of the model, as well as particularities of each of the three stages are presented in the following sections.

3.3.1 Generalities

3.3.1.1 Mesh design

One of the criteria used to size the computation domain of the numerical model is to set the boundaries as far as possible from the reservoir, so that the boundary elements do not sense the influence of the processes and changes taking place inside it. By taking this approach, the calculation results become less sensitive to the conditions specified at these "far" boundaries, and it is the physical laws as represented in the forward models what ultimately determine the thermodynamic conditions at the "immediate" reservoir boundaries, or reservoir envelope. An alternative approach is to model the exact volume of the reservoir, whatever that is thought to be based on the available geo-scientific data. This approach, of course, makes it necessary to specify much more precisely the boundary conditions, since the simulation results will highly depend on them. This latter approach has the advantage that a smaller domain is being modeled, therefore requiring less number of elements to achieve the same accuracy as the former approach. That is the reason why it has been commonly used in the past, when the computing power available was more limited.

Naturally, modeling a larger domain requires more elements and therefore is computationally more expensive. But with the increase of the computing power available in the standard PC's, more recent numerical models are using this method. In order to make the mesh more efficient, larger elements are used at the outer boundaries of the domain, where the thermodynamic variables gradients are expected to be smaller in space and time. In contrast, the elements inside the reservoir have to be smaller, since gradients there will be larger and we want to model in more detail the thermal conditions there. Consequently, an irregular Voronoi mesh was used, to have the flexibility of having the finer mesh concentrated only in the areas where it is required.

Figure 11 shows the overall mesh used, as well as the low resistivity contour which serves as basis for estimating the extent of the reservoir. The model area has an extension of 280 km, and the mesh has 314 elements per layer. It can be seen that the elements inside the reservoir (i.e. inside the resistivity anomaly) are, in general, smaller than those outside it. Particularly small elements were assigned close to the wells and the main faults and fissures, because the highest gradients are expected to occur there (Figure 12).

The vertical distribution of the mesh is shown in Figure 13. Layer A represents the groundwater system above the reservoir, while layer B representins the top part of the reservoir cap. Layers C to H constitute the high temperature reservoir. The deepest actual well (i.e. which has been already drilled) that will be producing in the model is well B14, which reaches a depth of about 2200 m, and the important aquifers (as seen in the circulation losses during drilling) for all wells are occurring above 1700 m. In our mesh the reservoir is assumed to reach a depth of 2200 m, and below that in layer I, we have placed a low permeability baserock, which has a thickness of 400 m. Note that this is just a general description of the vertical structure of the reservoir; a more detailed description will be made later, explaining the permeability distribution in the reservoir. It was decided to have the layers corresponding to the main part of the reservoir production zones (i.e. layers E to H) with a vertical dimension of no more than 300 m. The total number of elements in the mesh is 2829, with 10783 connections.

For the design of the mesh we used a series of Linux shell scripts developed by Andri Arnaldsson at Vatnaskil Consulting, Reykjavik. These scripts make use of the AMESH program, which generates an irregular mesh based on the Voronoi tessellation method (Haukwa, 1998).

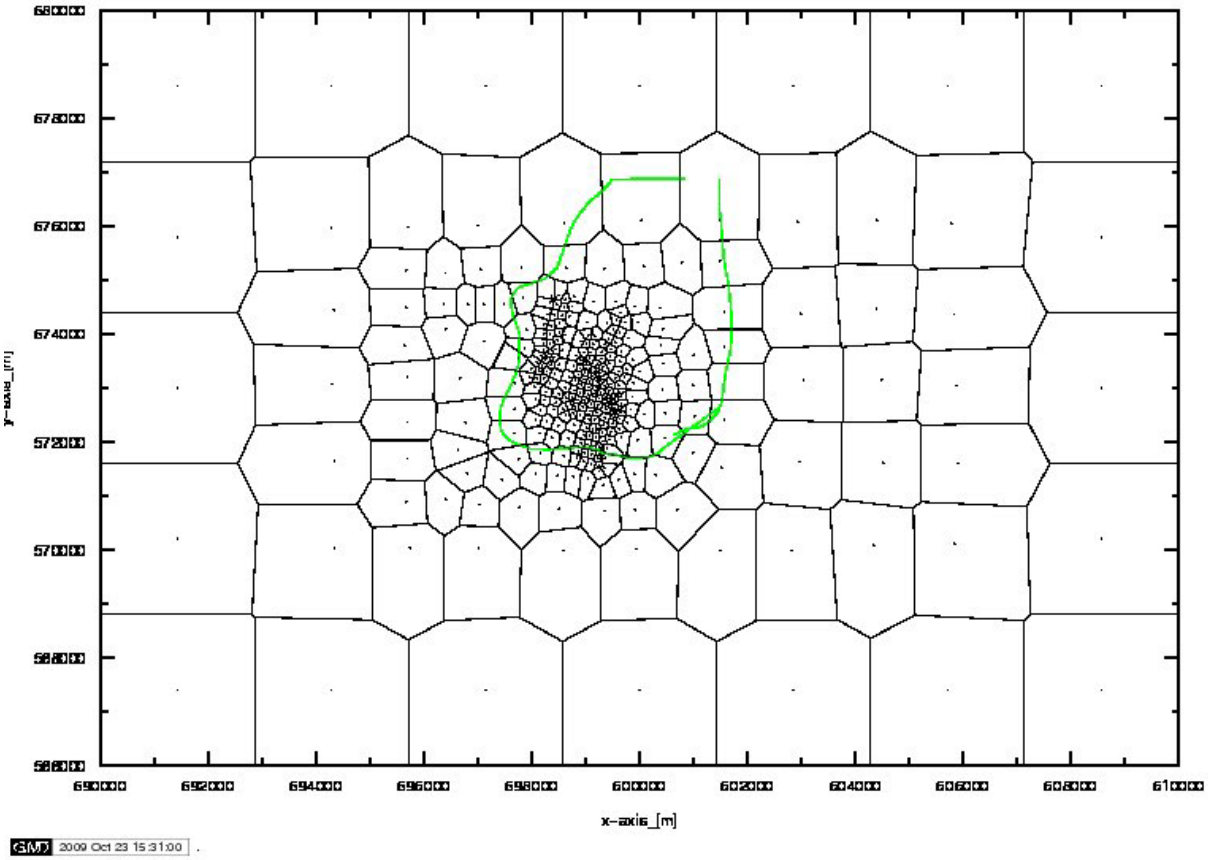

FIGURE 11: Aerial view of the mesh used. The green line indicates the high resistivity anomaly at 800 m depth

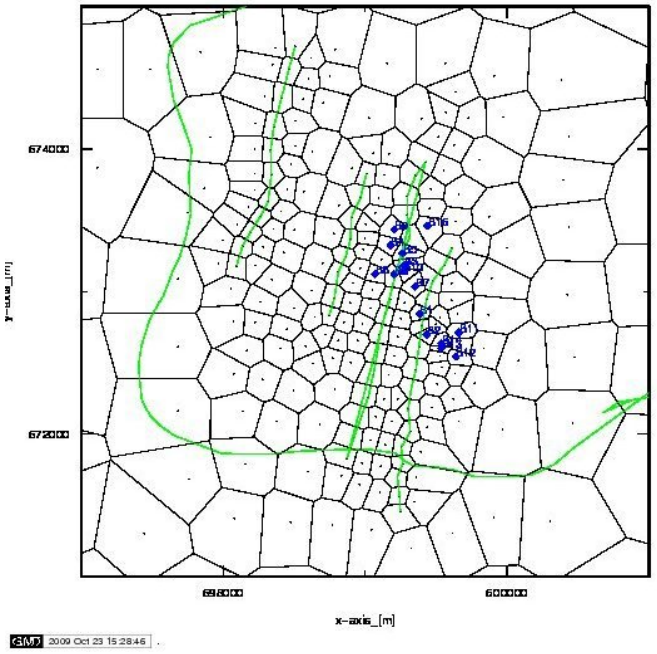

FIGURE 12: Detail of the mesh at the well field. The blue markers indicate the location of the existing wellheads and the NNE trending lines indicate the 4 main fractures modeled

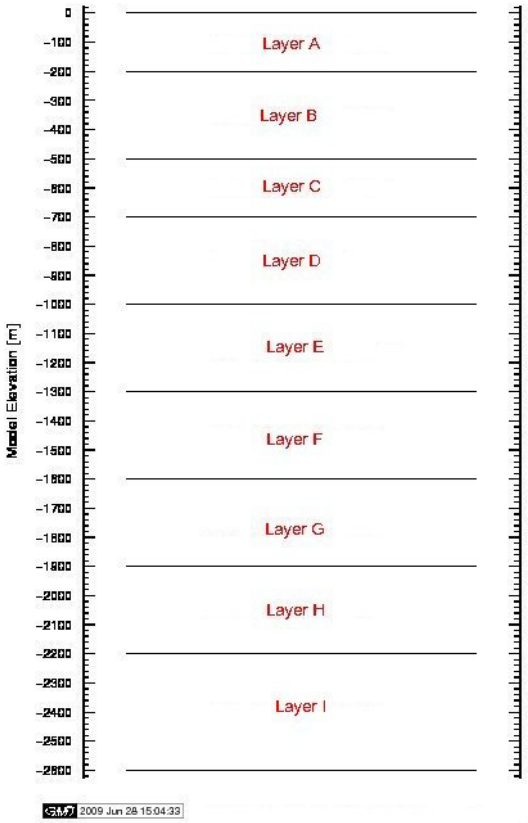

FIGURE 13: View of the layers used

3.3.1.2 Boundary conditions

The top, bottom and perimeter elements of the model have been given Dirichlet boundary conditions, that is, the values for the temperature and pressure have been specified and are assumed to be constant in time. At the top boundary this condition represents a constant yearly average ambient temperature of 5 °C. The conditions of the elements at the side boundaries of the model have been calculated by assuming a vertical temperature gradient of 100 °C/km and calculating the hydrostatic pressure at each depth based on the density variation of pure water with temperature. Pressure and temperature are constant at the side boundaries because they are assumed to be far enough from the reservoir, and therefore outside the influence of any changes happening within. The script *set_inactive* by Arnaldsson was used to set up the boundary conditions of the model.

As for the bottom boundary, it is more uncertain since we have no information about the thermodynamic conditions there. Therefore we took an approach taken by many modelers (O'Sullivan et al., 2001), which is assuming constant conditions corresponding to the values derived by using the method employed at the deepest side elements.

3.3.1.3 Rock types and permeability distribution

When developing a TOUGH2 model different rock types are specified, assigning properties like permeabilities in x, y and z direction, porosity, thermal conductivity and specific heat, and these rock types are assigned to different regions in the model domain. The approach taken was to start with as few rock types as possible and gradually create more rock types as required. In this study, 4 rock types were initially created to model the natural state of the reservoir, while the history match stage required the creation of most of the additional rock types.

During the initial approach, the rock types were not assigned based on the lithological units observed in the geological well logs, but based on the geophysical data, describing the shape of the reservoir, and also on the conceptualization of the reservoir. Afterwards, the permeability was adjusted to match the natural state and production history available, but keeping the parameters within what are perceived to be reasonable limits. One of the important pieces of data used to establish these limits is the injection test made on well B14 (Mortensen et al., 2008). Additionally, the permeabilities used in a numerical model of the Krafla geothermal field (Bödvarsson and Pruess, 1984) have been taken as reference point. A description of the physical properties of each material type and the assignment of each one to the simulation domain is presented in Appendix A. The script *set_rocks* by Arnaldsson was used.

The top layer of the domain was only assigned material type SURF1, and the layer immediately below it consists of material type CAPR1. The reservoir itself starts in layer C. As can be seen in the figures of Appendix A, we have tried to give the reservoir a bell shape, narrow at the top and wider at the bottom, following the shape observed in the TEM resistivity data. The reservoir itself is mainly composed of 2 material types, one is HIGK1, which has been assigned to the upper part of the reservoir, as well as for the lower part to the west of Krummaskard fault; the other type, RESV1, has been used for the region east of Krummaskard. The main reason for having 2 different material types in the reservoir was to be able to match the drawdown observed in wells B11 and B12.

A low permeability cap surrounds the reservoir. The permeability of this cap has an important role in controlling the recharge into the reservoir due to seepage of water from layer A, and will be one of the parameters included in the numerical optimization during the history match.

Four main fractures have been incorporated into the model, the Krummaskard and Grjótagja faults, which are thought to be the outer bounds of the reservoir, as well as 2 more major fractures in between them.

The bottom layer is composed of material BASE1, and its permeability is very low, therefore allowing very small, if any, water recharge into the system from below.

3.3.1.4 General computation parameters

The permeability interpolation at the interface between elements was done using an upstream weighted scheme, which, according to Pruess et al. (1999) is the best scheme suited for problems of multiphase flow in non-homogeneous media. For interface density, upstream weighting was used as well.

The relative permeability function was selected following Pruess et al. (1984). In their numerical experiments done in the model of the Krafla field, they suggest that linear relative permeability function gives better results in the Krafla system than the Corey curves. Hence we chose to use the same relative permeability function, which is shown in Figure 14.

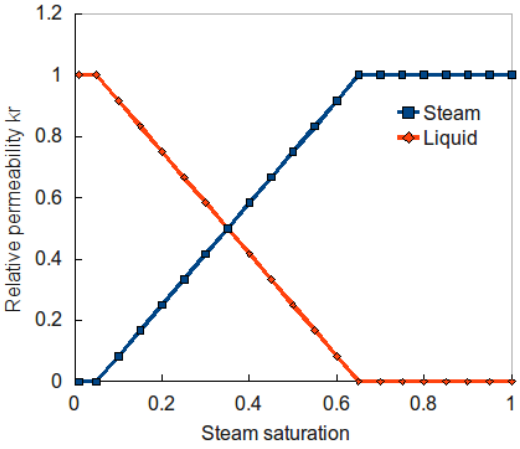

FIGURE 14: Relative permeability function used in the simulations

The irreducible vapor saturation Svr is 0.05, and the perfectly mobile vapor saturation Spv is 0.65, whereas for the liquid phase, the irreducible liquid saturation Slr is 0.35 and the perfectly mobile liquid saturation Spl is 0.95.

We also experimented with the relative permeability function used by Hjartarson et al. (2005), which uses Svp = 0.60 and Slr = 0.40, but found that for our model, a slightly better match was obtained with the first function.

For the calculation of the time step length, we used the automatic time step control feature in TOUGH2, which doubles the time step size if convergence occurs within a user-specified number of Newton-Rhapson iterations, which in our case was 4.

The linear equation solver used is the default iterative Lanczos-type bi-conjugate gradient solver, with incomplete LU-factorization as preconditioner.

The fluid of the Námafjall geothermal system is very dilute (Gudmundsson, 2002), therefore we decided to use the equation-of-state module EOS1 in the TOUGH2 simulator, which provides the thermo-physical properties for pure water in its liquid, vapor and two-phase states below the supercritical state.

3.3.2 Natural state model

The goal of developing natural state models is to verify the validity of conceptual models and to quantify the natural mass flow within the system (Bödvarsson and Witherspoon, 1989). It is done by matching observed formation temperatures and pressures from well logs, and if available, estimates of the natural mass fluxes observed at the surface. At this stage, an initial and rough estimate of the formation parameters distribution (permeability and porosity), and of the location and magnitude of heat and mass sources is obtained.

The result from the natural state simulations is not only used to compare the match with the measured formation temperature and pressure, but also serves as the initial conditions for the history match stage that follows in the modeling process.

3.3.2.1 Initial conditions

For the natural state simulation, we generated the initial conditions of the domain using the *set_incon* script by Andri Arnaldsson, in which we specified a temperature at the top of the domain of 5 °C, corresponding to the yearly average temperature in Iceland, as well as a constant vertical temperature

gradient of 100 °C/km, which has been commonly used as the average gradient within the active volcanic belt in Iceland. The temperature at the center of all layers is calculated by the script using these 2 values.

Additionally, we specified the pressure in the top layer of the domain. To estimate it, we used the groundwater-table maps of the area (Thórarinsson and Björgvinnsdóttir, 1980). The watertable in the Námafjall region is very shallow, and in many places it is a few meters below surface, therefore the pressure at the middle point of layer A, which has a thickness of 200 meters, was estimated by assuming that the water level goes all the way up to the top of the layer and calculating the hydrostatic pressure at 100 meters depth. Given this data, the *set_incon* script calculates the conditions for the rest of the elements in the mesh (Figure 15).

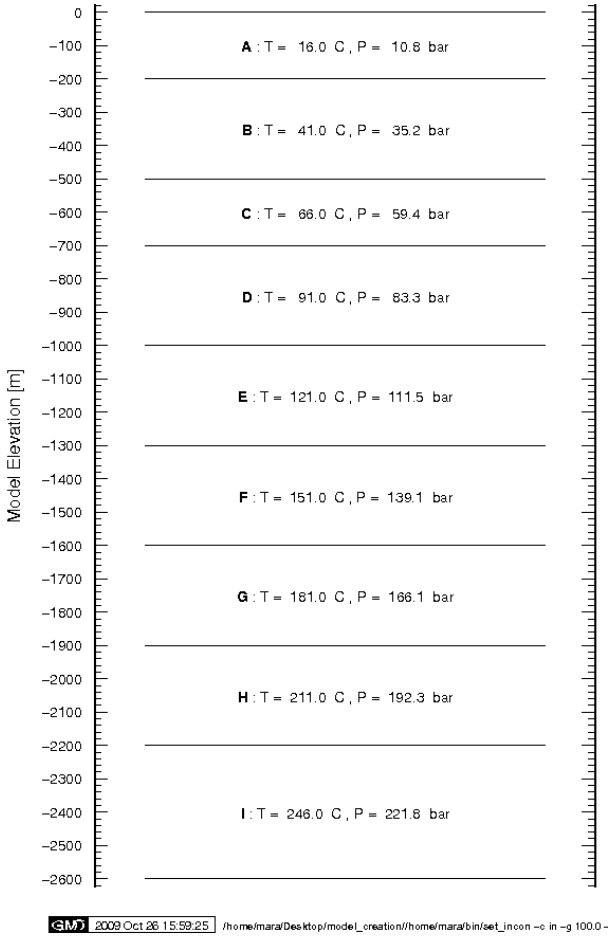

FIGURE 15: Initial conditions used for the natural state simulations

3.3.2.2 Sinks and sources

For the natural state simulation, we have included 3 types of sources: first, mass sources located at the bottom of the reservoir were positioned in the areas where the upflow is thought to be located, judging by the resistivity data. A total of 15 kg/s of fluid with an enthalpy of around 2000 kJ/kg are injected, giving a thermal energy input of about 30 MWt. Second, heat sources, located similarly around the upflow zones, but more spread out than the mass sources; these heat sources give an additional input of 18 MWt. These 2 deep types of source have been located in layer H. They were not located in layer I because it has been set as inactive and therefore no mass or energy balance equations are formulated for the elements there.

Finally, we have included several surface discharges of mass, represented as deliverability type sinks in TOUGH2, with productivity indexes ranging from to . These sinks have been located in areas of the field where high ground alteration is observed, as well as at the faults and fractures, where hot springs are found. See Figure 3. These sinks are located in layer B and not in layer A because the latter is inactive.

3.3.3 Model calibration with exploitation history

The goal of the exploitation history model is to refine the initial formation parameter distribution throughout the reservoir, as well as the distribution and magnitude of heat and mass sources. If the deliverability model is used to simulate the wells, the productivity index and the wellbottom pressure can be calibrated. It is done by matching the available production data, like mass flowrate, pressure drawdown and enthalpies observed at the wells. This stage of the modeling process is crucial, and it is likely that the amount of changes done to the model at this stage will be significantly larger compared to the natural state model in order to improve the match with observed data. When an acceptable match is obtained, the modeler has to assume that the parameters estimated are representative of the actual parameters present in the reservoir and therefore he can proceed to the forecast model. Moreover, the calculated reservoir conditions at the end of the history match are used as initial condition for the forecasting.

3.3.3.1 Data available for calibration

Pressure drawdown history is available for wells B5, B9, B11 and B12, and it was taken from Hjartarsson et al. (2005) with an addition of more recent data obtained from the Iceland Geosurvey (ISOR) database. Nevertheless, in many cases the data available consists of only about 2 to 3 measurements for each well, therefore interpolated points had to be added in between, trying to guess the possible trend of the series.

Enthalpy history for wells B1 to B12 was also taken mostly from Hjartarsson et al.(2005), complimented with additional recent data and with enthalpy for well B13. Similarly, the available data for most of the wells is sparse and interpolated data points had to be added in between.

Enthalpy data is far from being complete. Wells B3, B4 and B7 have only one measurement; wells B1, B2, B5, B6 and B8 have no measurements at all. Well B10 does not have measurements, but Gudmundsson et al. (1989) suggested that it is reasonable to assume that it was somewhere around 1200 kJ/kg. For well B9 the enthalpy history has been split in two: for the earlier stage of production (1963-1969) we have used an enthalpy value which was actually measured in 1984; for the second stage the measurements are more reliable. Finally, wells B11, B12 and B13 probably have the most reliable enthalpy data of all wells.

The mass extraction history of the field is shown in Figure 16. Production started in year 1963 with well B1 extracting around 23 kg/s. Gradually, more wells were drilled and put in production, and in 1976 the total production was about 200 kg/s. The sudden decline observed after 1977 is due to the tectonic movements during the Krafla eruptions, in which most of the wells were damaged. From the original wells, only B9 was used afterwards for production, and 2 new wells, B11 and B12 were later drilled. The production was kept to about 50 kg/s in the period 1980-2005. In year 2006 well B13 was drilled and included in the production.

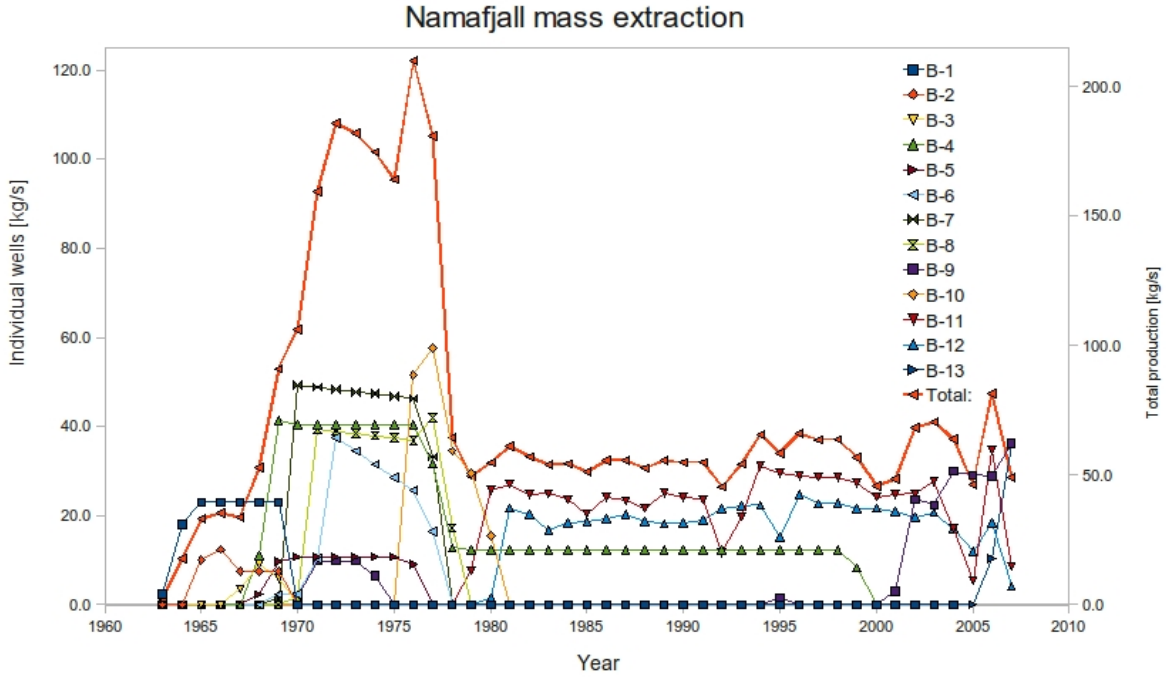

FIGURE 16: Production history of individual wells and total extracted mass

The individual well production can be used to calibrate the model if the wells are defined as deliverability type sinks (DELV-type). In that case, the well is assigned a productivity index and a bottomhole pressure, and TOUGH2 calculates the well production using the deliverability model presented in section 2.1.3. This calculated production is then compared to the measured data.

At the Námafjall field the wells came into and out of production stepwise. In this study, due to the

version of the iTOUGH2 code being used, we were not able to find a way to reproduce this stepwise behavior when the wells are declared in deliverability mode in TOUGH2; therefore, we decided to define the wells as mass sinks, specifying the mass extracted as a function of time. The disadvantage of this approach is that the well productivity index cannot be calibrated against observed flowrate data. To our knowledge, in order to make each well become "active" at a specific time in the simulation, modifications to the TOUGH2 source code would be required, which is beyond the scope of this study.

3.3.3.2 Initial conditions

The initial conditions used for the history match process are defined by the state obtained in the natural state model. A reasonably good natural state match can be obtained relatively early in the modeling process, but the history match is considerably more time consuming and requires making many changes to the model used for the natural state. As a consequence, the steps followed in the history match process are: first, run the history match simulation with an initial set of parameters obtained from the natural state model; most likely the match with the historical production data will not be satisfactory. Second, make changes to the parameters in order to improve the history match. Note that changing the parameters of the model means that the initial conditions used are no longer valid, since they were obtained with a different set of parameters; therefore we need to find the new initial condition by running the natural state simulation again and verify that the natural state match is satisfactory. Third, run the history match simulation again and check that the the improvements gained with the parameter changes still hold with the new initial conditions calculated, otherwise revert the changes and try a different parameter set. This is done iteratively until a satisfactory match is obtained in both the natural state and the history simulations.

3.3.3.3 Sinks and sources

For the history match simulations, in addition to the sinks and sources used to simulate the natural state, we need to add the wells, which were declared as MASS sources with time-dependent mass extraction.

3.3.3.4 Computation parameters

The history period simulations was run for 44 years, starting from 1963 (i.e. up to 2007), and the calculated system response was obtained every year and compared to the measured response. We used the default Levenberg-Marquardt optimization algorithm of iTOUGH2, with an initial Levenberg parameter of 0.001 and a Marquardt parameter of 10. The Jacobian matrix was calculated using forward differences, except for the last iterations, where we instructed iTOUGH2 to use central differences to increase accuracy.

3.3.4 Forecasting

From a practical perspective, the forecast constitutes the most important part of the modeling since it is supposed to provide aid in the management of the resource and the optimization of its long term productivity (Bödvarsson and Witherspoon, 1989). This model predicts the response of the thermodynamic conditions in the reservoir to different exploitation scenarios.

In the present work, 3 different exploitation scenarios were modeled:

Scenario 1. This model simulates 40 MWe electrical production:

- 50 kg/s extraction up to year 2015 with wells B9 and B13 (stage 1).
- Boost production to 40 MWe in 2015 with B9-B15 (stage 2).
- Add make-up wells as required. Simulation up to year 2045 (stages 3 and 4).

Scenario 2. Simulates 60 MWe production:

- 50 kg/s extraction up to 2015 with B9 and B13 (stage 1).
- Boost production to 40 MWe in 2015 with B9-B15 (stage 2).
- Boost production up to 60 MWe in 2020 with new hypothetical wells (stages 3 and onwards).
- Add make up wells as required. Simulate up to 2045.

Scenario 3. Simulates 90 MWe production:

- 50 kg/s extraction up to 2015 with B9 and B13 (stage 1).
- Boost production to 40 MWe in 2015 with B9-B15 (stage 2).
- Boost production up to 90 MWe in 2020 with new hypothetical wells (stages 3 and onwards).
- Simulate up to year 2045, adding make-up wells as required.

The estimation of the electrical power output will be made by using an overall thermal efficiency of 0.15%. In their numerical model for the Hengill volcano, SW-Iceland, Björnsson et al. (2003) have used an efficiency of 18%, but they are considering the use of the steam phase only. In Tester (2006), the suggested efficiencies for the energy conversion process with fluid temperature ranging from 200 to 250 °C are between 14 to 16%. Then, considering the use of both liquid and steam phases, we chose an efficiency of 15%.

The forecast simulation time starts in year 2008 and is run up to year 2045. Nevertheless, since new hypothetical wells are put into service in future years, and in our version of the iTOUGH2 code we do not have a feature to control the time when sinks in deliverability come into production, we have chosen to split the simulation and use different input files for each period simulated. Since at this stage we are not trying to match observed data anymore, for this part of the simulation we do not need to run the inversion algorithms of iTOUGH2, but instead we use only the forward simulator TOUGH2. Nevertheless, it was more convenient to use iTOUGH2 running in "forward mode only", since it provides useful additional features for data extraction from the output file for plotting.

Up to this point, we assume that we have adjusted the parameters of the model in a way that the observed data for the field and the output from the model match reasonably well (Appendix D). Therefore, the physical parameters of the reservoir like permeability, porosity, and boundary conditions are not changed any more. The same can be said about the heat and mass sources in the base of the reservoir, as well as for the surface mass sinks; the only exception are the wells. For the history match simulations, the wells have been declared as mass sinks with specified time dependent mass extraction rates. Consequently, if we were to use the same type of representation of the wells for the forecast simulations, we would only be able to assess the pressure response of the reservoir, but not the productivity of the wells since it would be fixed. Instead, from now on, we will use the deliverability model described in a previous section using 2 approaches: constant wellbottom pressure and variable wellbottom pressure, constant wellhead pressure to define the wells sinks. By doing so, we can additionally try to predict the production rates and trends for each well, as well as to assess if significant differences occur if the wellbottom pressure of the wells is allowed to change in time.

The location of the new hypothetical wells is determined based on the pressure distribution of the reservoir in layers E and F, where it has been determined during the history match that most of the wells are feeding from. Regions less affected by drawdown and cooling, but still within the high temperature reservoir are chosen to site the new wells.

Since for the reasons given above it is not possible to perform the simulation in one single continuous run, we have split the simulation time, inserting a new stage each time new wells come into production, either to increase the electrical power output or to maintain it. Each time the simulation is interrupted, a "save" file is created, which contains the state of each element at the time of interruption; this file is used as the initial conditions file when the simulation is continued in the next stage. For the first stage of the simulation, the *save* file created at the end of the history match period is used as initial condition.

3.3.4.1 Wells

The wells were simulated following two different approaches:

- As constant wellbottom pressure (DELV-type sink): The PI of each well was kept at the same value as the one used in the constant wellhead pressure model described below, and the bottomhole pressure was set such that the initial discharge rate of the well matched the initial discharge rate when defined as variable wellbottom, constant wellhead pressure sink.
- As variable wellbottom pressure, constant wellhead pressure sinks: For this simulation mode, a table was created for each of the existing wells using the HOLA wellbore simulator (Aunzo et al., 1991). The table contains the simulated wellbottom pressures for different combinations of flowrates and flowing enthalpies (Figure 17).

The actual geometry of the well was used in the simulation of the existing wells, with the exception that all the wells are assumed to be vertical. Recall that wells B13 to B15 are deviated. All the wells are assumed to have a single feedzone.

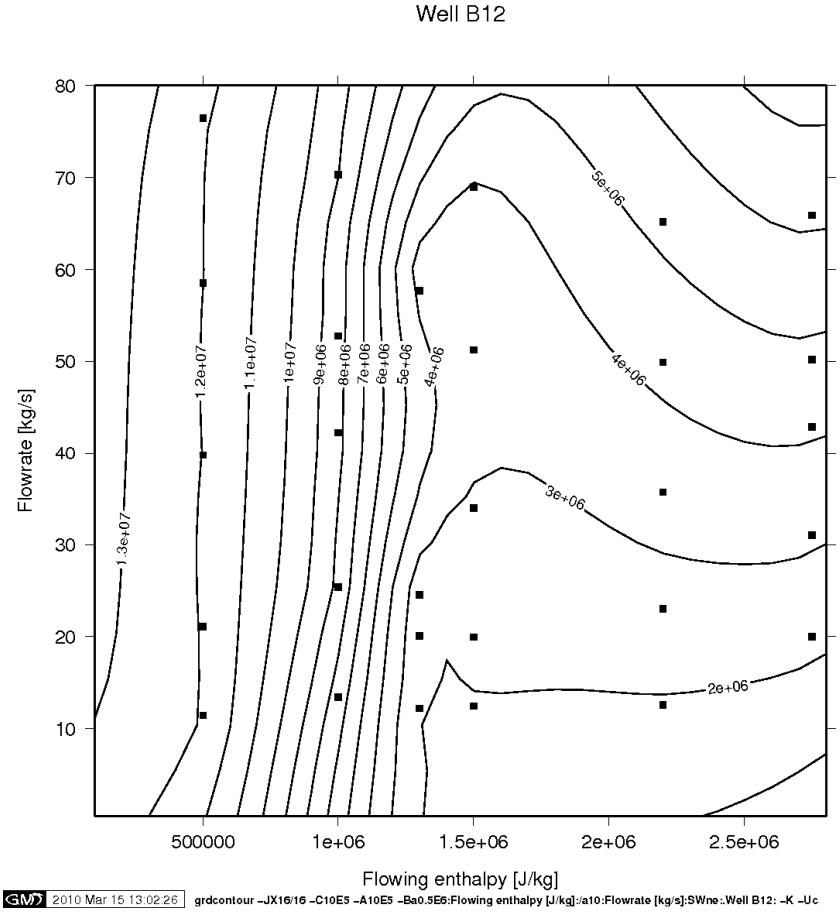

FIGURE 17: Contour plot showing the calculated wellbottom pressure [Pa] for different flowing enthalpies and flowrates for one of the wells in the model

An estimation of the productivity index of each well can be made using the permeability - thickness product obtained through injection tests, but with exception of well B14, no report of injection test data was found for the rest of wells. As a consequence, we only calculated the PI of well B14 and used this estimated value of m as a reference point for setting the PI of the rest of the wells, adjusting it to try to match the last observed values of production in each well, in the case of wells with production history, or to match an initial production in the range 20-40 kg/s for the new wells.

In the case of the new hypothetical wells, it is obvious that no well testing or geometrical data is available, and therefore we assume that their design will be similar to that of the more recent wells B13 to B15. The wellbottom pressure tables for them are therefore reused, choosing one that matches the intended feedzone depth in either layer E or layer F.

As explained in the mathematical modeling chapter in the beginning of the report, the flow of steam and liquid phases from the reservoir into the wellbore depends on the relative permeability function used. Therefore, in order to avoid the addition of inaccuracy and convergence problems in TOUGH2, we made sure that both HOLA and TOUGH2 were using the same relative permeability function. This required additionally that, as pointed out by Bhat et al. (2005), subroutine VINNA2 in the HOLA simulator was modified so that the calculation of the mass flowrate was done taking the reservoir fluid

parameters (density, saturation, viscosity) for production, i.e. flow entering the well, instead of taking the average between the fluid parameters and the wellbottom parameters.

3.4 Analysis of results

3.4.1 Natural state

The match between the measured formation temperature and pressure is presented in Appendix C. In this state, the thermal and mass balances in the reservoir are equal to zero, that is, the mass and heat entering the reservoir is equal to the amount being discharged, and the thermodynamic variables do not change anymore. The variation of the thermodynamic variables throughout the reservoir becomes negligible after some 60,000 years of total simulation time. A reasonable match was achieved for most of the wells; nevertheless, we can point out some discrepancies. We can see that for most of the wells the model underestimates the temperature in the upper layer; exceptions are wells B12 and B14, where the shallow temperatures are slightly overestimated. A more accurate match is achieved at reservoir depths. The slight temperature reversals observed in the shallow part of wells B4 and B12, as well as in the deep part of B11 and B15 are not adequately reproduced.

3.4.2 History match

The results for the historical data match is presented in Appendix D. The pressure drawdown data available for calibration is very limited. The first thing we noted is that the drawdown in wells B5 and B9 is considerably smaller than the drawdown observed in wells B11 and B12. To explain this, we can point out that the mass extraction from the former is smaller than that of the latter; we also see that B5 and B9 are located farther from the Krummaskard fault, as a matter of fact, they seem to be located in a more central position in the reservoir.

This different drawdown made us think from the beginning that this might be due to different permeabilities, and later it made us wonder about the permeability across the Krummaskard fault. We found that the best match was obtained by assigning a slightly higher permeability on the west side of Krummaskard, as well as giving a lower horizontal permeability value to the fault itself as compared to that of the surrounding rocks. Therefore, in a sense, this fault would be acting more as a sealing fault, somehow limiting, though not blocking completely the flow of water across it.

One interesting observation is the close match obtained for wells B11 and B12 when compared exactly to the observation values. See Appendix D.

In the history calibration process more weight was given to the enthalpy observations of wells B11 and B12 than to the enthalpy of the rest of the wells, since we know they are actual measurements and not guesses or estimations. It was therefore considered wise to put more effort in improving this match rather than for the other wells. We can see that both of these 2 wells have shown an overall decreasing trend in enthalpy, and the model is able to follow the trend to a reasonable degree.

For the rest of the wells, it is hard to say anything since most of the measured points are guessed or extrapolated, but in general we can note that the model estimates are almost in all cases higher than the corresponding measured (or guessed) values.

3.4.3 Forecast

In the following paragraphs we present the forecast results obtained for the 3 scenarios using coupled reservoir-wellbore simulation, as well as a comparison with the corresponding results defining wells as constant wellbottom pressure (DELV-type). It is worth mentioning that the creation of the wellbore tables proved to be a time consuming process due to the number of data points required to calculate in the table (around 40), and maybe even more due to the interactive user input required by the version of the HOLA wellbore simulator used. Significant time could be saved by using a simulator which does

not require interactive user input, and which could be repeatedly run for different conditions using a script or batch file. Excluding the user input, it was found that a typical wellbore run takes around one second to complete given that a good initial guess for the wellbottom pressure is provided. If a bad initial guess is provided the simulation will likely not converge and an new initual guess will have to be provided. Once the tables had been calculated, the additional computation time observed with the TOUGH2 simulator was insignificant.

3.4.3.1 40 MWe power production

The overall result for the simulated reservoir response is shown in Figure 18. A 40 MWe power output can be reached with 6 wells in 2015, and after this time, the production can be maintained by adding approximately 1 new well every 7.5 years, and by 2045 10 wells are required. The decline rate in electrical production is in the range 0.6 to 1.0 MWe/yr. The total mass extraction curve follows a trend which is quite similar to the total MWe, but we can note that the mass flowrate required to maintain the generation is decreasing in time. The reason for this is that the average enthalpy of the mass extracted has an increasing trend. A drawdown of 20 bars is observed at well B10 by year 2045 (Figure 19).

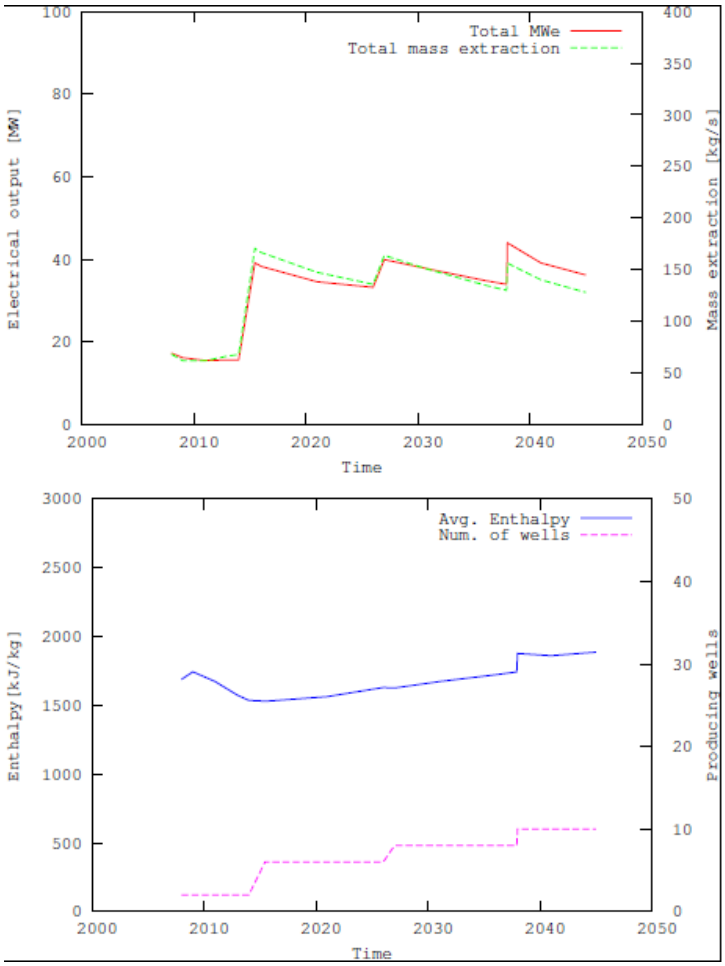

FIGURE 18: Reservoir response in the 40 MWe scenario. Picture shows estimated electrical output, total mass extraction, average enthalpy of the extracted fluids and number of producing wells

Most of the wells located to the east of the Krummaskard fracture (B11, B12, B13, B18 and B19) show either high enthalpies or a trend of increasing enthalpy (see Appendix E). Well B18, which was put in service in the latter part of the forecasting period, discharges dry steam from the beginning. The significant initial drawdown that these wells, particularly those closer to the Krummaskard fracture, show after they come into production can also be noted, which is not seen in the wells located to the west of Krummaskard. The reason for this difference is due to the fact that the permeability in the west side of the fracture is higher and also due to the proximity of these wells to the fracture, which has lower horizontal permeability and therefore restricts the flow across it. Drawdown values in the range of 10 to 20 bars are observed in the wells.

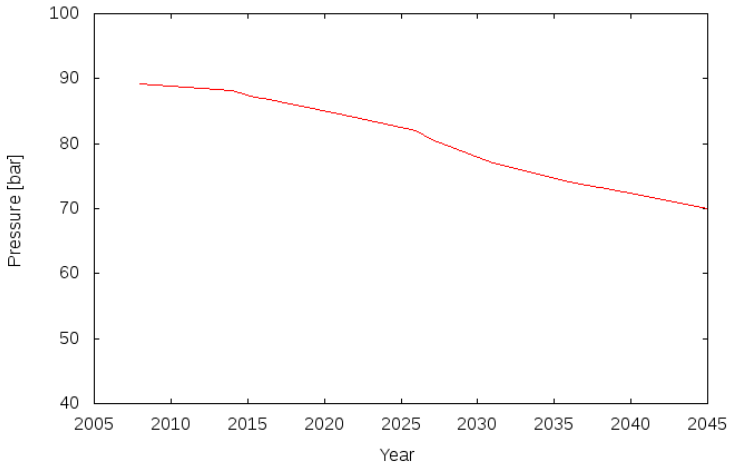

FIGURE 19: Pressure drawdown at well B10 in the 40 MWe scenario

On the other hand, the wells to the

west of this fracture (B9, B14, B15, B16, and B17) show a more steady enthalpy; the only exception is well B9, which seems to increase drastically in enthalpy after new wells are put in service in year 2015, reaching almost enthalpy of dry steam in year 2025. Most of the wells have an almost steady production by year 2045.

The figures showing the reservoir pressure, temperature and steam saturation distribution are presented in Appendix E. A steam cap has formed in most of the central part of the reservoir (layer D), except at the central and Gossprung from 1977 fractures, where some seepage of colder fluids from shallow layers may be causing a slight cooling. In layer E, the steam region forms towards the west of the reservoir, and in layer F the highest steam saturations are found close to the main upflow zone under Námafjall.

Pressure contours in Appendix E show that the most significant drawdown occurs, as expected, in the neighborhood of the wells. A 15-20 °C cooling is observed throughout the drilled area of the reservoir, and in layer E, it is evident that significant cooling occurs around the wells due to boiling.

3.4.3.2 Wells as DELV-type

In the case that the wells are modeled with constant wellbottom pressure, or DELV-type, we found the results to be as we expected. We found that the rate at which the well production declines is greater, and therefore the total mass extraction from the field is lower, which in turn causes a slightly lower increase of the average enthalpy of the fluids extracted. These combined effects cause the electrical output of the field at the end of year 2045 to be reduced by 14.9% (Figure 20). Then, in order to have the same output, it would require some additional 20 kg/s of fluid at 1808 kJ/kg enthalpy, which could mean one additional well in the simulation. In general, the shape of the pressure, mass production and enthalpy curves for each of the wells is quite similar.

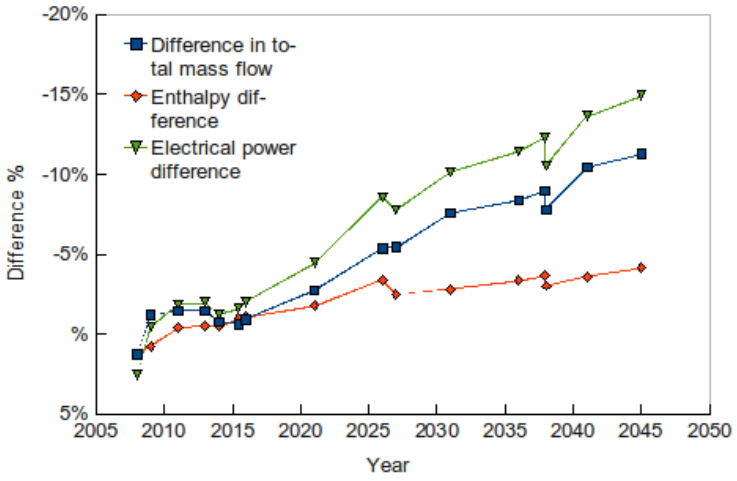

FIGURE 20: Comparison of production forecast between using F-type and DELV-type sinks for the wells for the 40 MWe scenario

3.4.3.3 60 MWe

In this scenario, it is required to add 6 more wells in year 2020 to increase the electrical output from 40 to 60 MWe, with the average enthalpy of the mass extracted at 1646 kJ/kg (Figure 21). After this time, it takes an average of 1 well every 5 years to maintain the electrical output. It can be noted how the total mass extraction declines at a steeper rate as compared with the 40 MWe scenario. The electrical production decline rate is 2.3 MWe/yr in close to year 2020 and falls down to 1.7 MWe/yr by 2045. The average enthalpy seems to be the same in year 2045 as in the 40 MWe scenario, with the only difference that in this scenario it increases earlier. By 2045 the model requires 17 wells to be in service. The mass extraction rate reaches 295 kg/s in 2020, and due to the increase in enthalpy maintaining it at some 225 kg/s some years later is sufficient. With this mass extraction regime, the model predicts that the drawdown at well B10, at the center of the reservoir, will be 30 bars (Figure 22).

In general, we can say that the wells with feedzones in layer E tend to increase in enthalpy more rapidly than those with feedzones in the deeper layer F. Actually, we can observe that in 2045, all the wells in layer E are discharging dry steam (see Appendix F). We also note that by this time, the flowrate for about 12 of the 17 wells has become quite steady. The drawdown at the wells is typically

in the range 20 to 30 bars, but some wells exhibit up to 40 and 50 bars drawdown, while well B9 has only 6 bars drawdown.

In comparison with year 2007, temperature does not seem to have changed significantly in the D layer, where most of the cooling has happened around well B9 (10 °C cooling). On the other hand, layers E and F show a more considerable cooling: 20 °C in layer E, with greatest cooling around wells and at the Gossprung and central fractures. Layer F shows even greater cooling of 25 °C in the center of the reservoir. In every case, the cooling is due to boiling (see Appendix F).

As for the pressure, in layer D we note that a considerable drawdown occurs around well B9, and that the HIGK1 domain shows a drawdown of about 6 bars, whereas RESV1 domain to the east of Krummaskard shows a higher drawdown of 10 bars. Layer E exhibits a drawdown between 22 to 25 bars, and layer F between 25 to 30 bars.

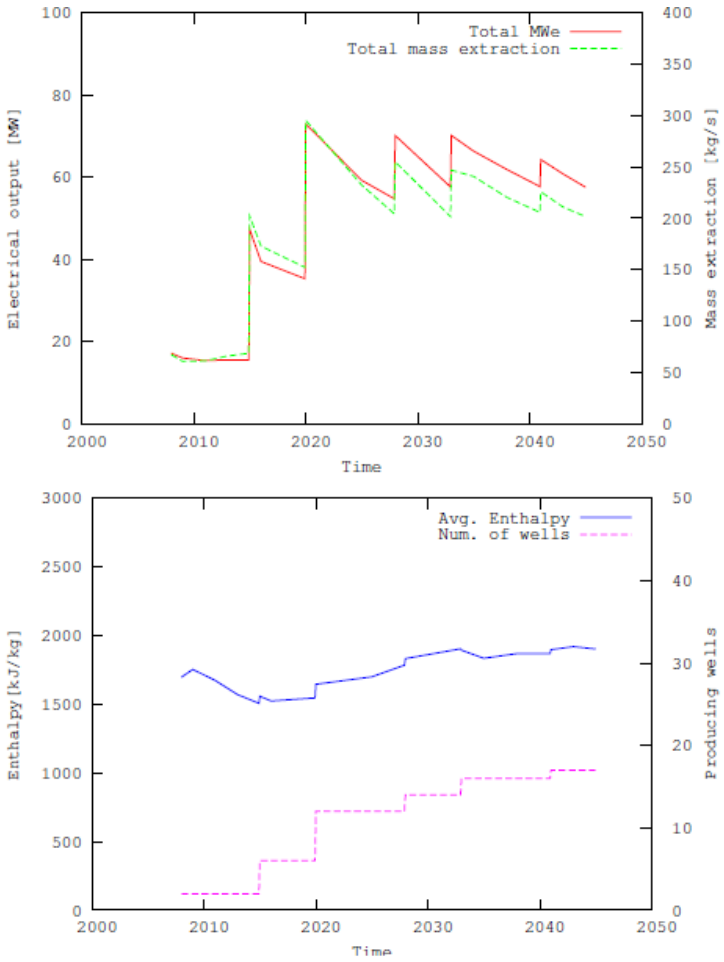

FIGURE 21: Reservoir response in the 60 MWe scenario

The steam zones developed are practically of the same size in the shallower layer D, but more significant in layers E and F as compared to the 40 MWe scenario.

In general, we can say that the wells with feedzones in layer E tend to increase in enthalpy more rapidly than those with feedzones in the deeper layer F. Actually, we can observe that in 2045, all the wells in layer E are discharging dry steam (see Appendix F). We also note that by this time, the flowrate for about 12 of the 17 wells has become quite steady. The drawdown at the wells is typically in the range 20 to 30 bars, but some wells exhibit up to 40 and 50 bars drawdown, while well B9 has only 6 bars drawdown.

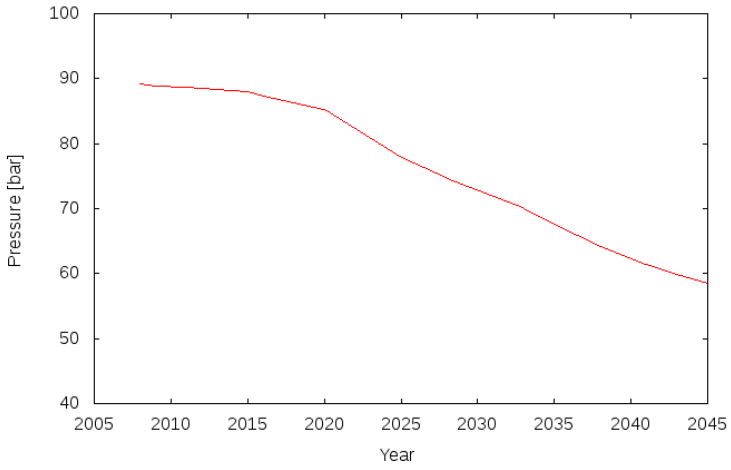

FIGURE 22: Pressure drawdown at well B10 in the 60 MWe scenario

In comparison with year 2007, temperature does not seem to have changed significantly in the D layer, where most of the cooling has happened around well B9 (10 °C cooling). On the other hand, layers E and F show a more considerable cooling: 20 °C in layer E, with greatest cooling around wells and at the Gossprung and central fractures. Layer F shows even greater cooling of 25 °C in the center of the reservoir. In every case, the cooling is due to boiling (see Appendix F).

As for the pressure, in layer D we note that a considerable drawdown occurs around well B9, and that the HIGK1 domain shows a drawdown of about 6 bars, whereas RESV1 domain to the east of Krummaskard shows a higher drawdown of 10 bars. Layer E exhibits a drawdown between 22 to 25 bars, and layer F between 25 to 30 bars.

The steam zones developed are practically of the same size in the shallower layer D, but more significant in layers E and F as compared to the 40 MWe scenario.

3.4.3.4 Wells as DELV-type

When defined as DELV-type sinks (i.e. constant wellbottom pressure), the wells show a more rapidly declining mass production as compared with the F-type sinks; It can be seen that the beginning of this divergence in the production coincides with the time when the enthalpies of the wells start diverging (Figure 23). This makes perfect sense, because this change in the enthalpy implies a change in the steam fraction of the extracted fluid, which is what effectively makes the bottomhole pressure change, and this in turn makes the mass production show the differences observed. Recall that in the F-type sinks the wellbottom pressure is allowed to decrease as the enthalpy increases, making the difference between the reservoir pressure and wellbottom pressure, the driving force for the flow into the wellbore, greater.

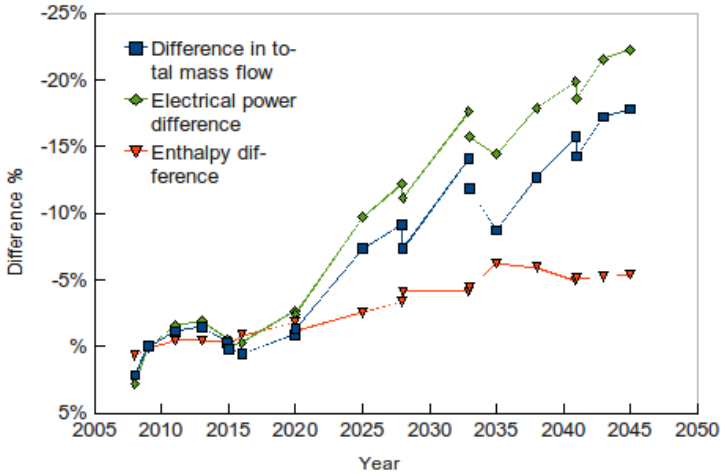

FIGURE 23: Comparison of production forecast between using F-type and DELV-type sinks for the wells for the 60 MWe scenario

It can be seen that the change in the production starts in year 2020, when the more intense exploitation regime starts, and in year 2045 the mass extraction is 15% less when DELV-type wells are used; moreover, the electrical output is 20% lower.

3.4.3.5 90 MWe

When the electrical production is increased to 90 MWe in year 2020, this requires about 350 kg/s of fluid, but with the gradual increase of enthalpy calculated, the required mass decreases to about 300 kg/s in year 2030 and seems to remain steady afterwards because the average enthalpy of the extracted fluid also seems to remain constant (Figure 24). Note how quickly the total flowrate decreases every time new wells come into service (the slope on the "teeth" of the total mass production curve), significantly more rapidly than in the 60 MWe scenario. The electrical production decline rate is 11.9 MWe/yr by 2020, and falls down to 3.9 MWe/yr by 2045.

In 2020 14 wells are required to reach the 90 MWe, and an average of 3.2 new wells are required every 5 years, reaching 30 wells in 2045. This is significantly higher than the 1 well every 5 years required in the 60 MWe scenario.

Drawdown in well B10 is predicted to be about 44 bars by year 2045, which is 14 bars more than in the 60 MWe scenario (Figure 25). Note that the curve does not show signs of approaching a steady state, and the drawdown will continue to be drastic in the following years.

Most of the wells used in this scenario which were also used in the 60 MWe (B9 to B26) show a similar trend in production, enthalpy and drawdown curves, with the only difference that in this

scenario, since a higher drawdown occurs earlier in time, some of them reach higher enthalpies earlier as well (see Appendix G).

Most of the wells that are put in service after 2028 are discharging dry steam; some exceptions occur for wells producing from the deeper layer F. Note also that, even though similar values of productivity index were used in most of the new hypothetical wells, the ones put in service in the latest part of the simulations have relatively lower yields, most of them in the range of 6 to 12 kg/s; this is a consequence of the great drawdown prevailing through the reservoir at this time.

Some wells like B27, B31 and B34 show a particular behavior in their enthalpy: they initially discharge fluid with very high enthalpy, but it drastically decreases shortly afterwards. The reason might be that at first the enthalpy of the fluid at the element from which it produces is close to that of dry steam, but the mass extraction causes inflow of colder, lower enthalpy fluids in the neighborhood.

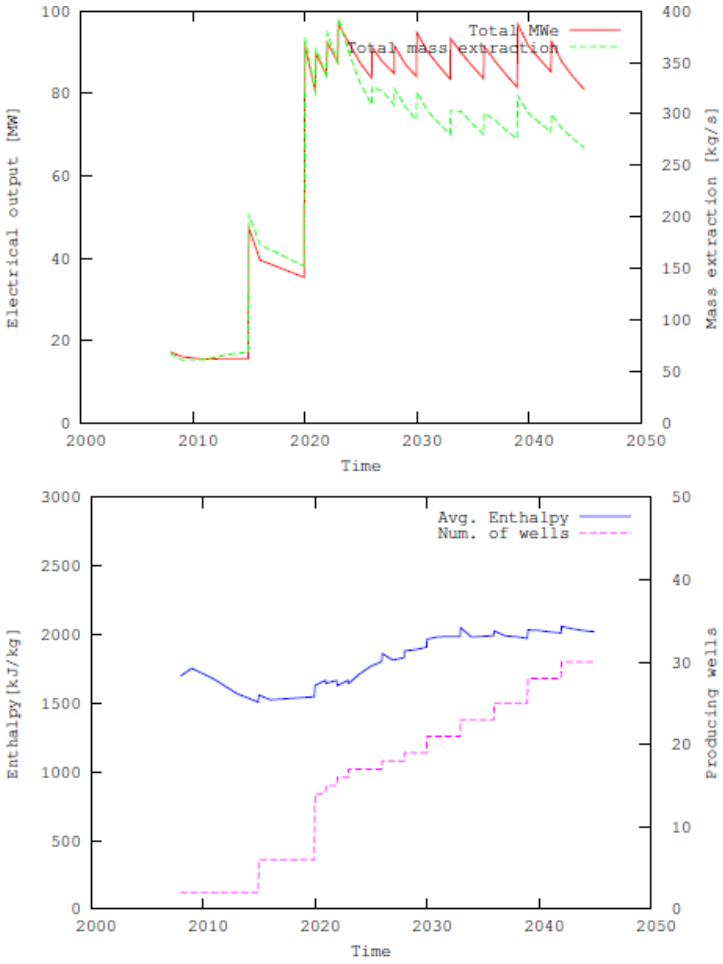

FIGURE 24: Reservoir response in the 90 MWe scenario

While the reservoir in layer D does not show significant differences in temperatures as compared with year 2007, layers E and F do show important changes: 25-30 °C cooling is observed in layer E, mainly around the wells and the Gossprung and central fractures. Furthermore, layer F seems to be most affected, with 30 to 40 °C cooling caused by boiling.

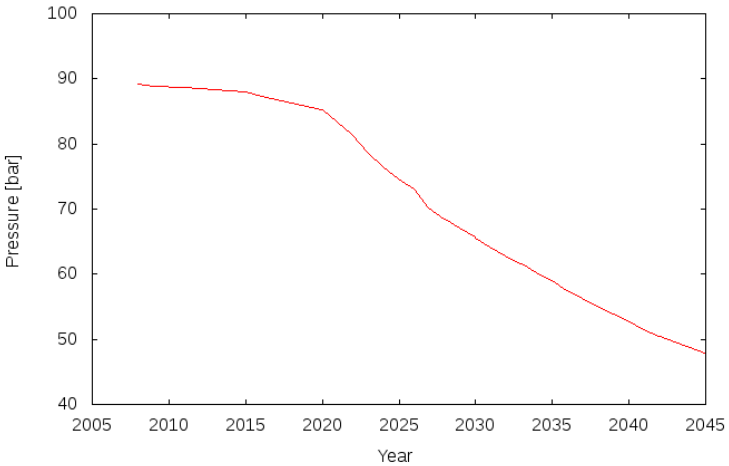

FIGURE 25: Pressure drawdown at well B10 in the 90 MWe scenario

Pressure drawdown is of the order of 10-12 bars in layer D, 26-28 bars in layer E and 30-40 bars in layer F. It may be noted that the drawdown is lower to the east of Krummaskard, in the RESV1 domain.

By year 2045 a dry steam region has developed in the whole of the central part of the wellfield in layer D, and in layer E the dry steam region reaches all the way to the Krummaskard fracture, where it seems to decrease further to the east. In layer F a smaller dry steam region develops in the center of the well field.

3.4.3.6 Wells as DELV-type

The difference in the model output for 90 MWe is similar to the one observed in the 60 MWe scenario: The divergence in output starts being significant in year 2020, when the mass extraction rate is significantly increased, and by year 2045, the average enthalpy of the extracted fluid using DELV-type wells is 3% lower, the total mass extraction rate is 15% lower and the estimated electrical output is 20% lower compared to the model with F-type wells (Figure 26). The significant contrast from the 60 MWe case is that the difference is reached earlier in the simulation, by year 2030 and stay close to that value afterwards.

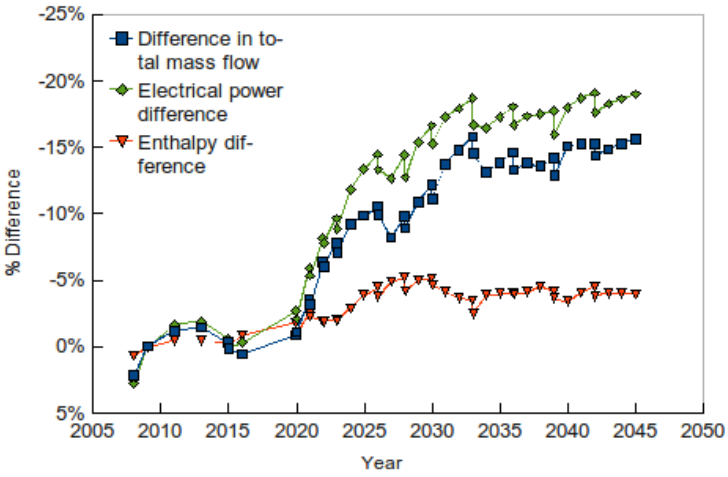

FIGURE 26: Comparison of production forecast between using F-type and DELV-type sinks for the wells for the 90 MWe scenario

3.4.4 Recharge to the system

Figure 27 shows an estimation of the total recharge into the reservoir, calculated by the recharge through the top, bottom and side boundaries (i.e. through the different caprock and baserock of the system) as well as from the mass sources located at the bottom for all the stages of the simulation: natural state in year 1963, history match up to year 2007 and the 3 forecast scenarios up to year 2045. We will refer to the term caprock as not only the low permeability layer B locate on top of the domain, but also the low permeability envelope surrounding the reservoir.

In the natural state the recharge into the system is close to 25 kg/s, most of which comes from the mass sources at the base; this recharge rate is equal to the discharge rate through the surface manifestations (e.g. hot springs, fumaroles); this is as expected, since it is the main reason why the simulator reaches steady state from the mass conservation perspective. The recharge going in through the low permeability caprock and baserock is only about 10 kg/s. Note that in all cases the recharge rate is negative in layer C, which is immediately below the top caprock; this indicates the ouflow of the reservoir occurring in that layer.

In year 2007, the amount of recharge through the caprock and baserock increases to 20 kg/s due to the pressure drawdown inside the reservoir caused by the mass extraction. The total recharge into the reservoir is 35 kg/s, which can be compared to the 50 kg/s being extracted at that time.

For the 3 forecast scenarios, it can be seen that the recharge does not increase significantly (Table 2), not even in the 90 MWe scenario, where the pressure inside the reservoir shows the greatest drop. The extraction rates for the 3 scenarios are 150, 250 and 300 kg/s. This suggests that the boundaries of the reservoir are very impermeable, and therefore the model can be regarded as a practically closed one. Additionally, this tells us that the model is pessimistic from a hydrological recharge perspective.

TABLE 2: Comparison between simulated mass extraction and recharge rate for each scenario

Scenario	Extraction rate (kg/s)	Recharge rate (kg/s)	Percent (%)
Natural state	25	25	100
2007	50	34	68
40 MWe	150	38	25
60 MWe	250	40	16
90 MWe	300	42	14

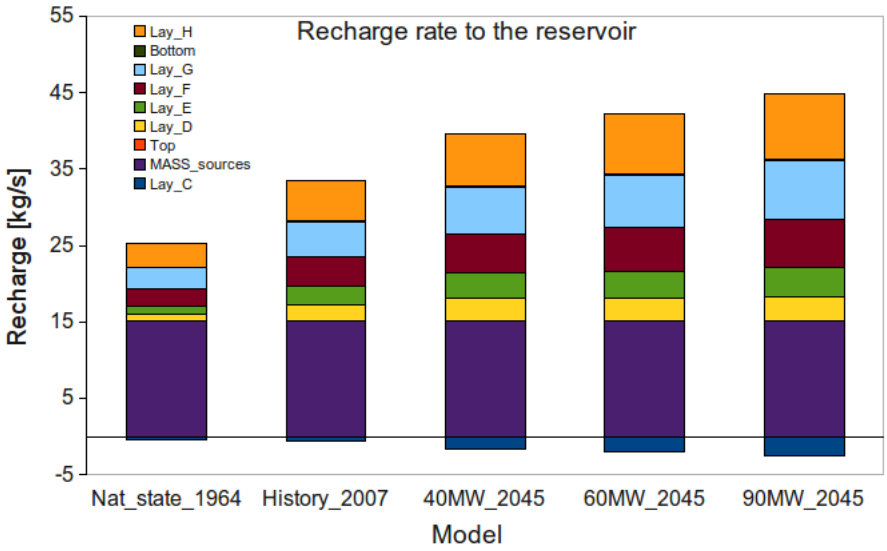

FIGURE 27: Mass recharge into the reservoir for the simulated natural state (year 1964), production history (year 2007) and the 3 forecast scenarios (year 2045)

4. CONCLUSIONS

A detailed numerical model of the Námafjall geothermal Field, N-Iceland, with coupled reservoir-wellbore simulation was developed in this work. The available natural state formation temperatures and pressures, as well as the exploitation history data served as a basis for creating a model which can be regarded from a hydrological perspective as pessimistic, since the water recharge into the system is limited due to the low permeability at the reservoir boundaries. A reasonable match was achieved with the natural state and historical data, but still, some datasets could not be matched. Some of the limitations found in the available data are that in some cases they were incomplete or based on estimates and not actual measurements. Additionally, since the wells have been drilled rather close to each other, the measured data, which is maybe the most valuable, is available for a fairly small and narrow region of the reservoir.

Three exploitation scenarios, namely 40 MWe, 60 MWe and 90 MWe were considered, and it was possible to maintain the 90 MWe case for 30 years in the simulations. Nevertheless, for this mass extraction regime the model predicts very large pressure drawdown in the reservoir, causing the development of an important steam pillow in the upper regions through boiling, which in turn produced significant cooling in and around the wells. The low pressure in the reservoir by year 2045 and consequent low yield from the wells suggest that 90 MWe electrical production will be difficult to maintain beyond that time according to this pessimistic model. More optimistic results might be obtained by including reinjection or by developing a model with more permeable caprock and more lateral inflow. In such cases, it can be expected that the simulation results will predict less pressure drawdown due to increased recharge, and therefore less boiling and cooling in the well field. Additionally, the production decline rates should be slower.

In the forecast model, the wells were treated in two different ways: as constant wellbottom pressure sinks and as constant wellhead pressure sinks by running coupled reservoir-wellbore simulation. This was done by using an indirect approach, which involved running the wellbore simulator in advance and generating wellbore tables given as input files for the reservoir simulator. It was found that the generation of these wellbore tables can be a time consuming process, particularly with the simulator used in this work, which required interactive user input. The use of a wellbore simulator which does not require interactive user input could be useful to reduce the time required. The additional computation power required was not significant for the coupled wellbore-reservoir simulation, and the results showed that, for the particular conditions of this model and the same number of wells, 15 to 20% more energy output was attained by modeling the wells as variable wellbottom pressure, constant wellhead pressure sinks. This output difference cannot be generalized for other models or reservoirs, since the magnitude of the variation will depend mainly on the variation in steam/liquid fraction experienced throughout the reservoir, as well as on the variation of the well flowrate. The main limitation of the indirect coupling approach used in this work is that wells have to be simplified as producing from a single feedzone, which causes difficulties in matching the enthalpy datasets during the model calibration and introduces inaccuracies in the forecasted enthalpy behavior of the wells.

The iTOUGH2 inversion algorithm proved to be very useful and effective in finding a set of parameters which yielded improved match with the available data sets. The process still requires the intervention of the human modeler, but the iTOUGH2 code includes very useful tools like parameter sensitivity analysis and estimates covariance, which provide valuable guidance in the history matching process. Like with any non-global optimization algorithm, it was found convenient and even necessary to test different starting sets of parameters in the matching process in order to escape sub-optimal local minima in the objective function topology. Also it was found that limiting the number of parameters included in the inversion process helped in understanding and visualizing the direction in which the optimization algorithm was moving the parameter set throughout the process. Additionally the computation time required is significantly lower.

Equally important as the simulation results is to have the means of visualizing the output data contained in the simulator's output files, which usually are quite large and somehow difficult to handle, as well as capabilities to compare the result of two or more different simulations. The

TOUGH2 simulator does not have plotting capabilities and external plotting packages are required. Since the simulations are run several times, it was found absolutely necessary to have scripts that automate the generation of visual output from the simulated data. Having these plotting scripts available before starting the numerical simulations is essential in order to keep the modeler's attention focused on the simulations.

REFERENCES

Ármannsson, 1993: *The geothermal system in Námafjall. Geochemical investigation.* Orkustofnun, Reykjavik, report 93053/JHD-29B, 30 pp.

Árnason, K., Karlsdóttir, R., Eysteinsson, H., Flóvenz, Ó., and Gudlaugsson, S., 2000: The resistivity structure of high-temperature geothermal systems in Iceland. Proceedings of the World Geothermal Congress 2000, Kyushu-Tohoku, Japan, 923-928.

Arnórsson, S., 1995: Geothermal systems in Iceland: Structure and conceptual models - I. High-temperature areas. *Geothermics, 24*, 561-602.

Aunzo, Z., Björnsson, G., and Bödvarsson, G., 1991: W*ellbore models GWELL, GWNACL, and HOLA user's guide*.

Bhat, A., Swenson, D., and Gosavi, S., 2005: Coupling the HOLA wellbore simulator with TOUGH2. Proceedings of the 20th Workshop on Geothermal Reservoir Engineering, Stanford University, Stanford, Ca, 6 pp.

Björnsson, G., 1987: *A multi-feedzone geothermal wellbore simulator.* Lawrence Berkeley Laboratory, University of California, MSc thesis, unpubl., 117 pp.

Björnsson, G., Hjartarson, A., Bödvarsson, G., and Steingrímsson, B., 2003: Development of a 3-D geothermal reservoir model for the greater Hengill volcano in SW-Iceland. *Proceedings of the TOUGH symposium, Lawrence Berkeley National Laboratory, Berkeley, California*, 11 pp.

Bödvarsson, G., Pruess, K., Stefánsson, V., and Elíason, E., 1984: The Krafla geothermal field, Iceland, 2. *Water Resources Research, 20, 11, 1531-1544.*

Bödvarsson, G., and Witherspoon, P., 1989: Geothermal reservoir engineering, part I. *Geothermal Science and Technology, 2, 1,* 1-68.

Finsterle, S., 2007: *iTOUGH2 user's guide.*

Gudmundsson, A., Steingrímsson, B., Jónsson, S., and Thórhallsson, S., 1989: *Boreholes at Bjarnarflag*. Orkustofnun, Reykjavik, report OS-89046/JHD-21 B (in Icelandic).

Gudmundsson, B., and Arnórsson, S., 2002: Geochemical monitoring of the Krafla and Námafjall geothermal areas, N-Iceland. *Geothermics, 31*, 195-243.

Hafstad, Th.H., and Saemundsson, K., 2002: *Bjarnarflag, investigation on construction sites.* Orkustofnun, Reykjavik, report OS-2002/042, 27 pp.

Haukwa, C., 1998: *AMESH: a mesh creating program for the integral finite difference method. User's manual*.

Hjartarson, A., Sigurdsson, Ó., Gudmundsson, Á., Ármansson, H., and Karlsdóttir, R., 2005: *Numerical model of the Námafjall geothermal system and forecast of it's response to 30-90 MW electrical generation at Bjarnarflag*. ISOR – Iceland GeoSurvey, Reykjavik, report ISOR-2004/009 (in Icelandic).

Isabyrie, E., 1994: Borehole geology and hydrothermal alteration in well B-9, Námafjall geothermal field, NE-Iceland. *Report 5 in: Geothermal Training in Iceland 1994*. UNU-GTP, Iceland, 89-121.

Karlsdóttir, R., 2002: *Námafjall TEM resistivity measurements 2001*. Orkustofnun, Reykjavik, report OS-2002/057 (in Icelandic).

Mortensen, A., Egilson, T., Gautason, B., Gunnarsson, H., and Ingólfsson, T., 2008*: Bjarnarflag - well BJ-14. 3rd stage: Drilling of production section from 847 m to 2506 m depth*. ISOR – Iceland GeoSurvey, Reykjavik, report ISOR-2008/039 (in Icelandic).

O'Sullivan, M., Pruess, K., and Lippmann, M., 2001: State of the art of geothermal reservoir simulation. *Geothermics, 30, 4,* 395-429.

Pruess, K., 2002: *Mathematical modeling of fluid flow and heat transfer in geothermal systems - An introduction in five lectures.* UNU-GTP, Iceland, report 3, 92 pp.

Pruess, K., Bödvarsson, G., Stefánsson, V., and Elíason, E., 1984: The Krafla geothermal field, Iceland 4. History match and prediction of individual well performance. *Water Resources Research, 20, 11*, 1561-1584.

Pruess, K., Oldenburg, C., and Moridis, G., 1999: *TOUGH2 user's guide, version 2.0*.

Tester, J., et al., 2006: *The future of geothermal energy: Impact of enhanced geothermal systems (EGS) on the United States in the 21st century*. MIT, Cambridge, MA, 372 pp.

Thórarinsson, F., and Björgvinsdóttir, B., 1980: *Krafla-Námafjall: Groundwater level*. Orkustofnun, Reykjavik, report FTh-BB-80/01 (in Icelandic).

Tokita, H., Lima, E., and Hashimoto, K., 2005: A middle-term power output prediction at the Hatchobaru field by coupling multifeed wellbore simulator and fluid-gathering pipeline simulator to reservoir simulator. *Proceedings of the World Geothermal Congress 2005, Antalya, Turkey,* 8 pp.

APPENDIX A: Rock type distribution in the simulation domain

Colour maps of the rock types used, and some physical properties of each rock type. φ is porosity, k_x, k_y, k_z are permeabilities in the three directions (mD), k is the thermal conductivity (W/m C) and C is the specific heat (J/kg C)

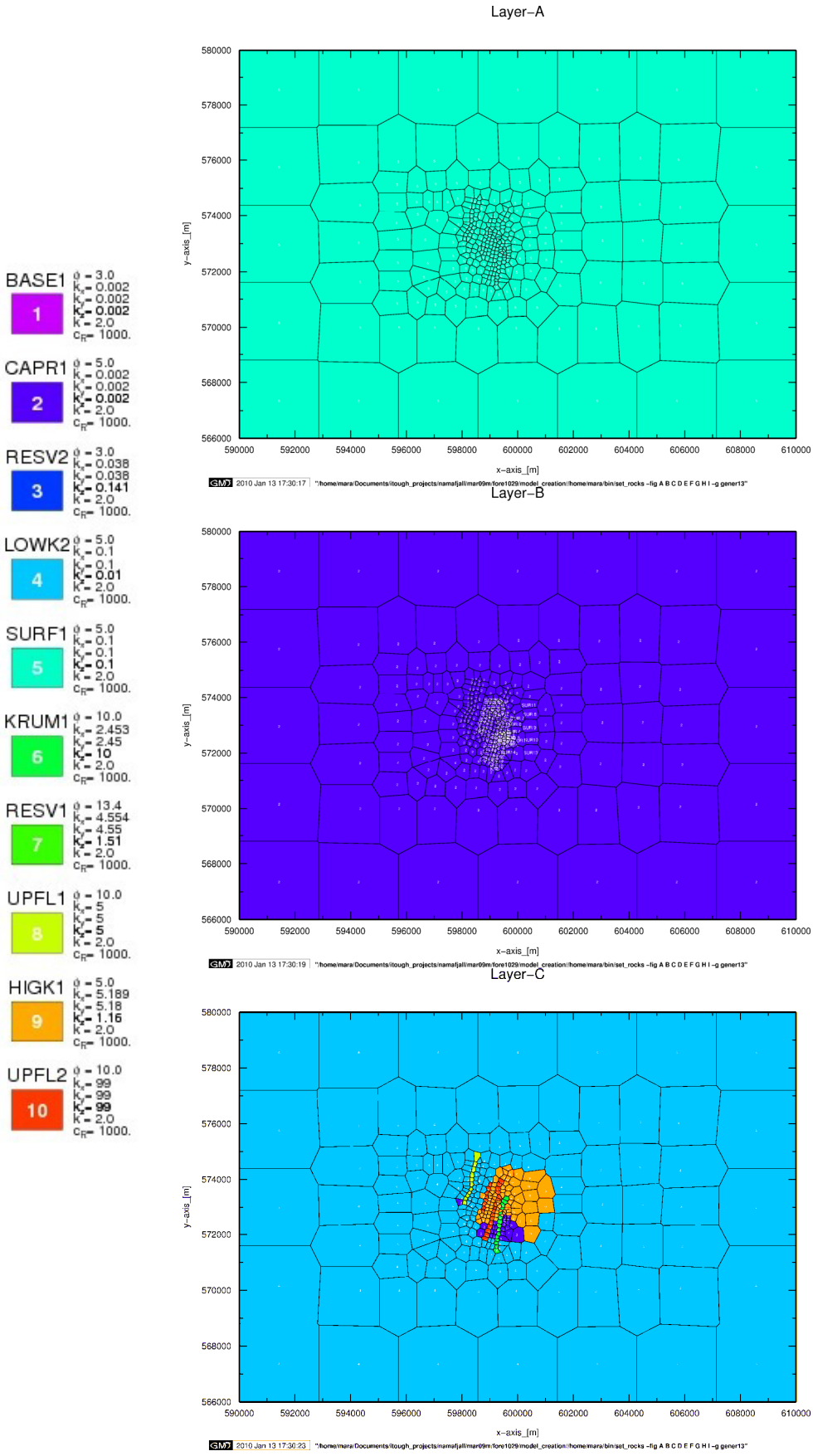

Layer−D

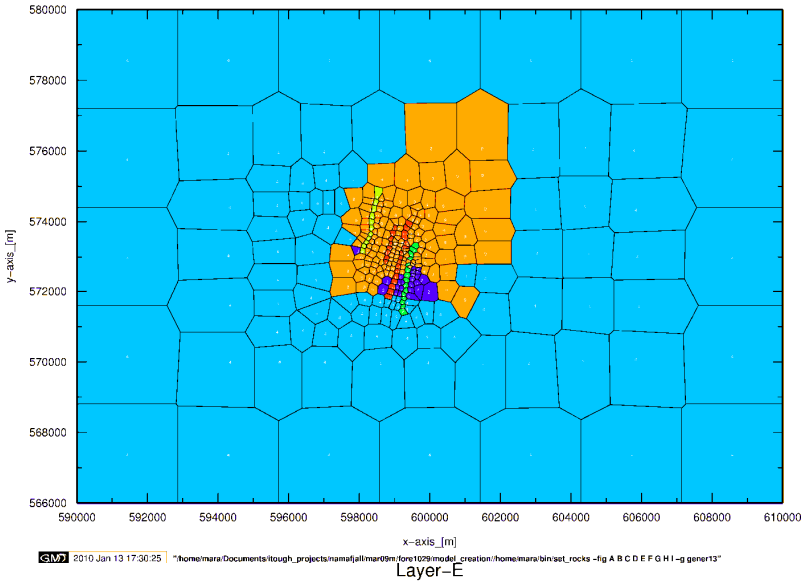

Layer−E

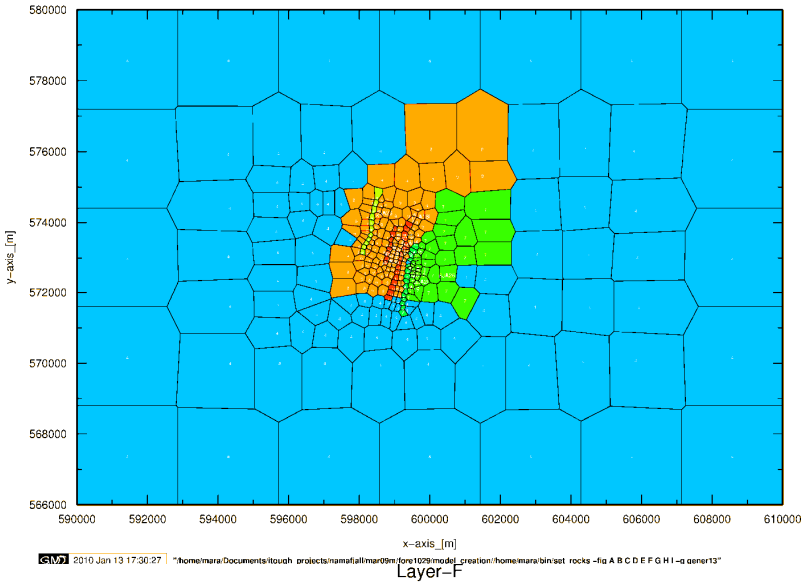

Layer−F

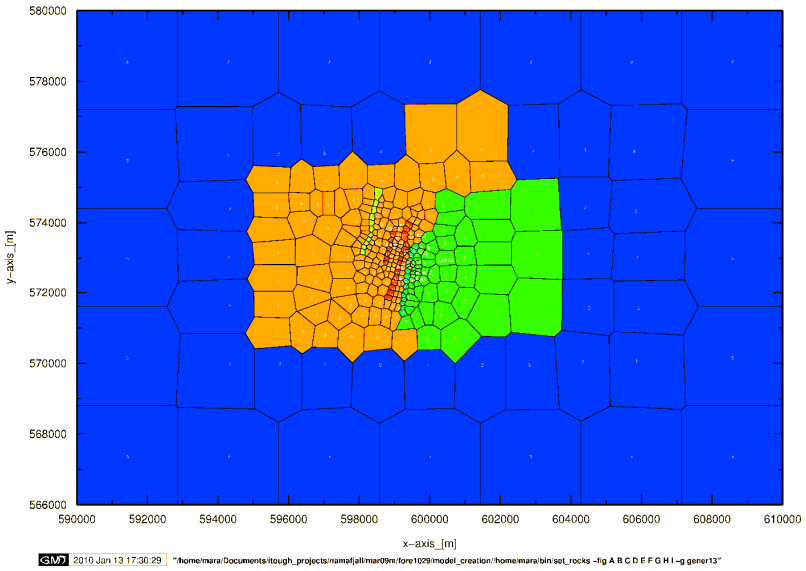

Layer–G

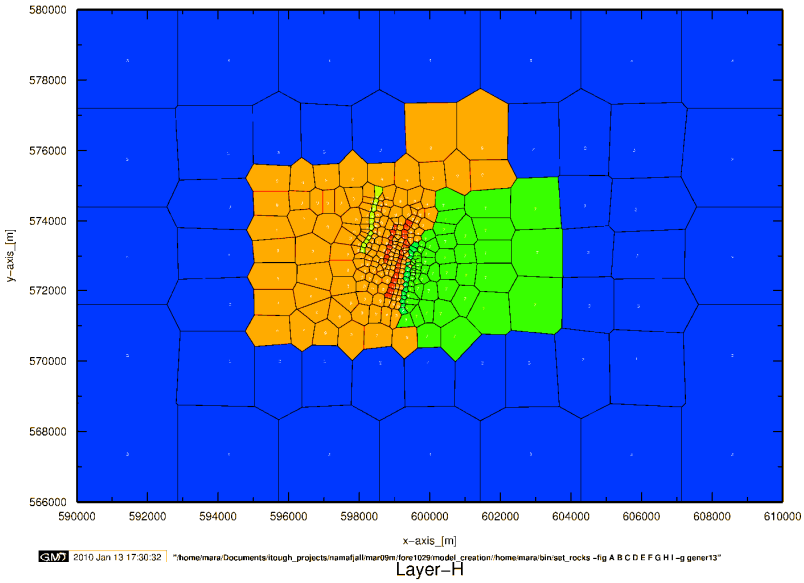

Layer–H

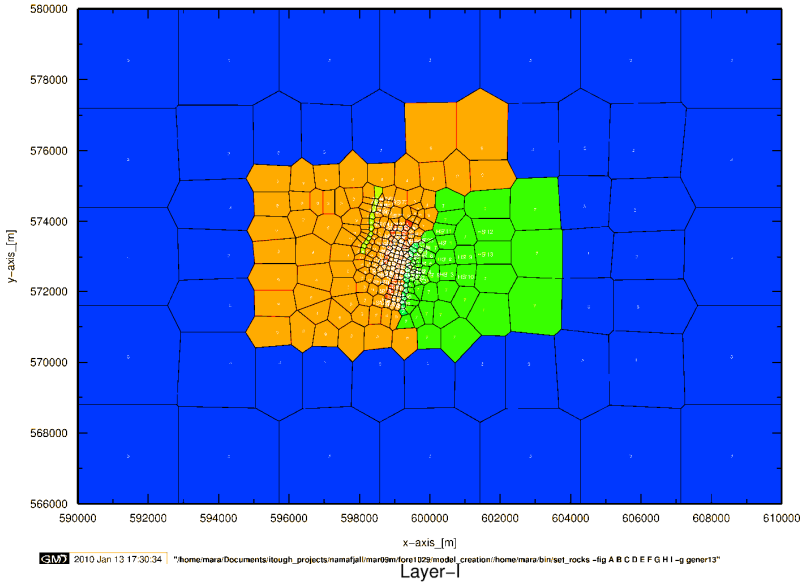

Layer–I

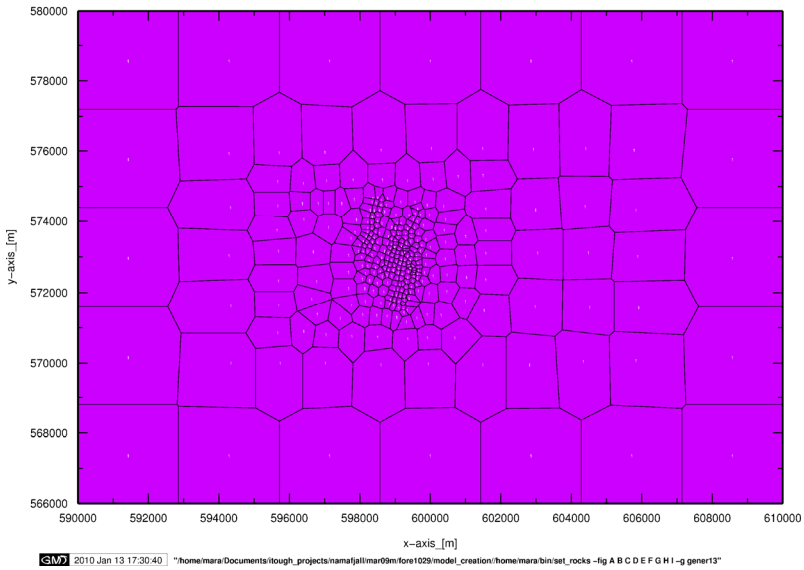

APPENDIX B: Well locations

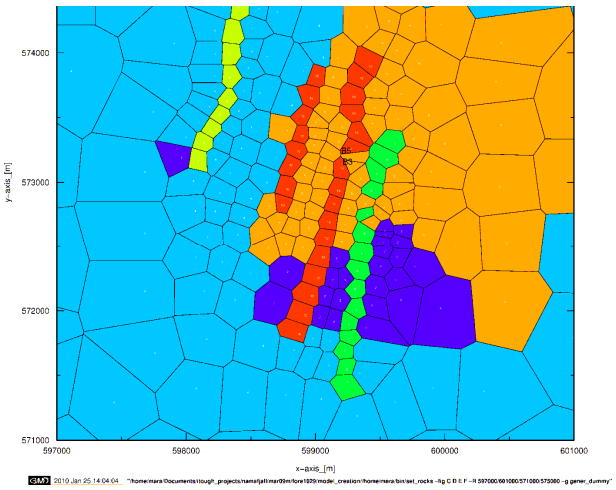

FIGURE 1: Wells in layer C

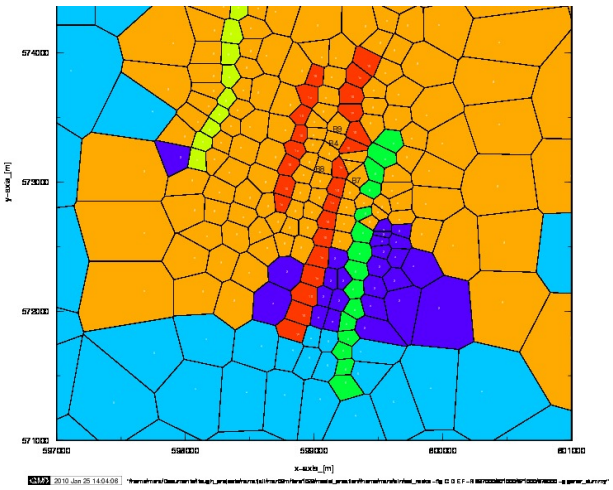

FIGURE 2: Wells in layer D

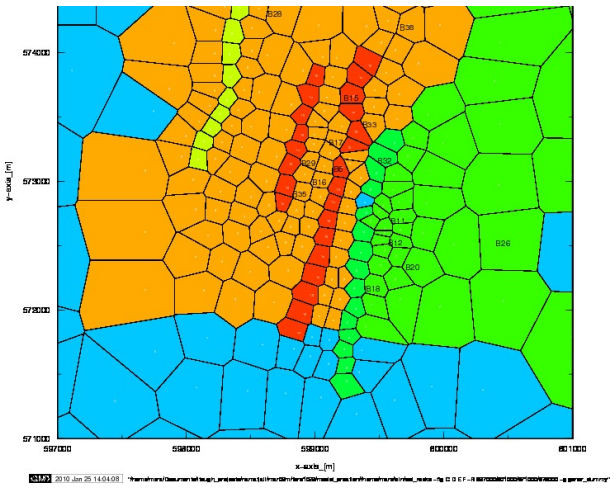

FIGURE 3: Wells in layer E

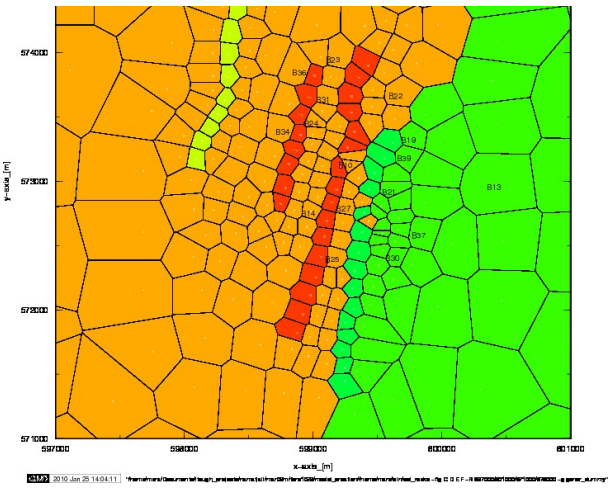

FIGURE 4: Wells in layer F

APPENDIX C: Natural state match (year 1963)

Discrete points are measured values and solid lines are simulated.

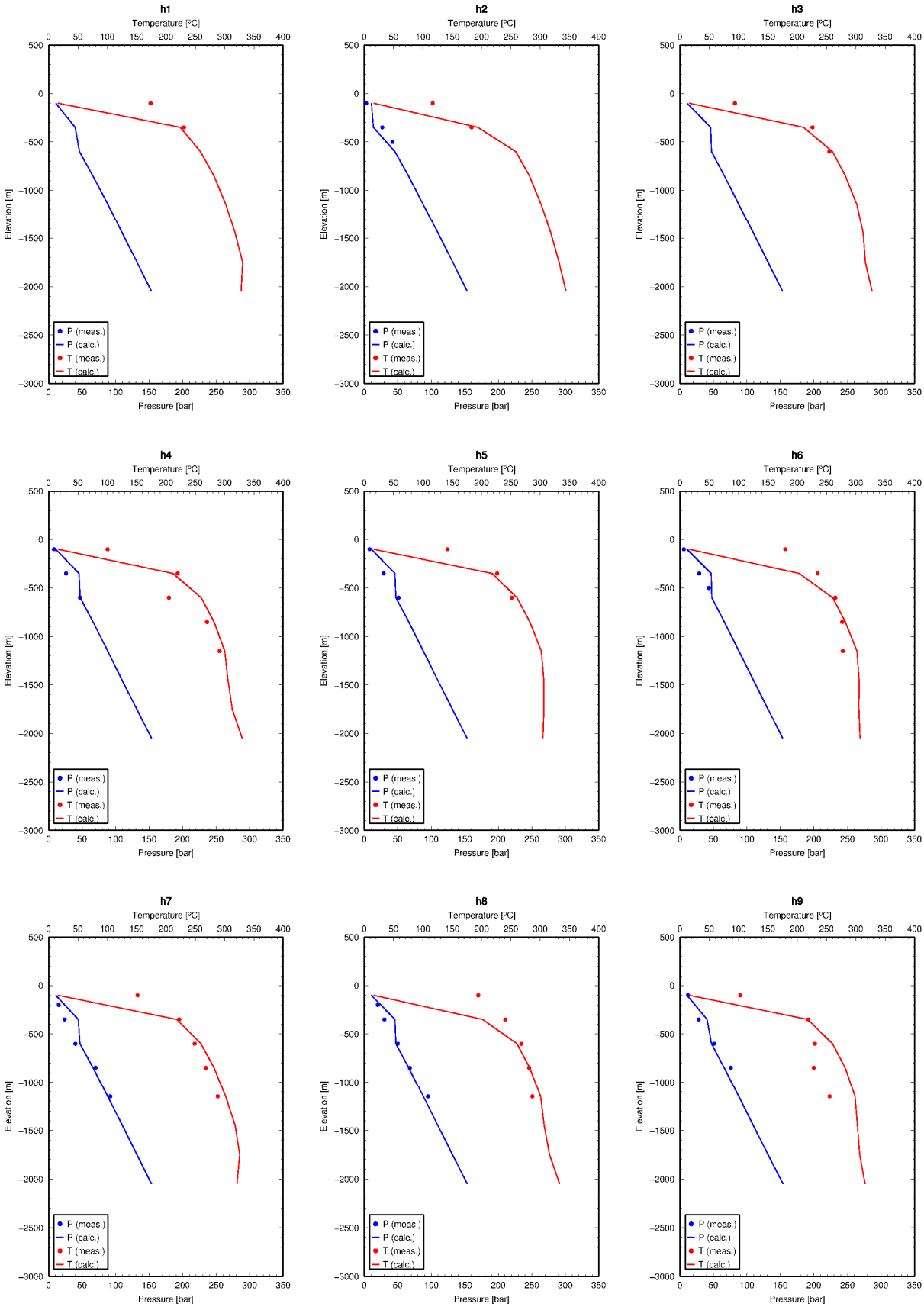

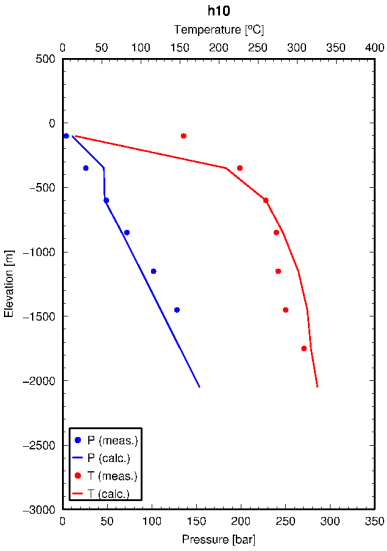
h10
Temperature [°C]
Elevation [m]
Pressure [bar]
P (meas.)
P (calc.)
T (meas.)
T (calc.)

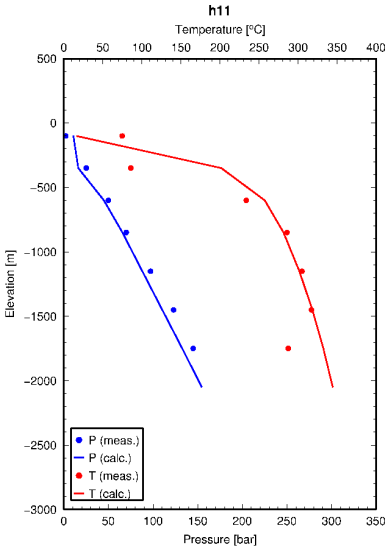
h11
Temperature [°C]
Elevation [m]
Pressure [bar]
P (meas.)
P (calc.)
T (meas.)
T (calc.)

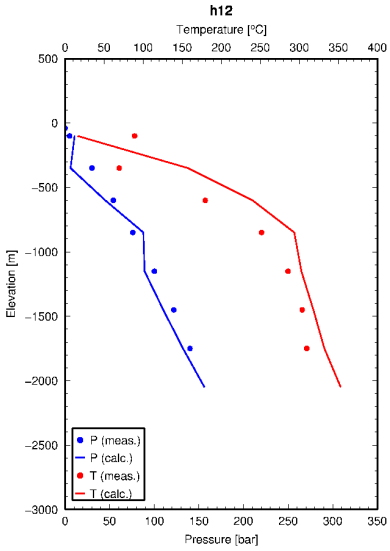
h12
Temperature [°C]
Elevation [m]
Pressure [bar]
P (meas.)
P (calc.)
T (meas.)
T (calc.)

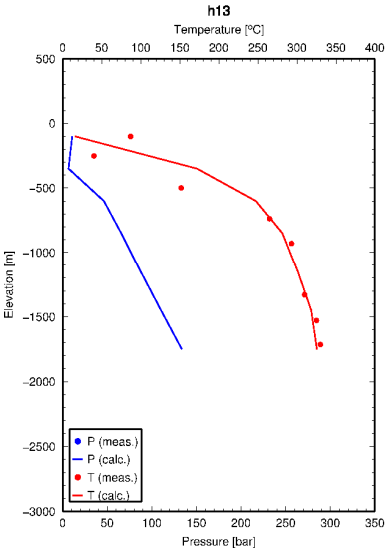
h13
Temperature [°C]
Elevation [m]
Pressure [bar]
P (meas.)
P (calc.)
T (meas.)
T (calc.)

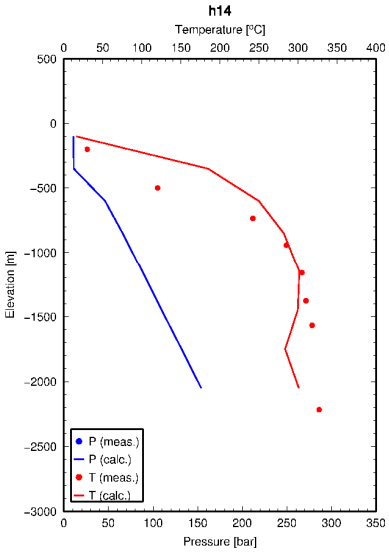
h14
Temperature [°C]
Elevation [m]
Pressure [bar]
P (meas.)
P (calc.)
T (meas.)
T (calc.)

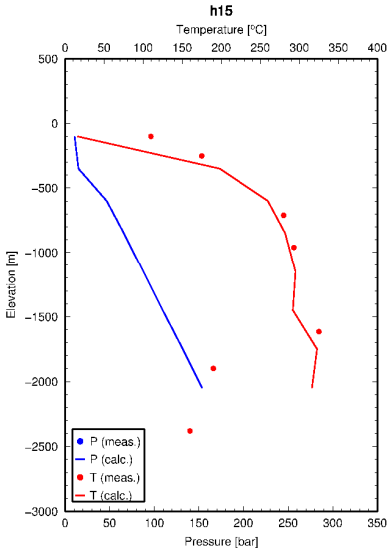
h15
Temperature [°C]
Elevation [m]
Pressure [bar]
P (meas.)
P (calc.)
T (meas.)
T (calc.)

APPENDIX D: History match results

Discrete points are measured and solid lines are simulated values.

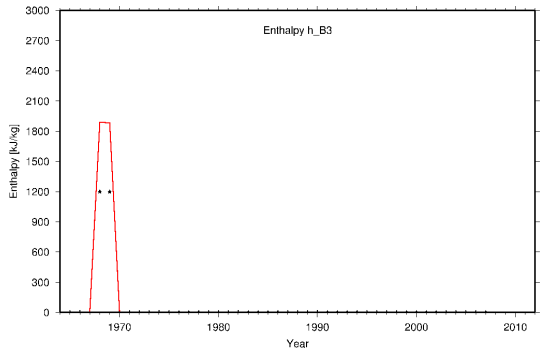

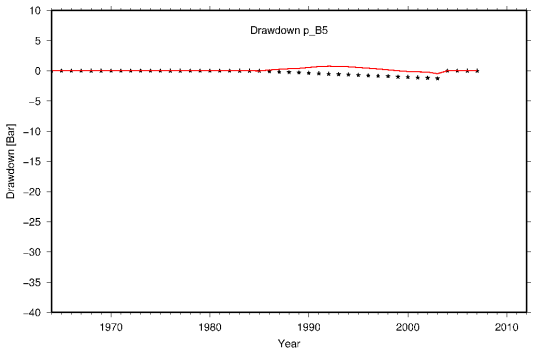

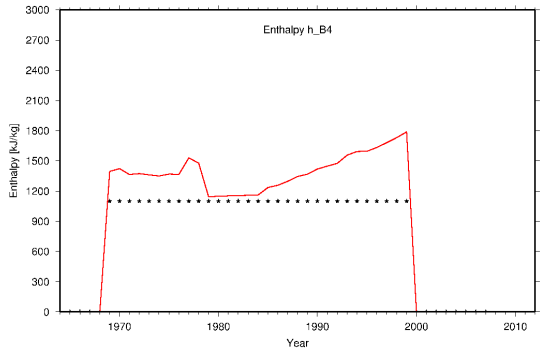

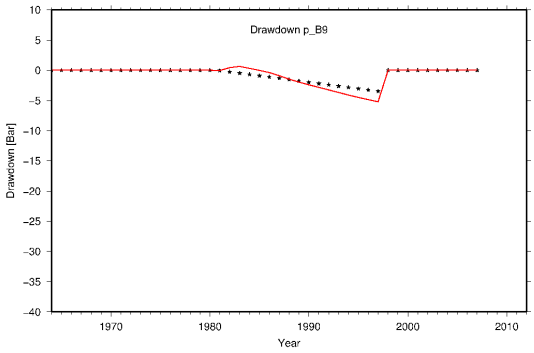

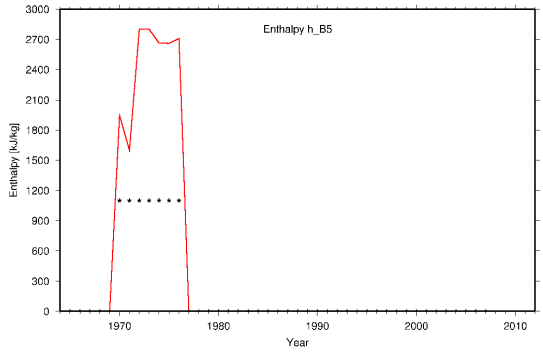

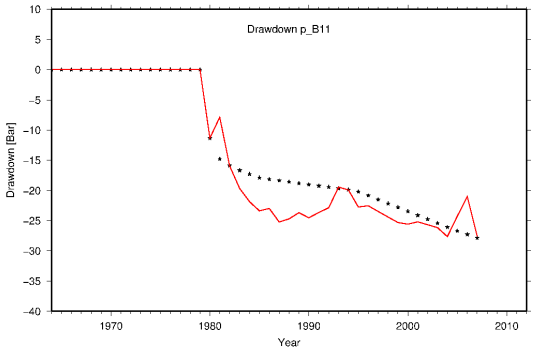

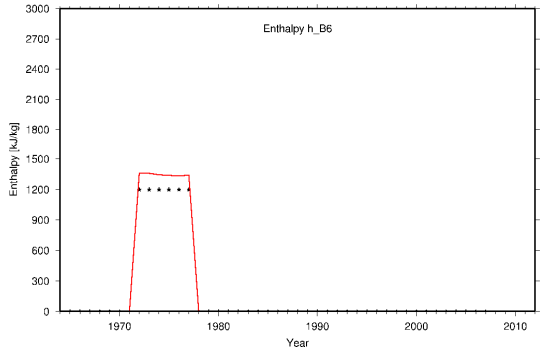

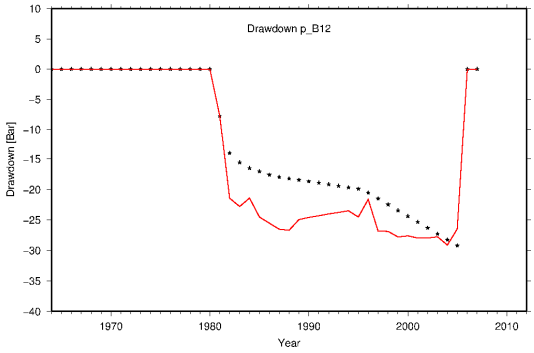

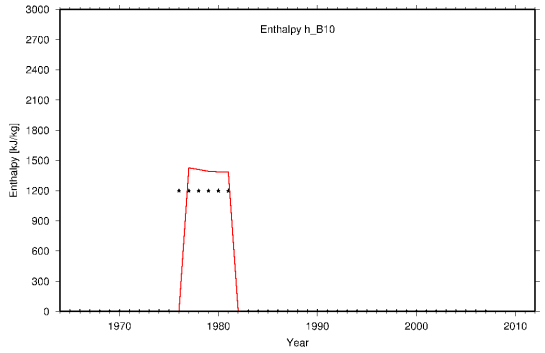
Enthalpy h_B10
Enthalpy [kJ/kg]
Year

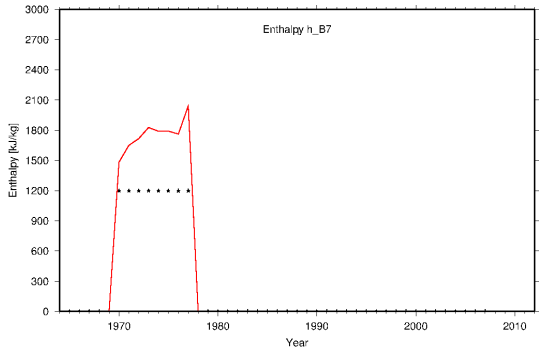
Enthalpy h_B7
Enthalpy [kJ/kg]
Year

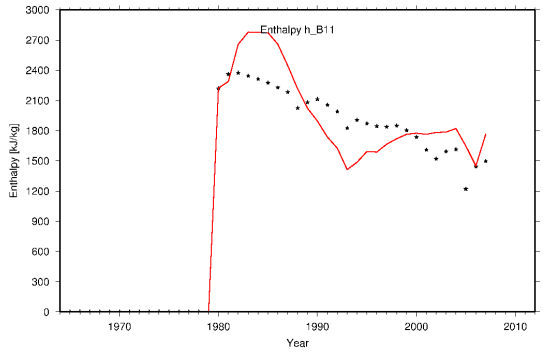
Enthalpy h_B11
Enthalpy [kJ/kg]
Year

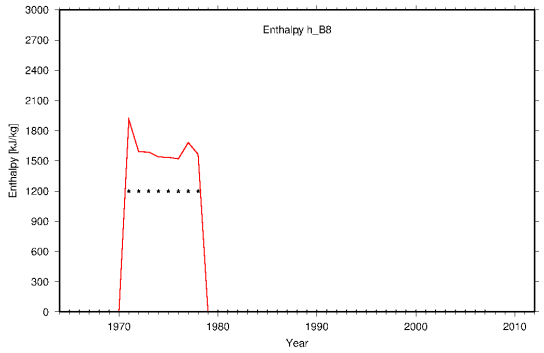
Enthalpy h_B8
Enthalpy [kJ/kg]
Year

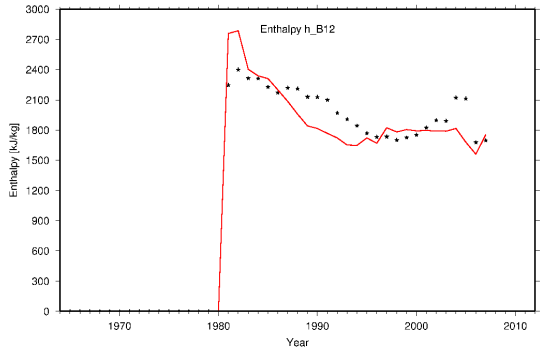
Enthalpy h_B12
Enthalpy [kJ/kg]
Year

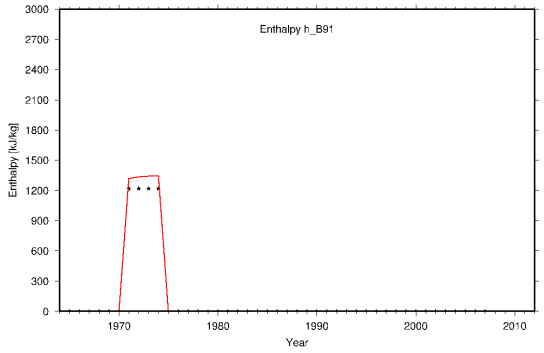
Enthalpy h_B91
Enthalpy [kJ/kg]
Year

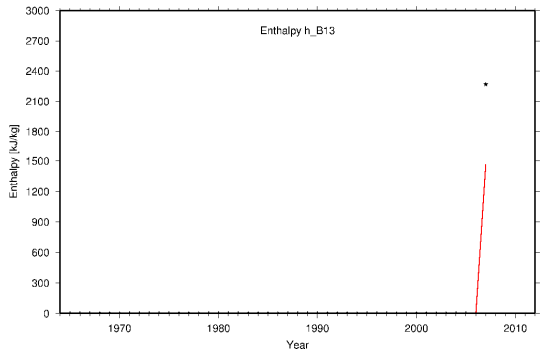
Enthalpy h_B13
Enthalpy [kJ/kg]
Year

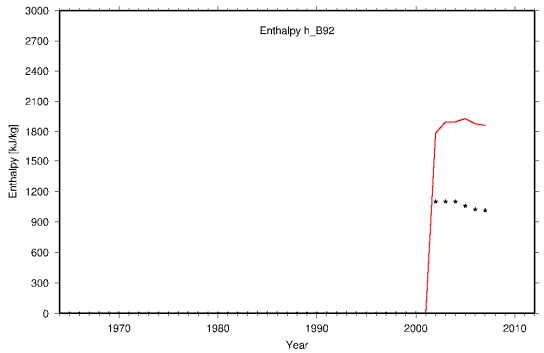
Enthalpy h_B92
Enthalpy [kJ/kg]
Year

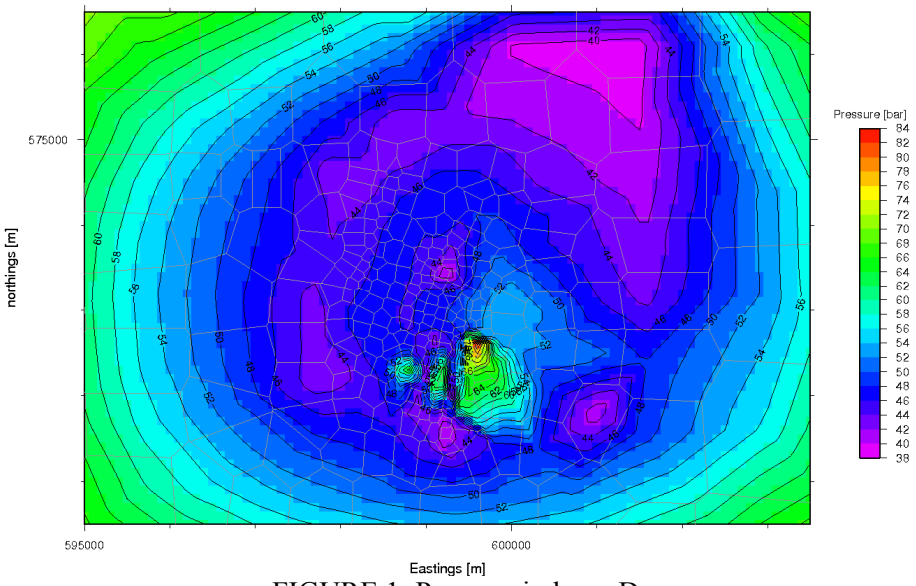

FIGURE 1: Pressure in layer D

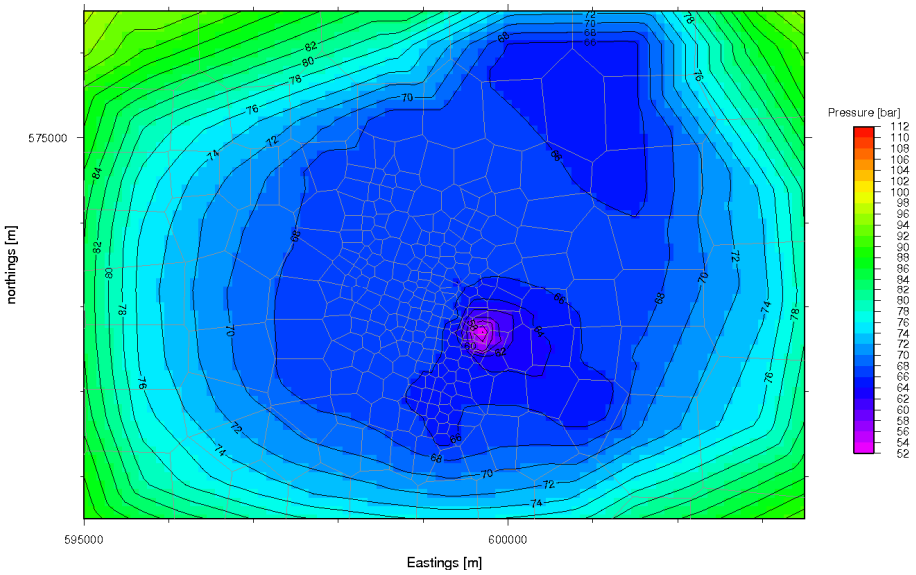

FIGURE 2: Pressure in layer E

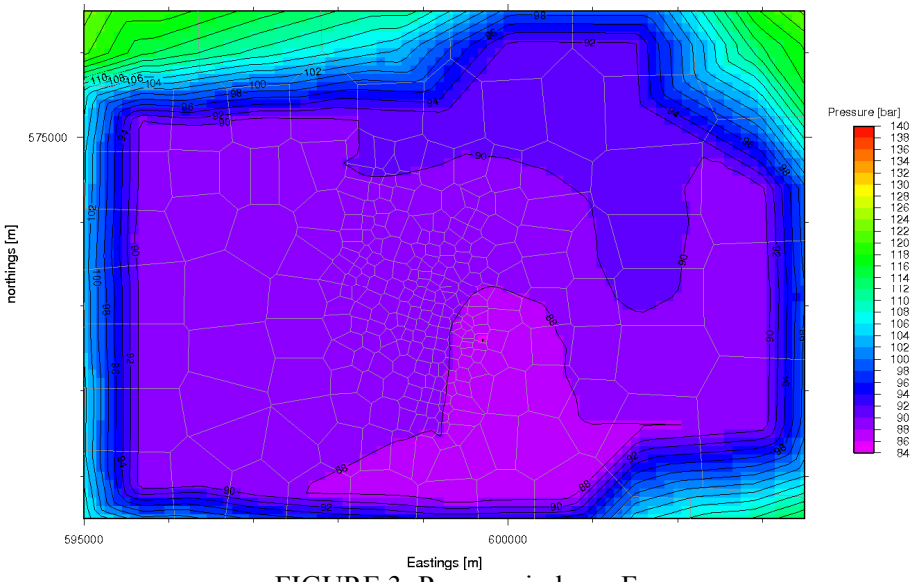

FIGURE 3: Pressure in layer F

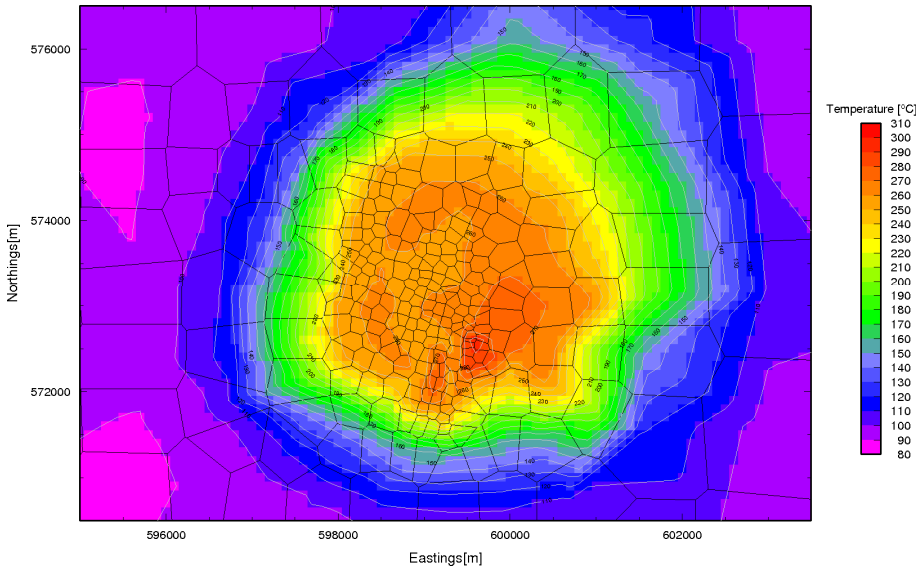

FIGURE 4: Temperature in layer D

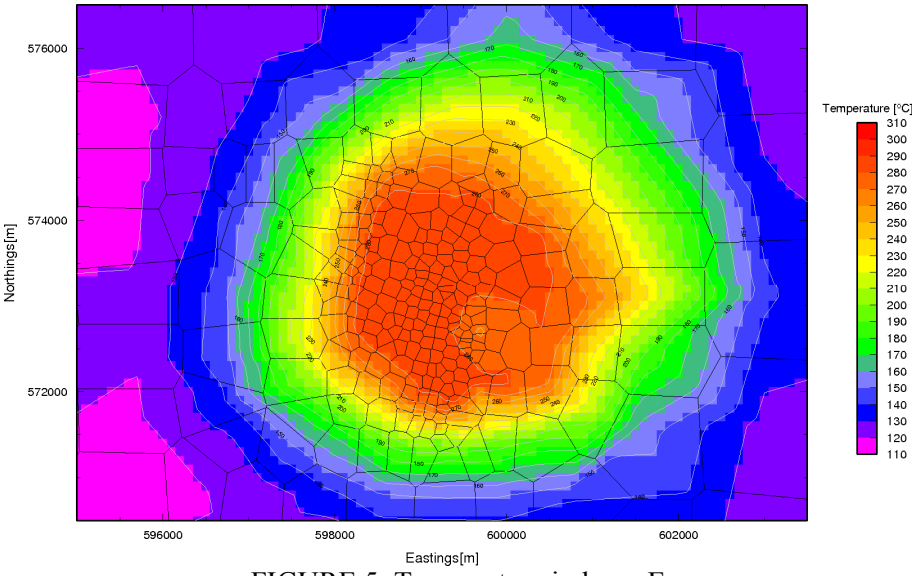

FIGURE 5: Temperature in layer E

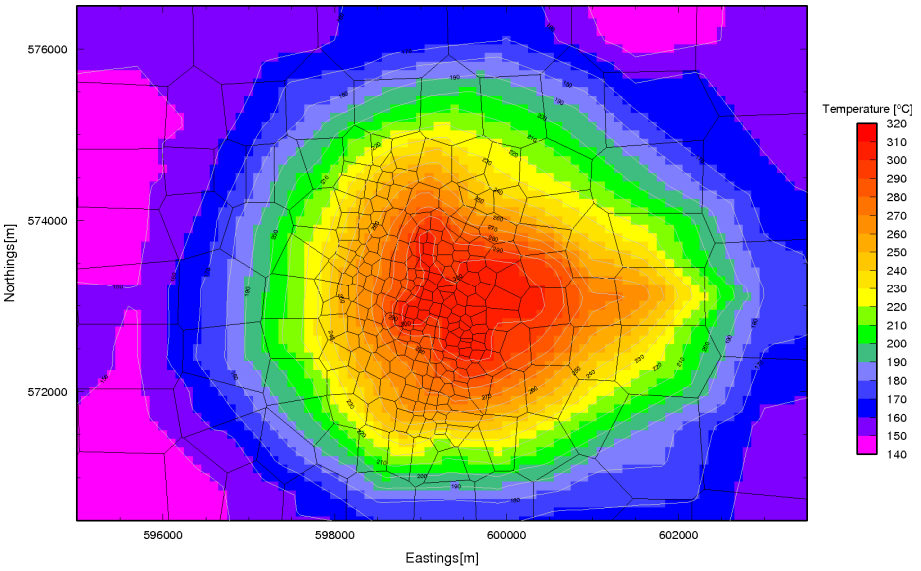

FIGURE 6: Temperature in layer F

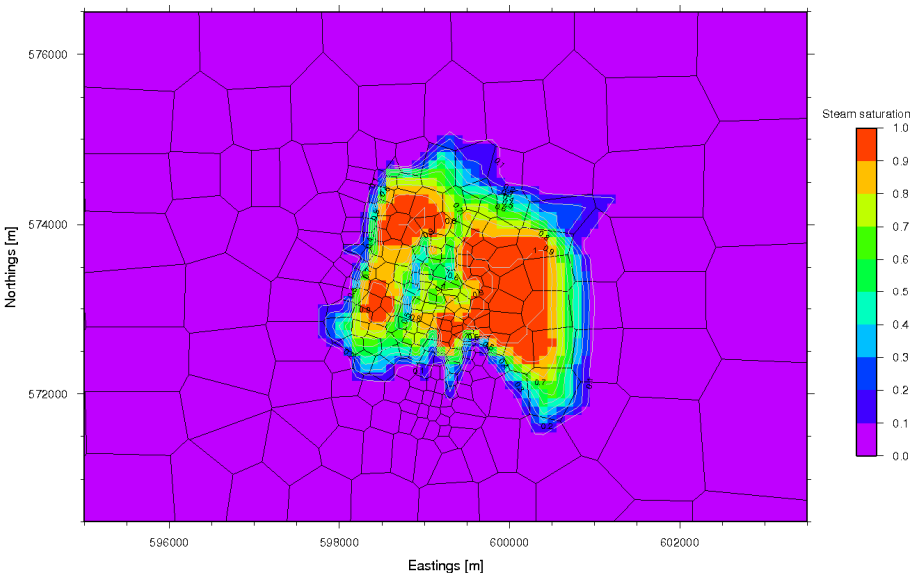

FIGURE 7: Steam saturation in layer D

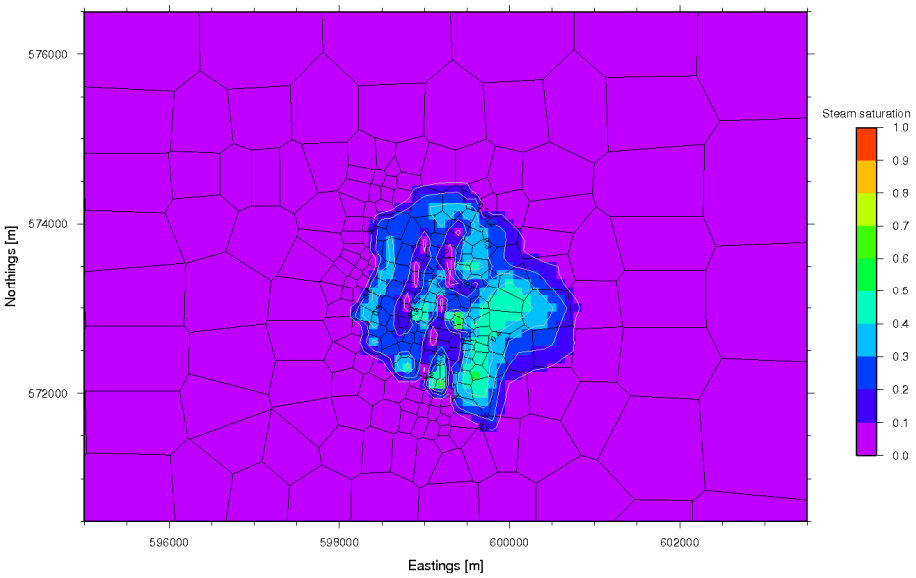

FIGURE 8: Steam saturation in layer E

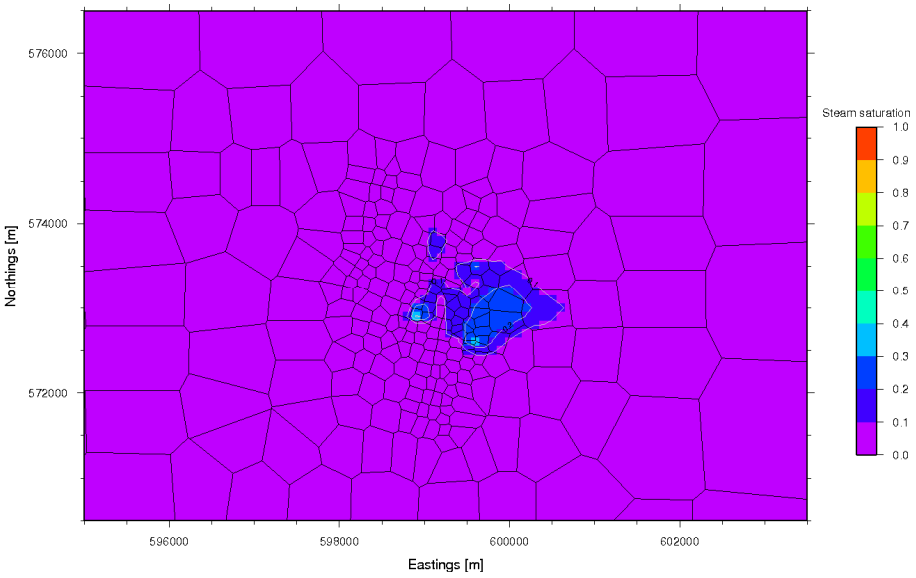

FIGURE 9: Steam saturation in layer F

APPENDIX E: Reservoir in 2045 for the 40 MWe scenario

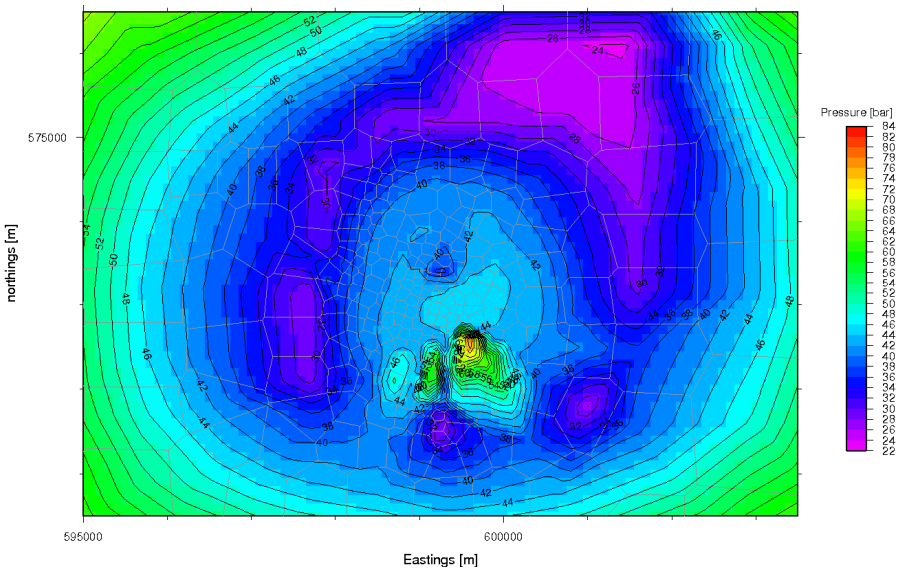

FIGURE 1: Pressure in layer D

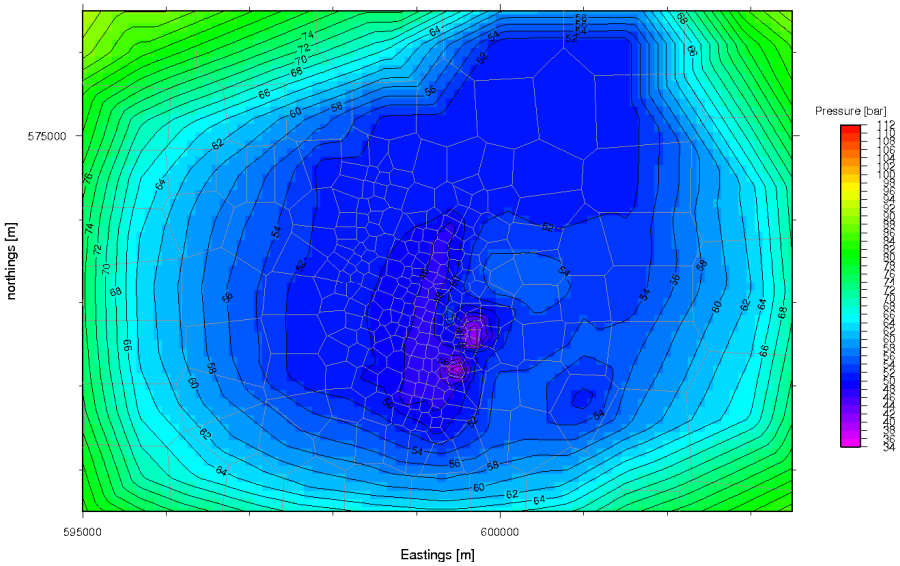

FIGURE 2: Pressure in layer E

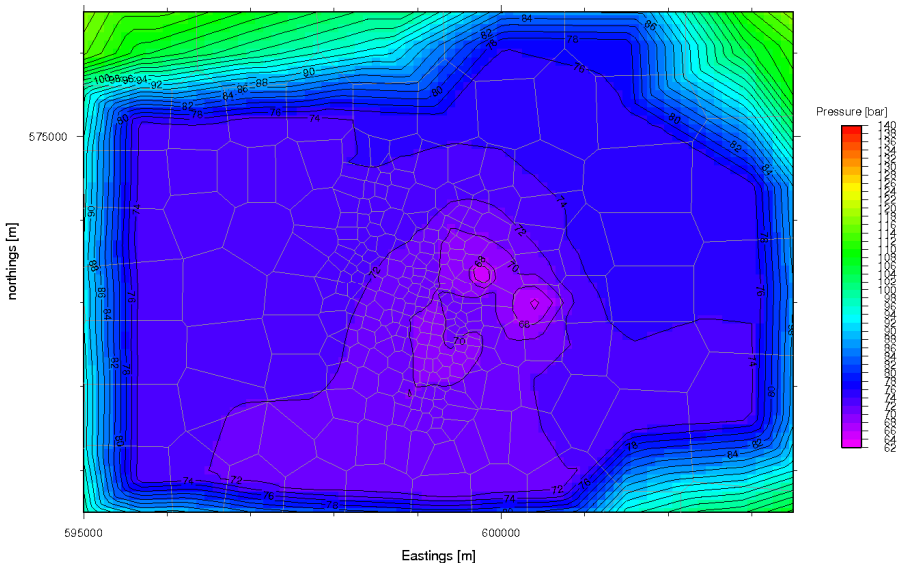

FIGURE 3: Pressure in layer F

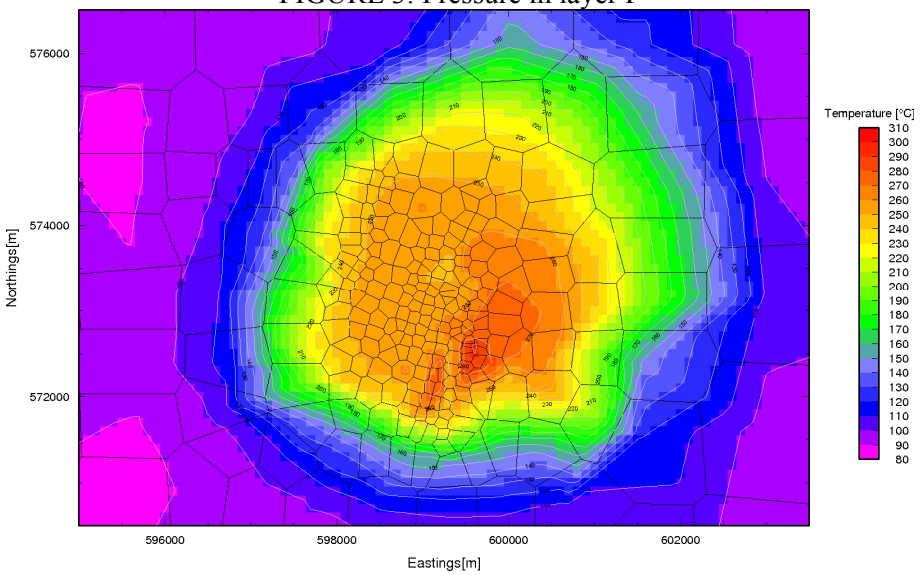

FIGURE 4: Temperature in layer D

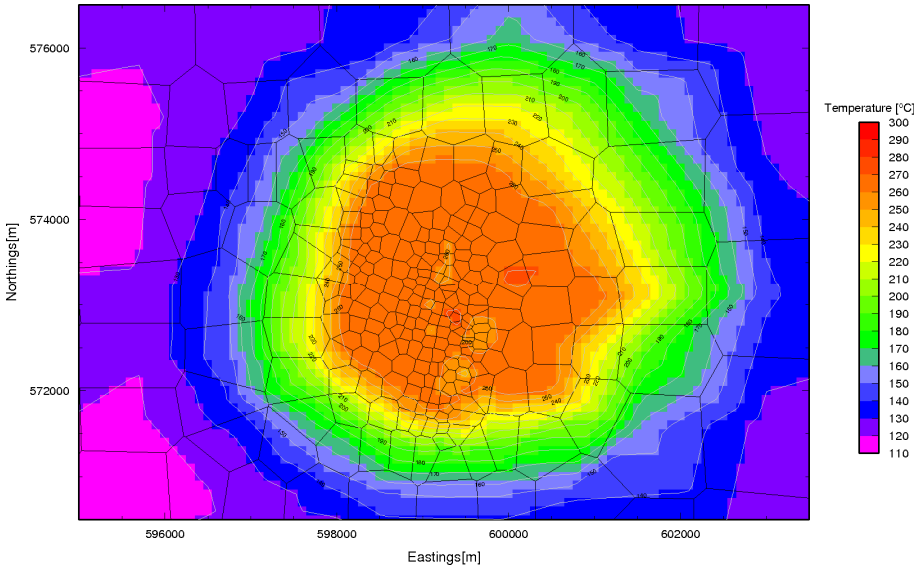

FIGURE 5: Temperature in layer E

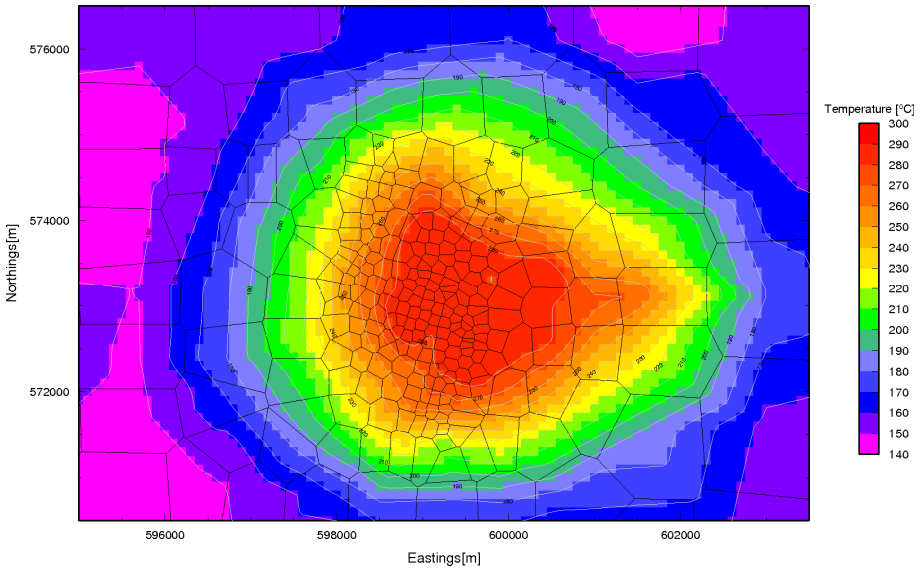

FIGURE 6: Temperature in layer F

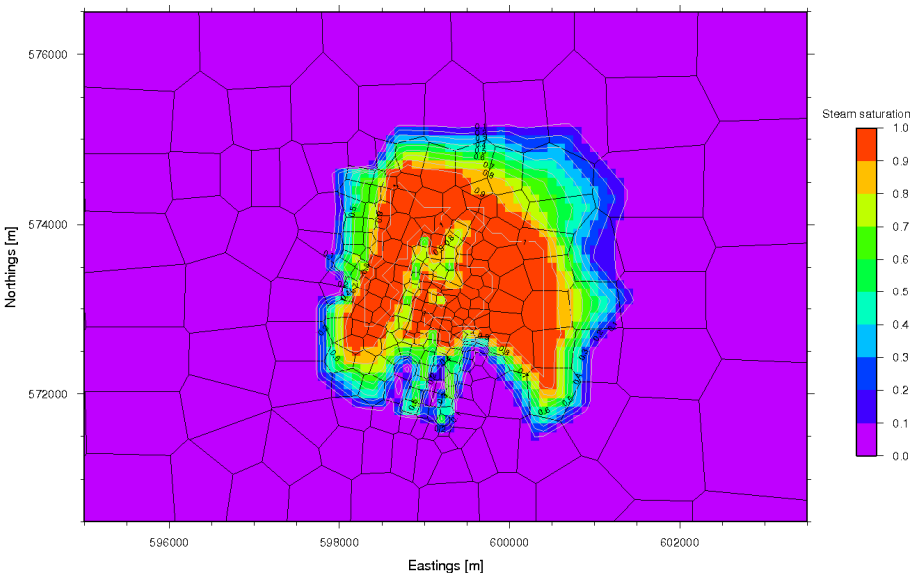

FIGURE 7: Steam saturation in layer D

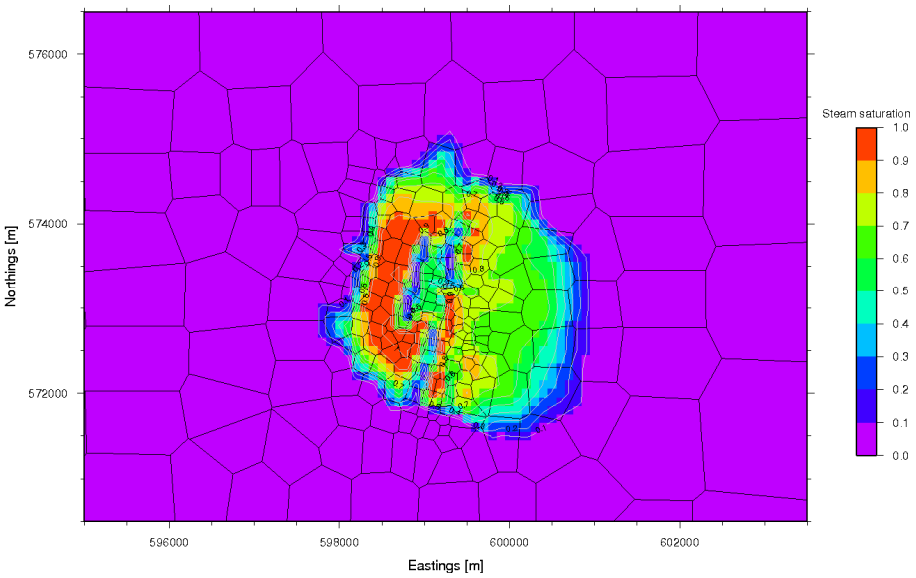

FIGURE 8: Steam saturation in layer E

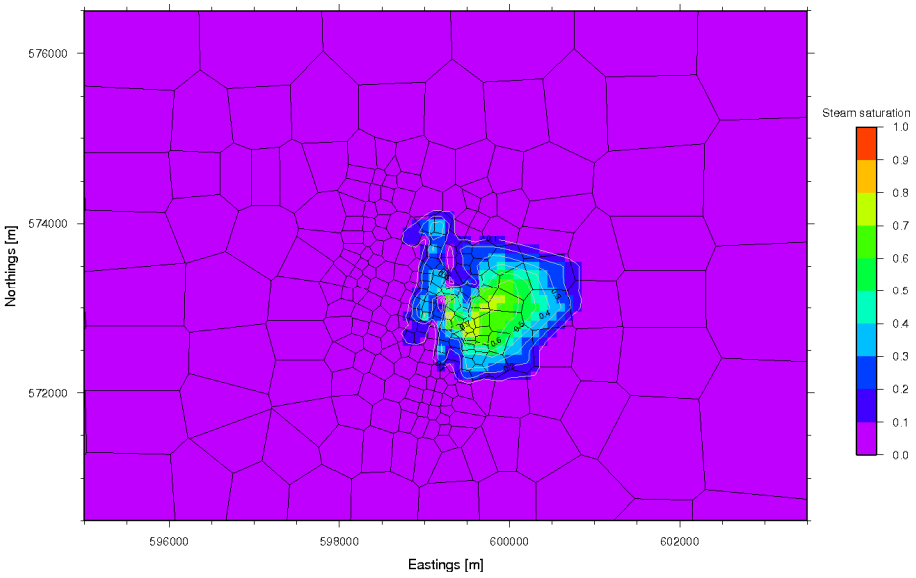

FIGURE 9: Steam saturation in layer F

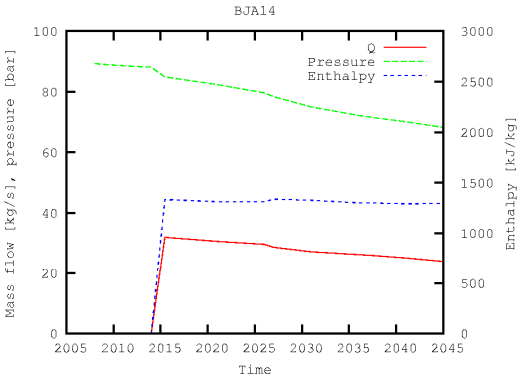
BJA14
Q
Pressure
Enthalpy
Mass flow [kg/s], pressure [bar]
Enthalpy [kJ/kg]
Time

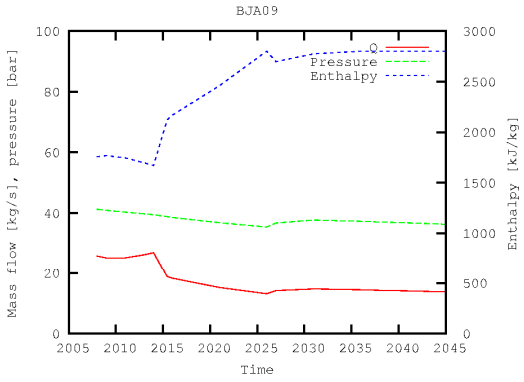
BJA09
Q
Pressure
Enthalpy
Mass flow [kg/s], pressure [bar]
Enthalpy [kJ/kg]
Time

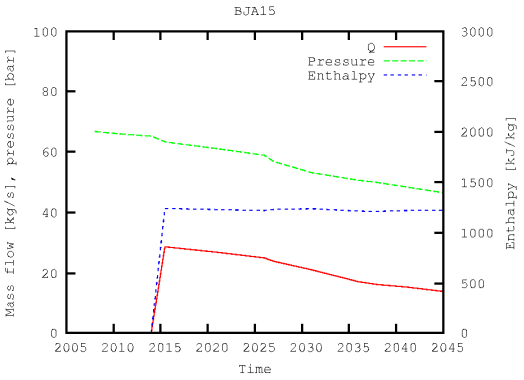
BJA15
Q
Pressure
Enthalpy
Mass flow [kg/s], pressure [bar]
Enthalpy [kJ/kg]
Time

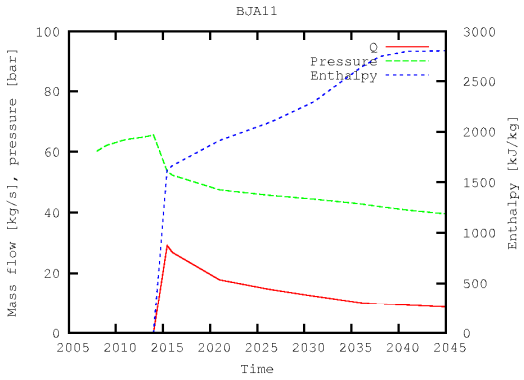
BJA11
Q
Pressure
Enthalpy
Mass flow [kg/s], pressure [bar]
Enthalpy [kJ/kg]
Time

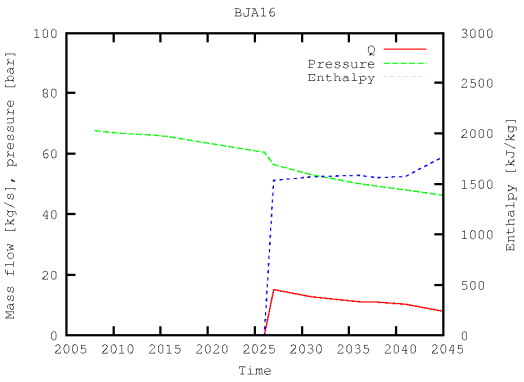
BJA16
Q
Pressure
Enthalpy
Mass flow [kg/s], pressure [bar]
Enthalpy [kJ/kg]
Time

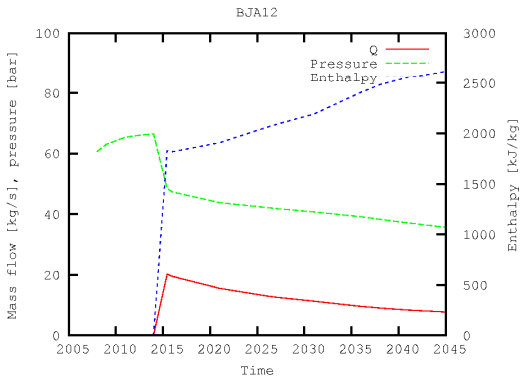
BJA12
Q
Pressure
Enthalpy
Mass flow [kg/s], pressure [bar]
Enthalpy [kJ/kg]
Time

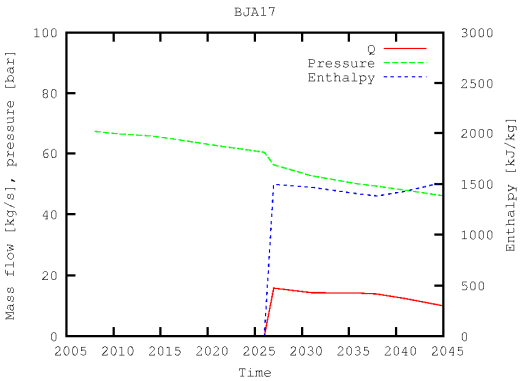
BJA17
Q
Pressure
Enthalpy
Mass flow [kg/s], pressure [bar]
Enthalpy [kJ/kg]
Time

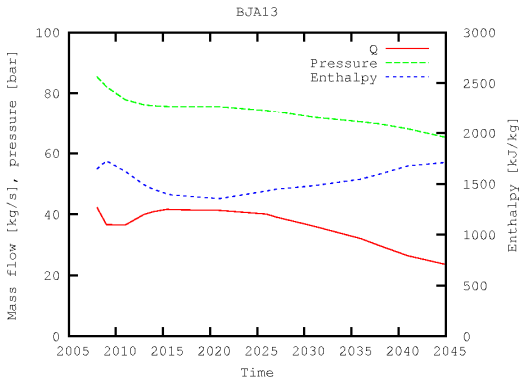
BJA13
Q
Pressure
Enthalpy
Mass flow [kg/s], pressure [bar]
Enthalpy [kJ/kg]
Time

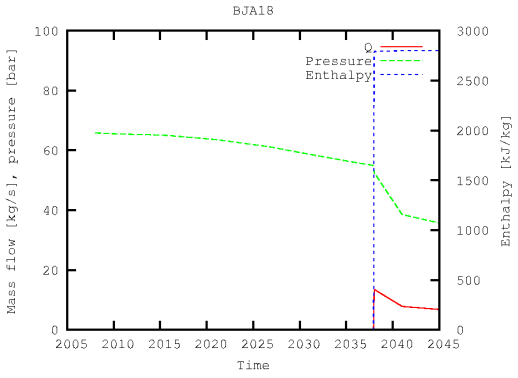
BJA18
Q
Pressure
Enthalpy
Mass flow [kg/s], pressure [bar]
Enthalpy [kJ/kg]
Time
0
20
40
60
80
100
0
500
1000
1500
2000
2500
3000
2005
2010
2015
2020
2025
2030
2035
2040
2045

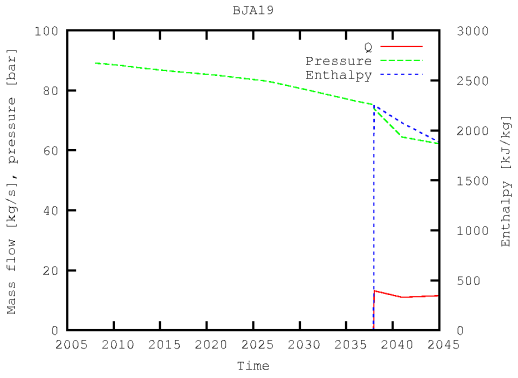
BJA19
Q
Pressure
Enthalpy
Mass flow [kg/s], pressure [bar]
Enthalpy [kJ/kg]
Time
0
20
40
60
80
100
0
500
1000
1500
2000
2500
3000
2005
2010
2015
2020
2025
2030
2035
2040
2045

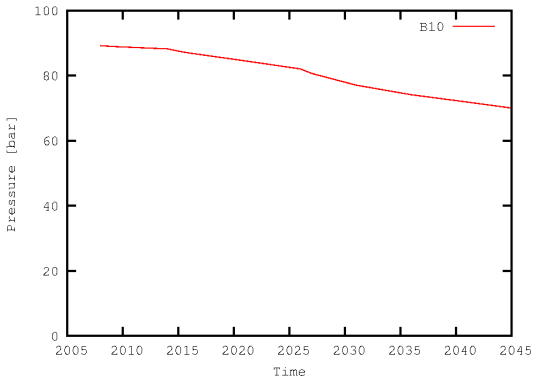
B10
Pressure [bar]
Time
0
20
40
60
80
100
2005
2010
2015
2020
2025
2030
2035
2040
2045

APPENDIX F: Reservoir in 2045 for the 60 MWe scenario

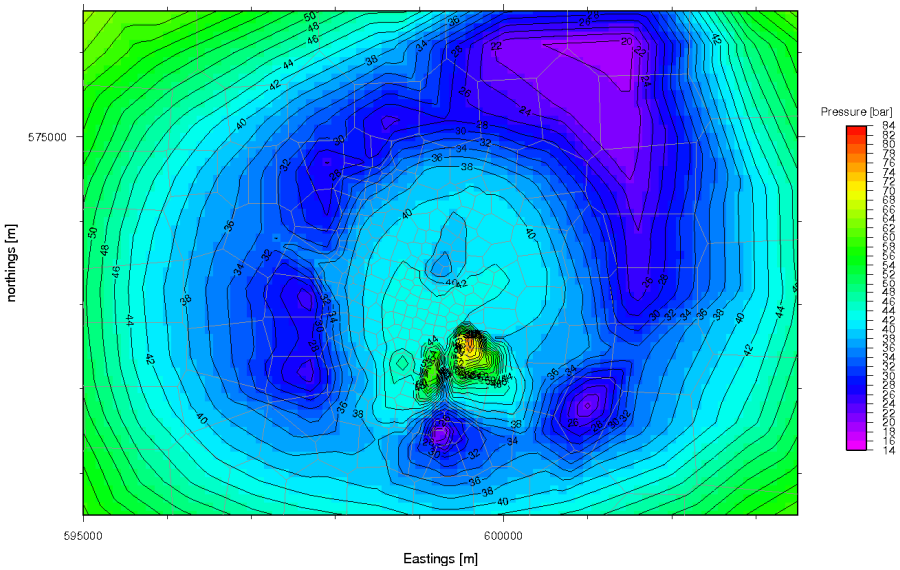

FIGURE 1: Pressure in layer D

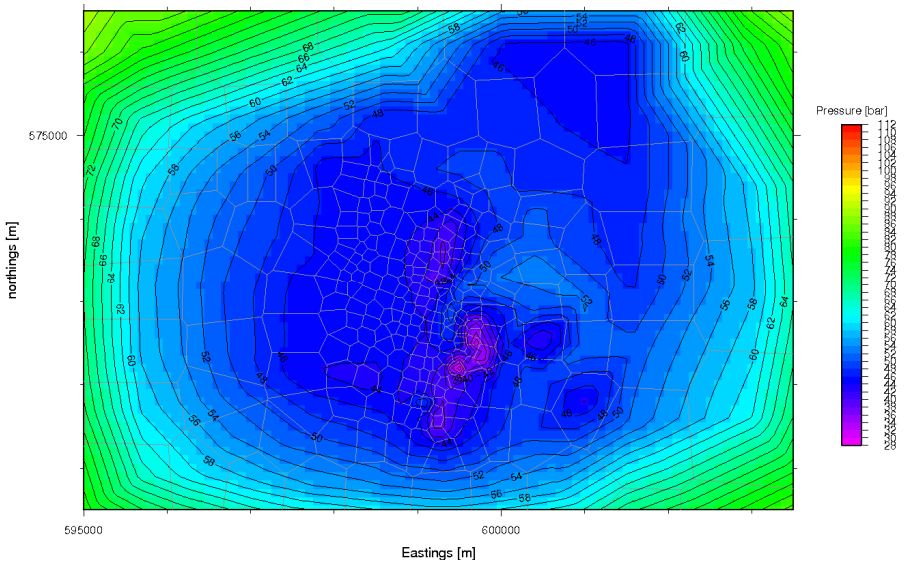

FIGURE 2: Pressure in layer E

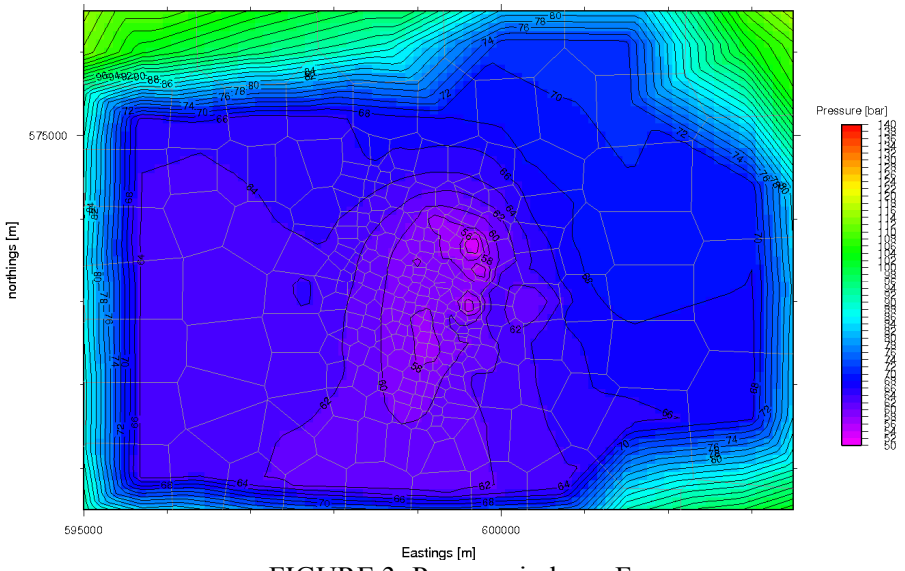

FIGURE 3: Pressure in layer F

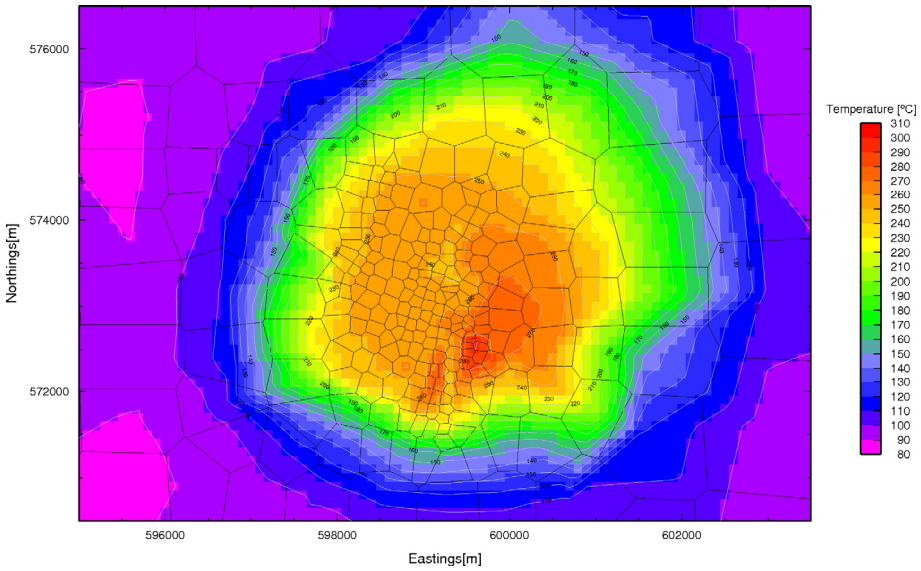

FIGURE 4: Temperature in layer D

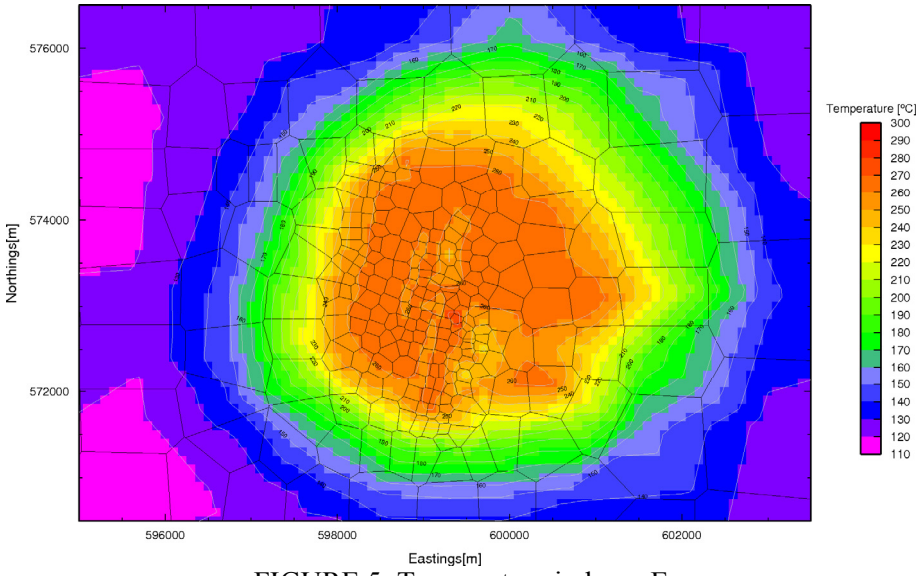

FIGURE 5: Temperature in layer E

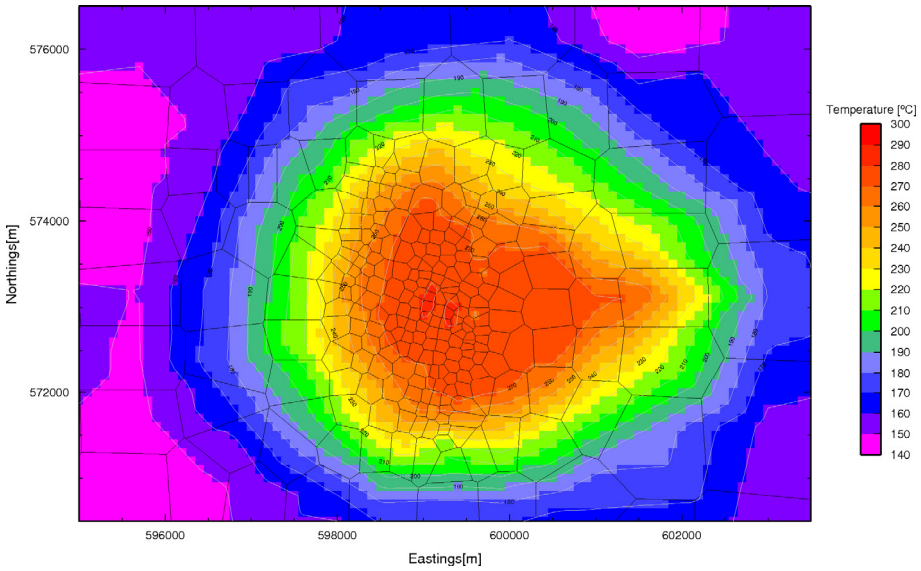

FIGURE 6: Temperature in layer F

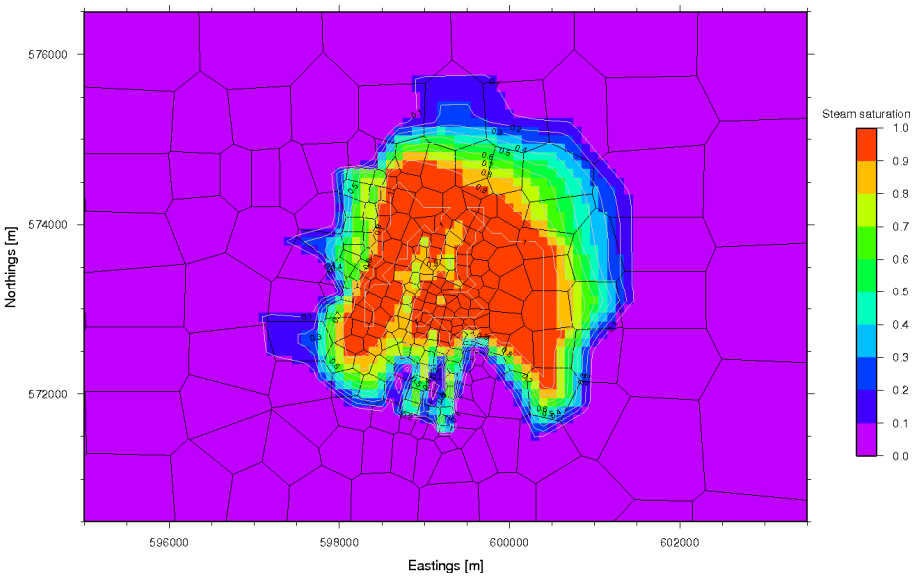

FIGURE 7: Steam saturation in layer D

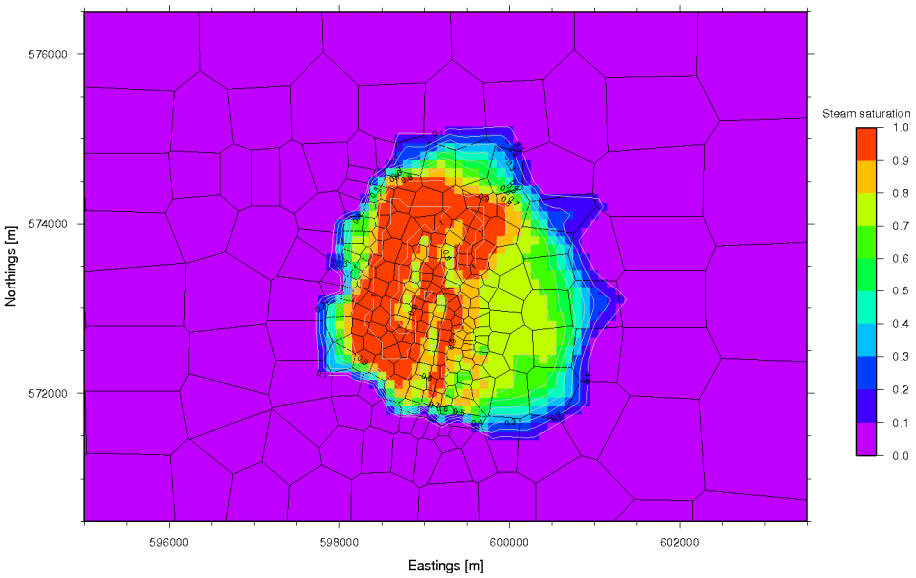

FIGURE 8: Steam saturation in layer E

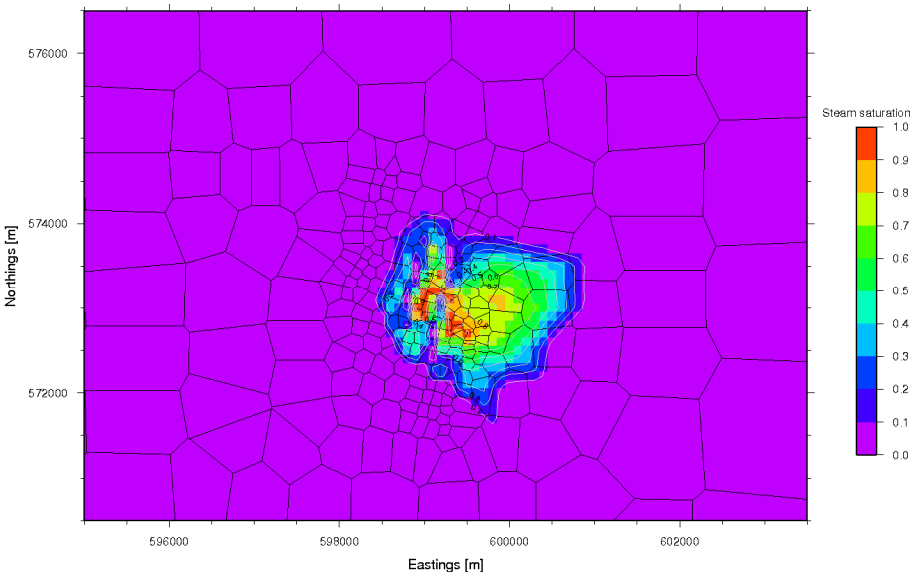

FIGURE 9: Steam saturation in layer F

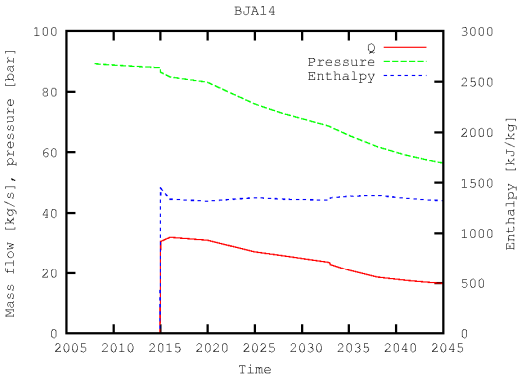
BJA14
Q
Pressure
Enthalpy
Mass flow [kg/s], pressure [bar]
Enthalpy [kJ/kg]
Time

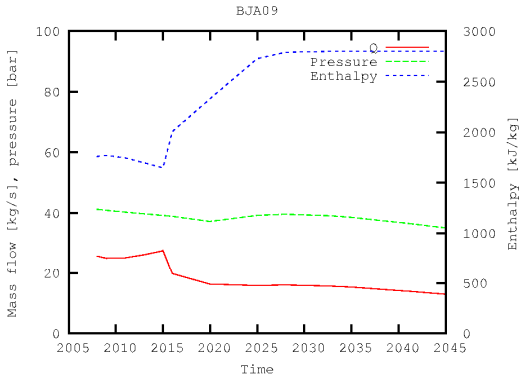
BJA09
Q
Pressure
Enthalpy
Mass flow [kg/s], pressure [bar]
Enthalpy [kJ/kg]
Time

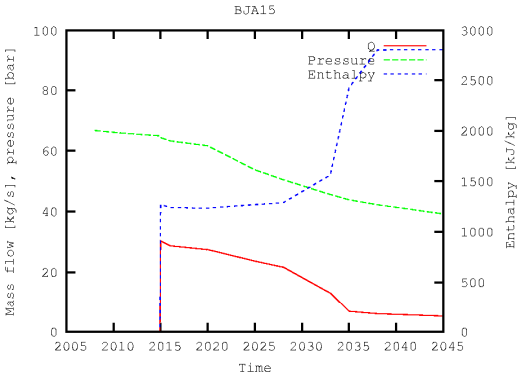
BJA15
Q
Pressure
Enthalpy
Mass flow [kg/s], pressure [bar]
Enthalpy [kJ/kg]
Time

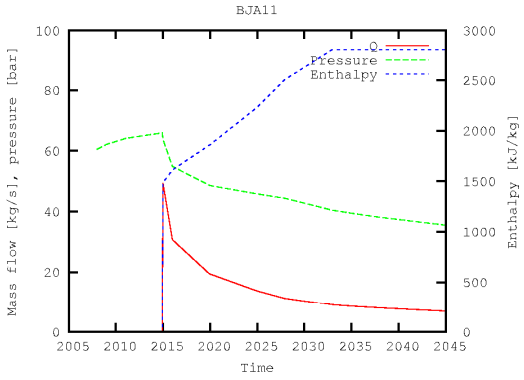
BJA11
Q
Pressure
Enthalpy
Mass flow [kg/s], pressure [bar]
Enthalpy [kJ/kg]
Time

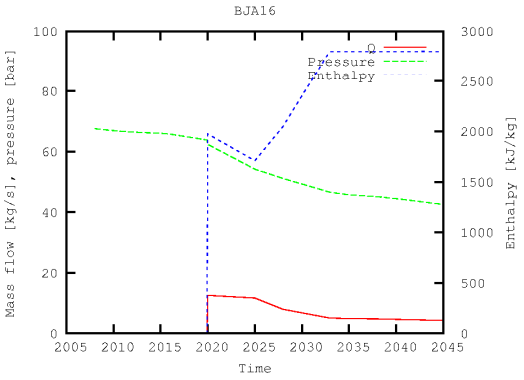
BJA16
Q
Pressure
Enthalpy
Mass flow [kg/s], pressure [bar]
Enthalpy [kJ/kg]
Time

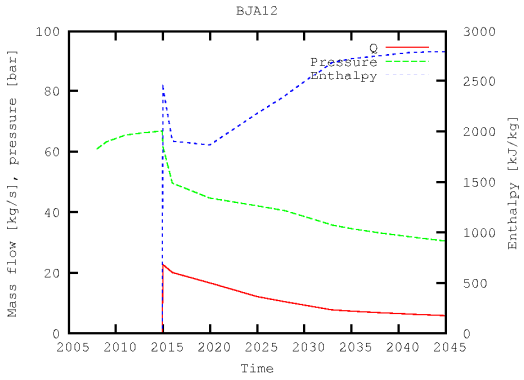
BJA12
Q
Pressure
Enthalpy
Mass flow [kg/s], pressure [bar]
Enthalpy [kJ/kg]
Time

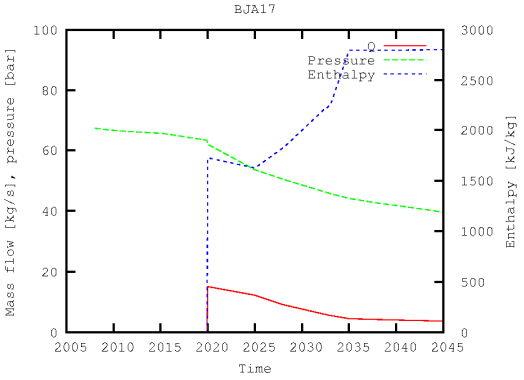
BJA17
Q
Pressure
Enthalpy
Mass flow [kg/s], pressure [bar]
Enthalpy [kJ/kg]
Time

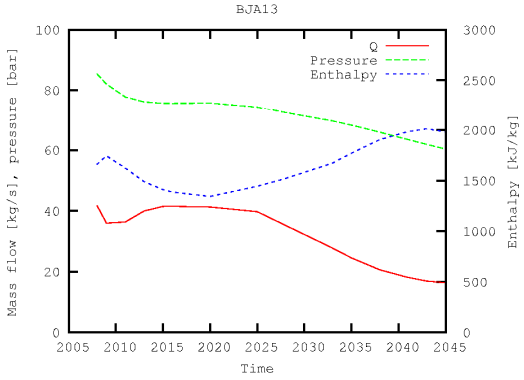
BJA13
Q
Pressure
Enthalpy
Mass flow [kg/s], pressure [bar]
Enthalpy [kJ/kg]
Time

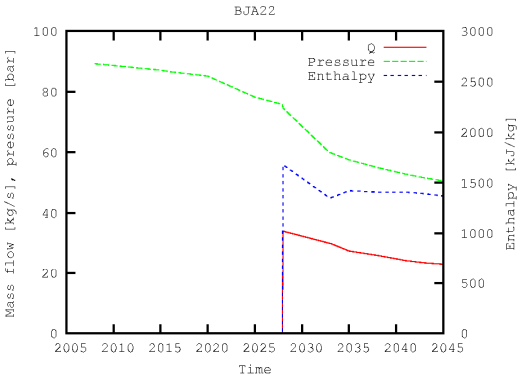
BJA22
Q
Pressure
Enthalpy
Mass flow [kg/s], pressure [bar]
Enthalpy [kJ/kg]
Time

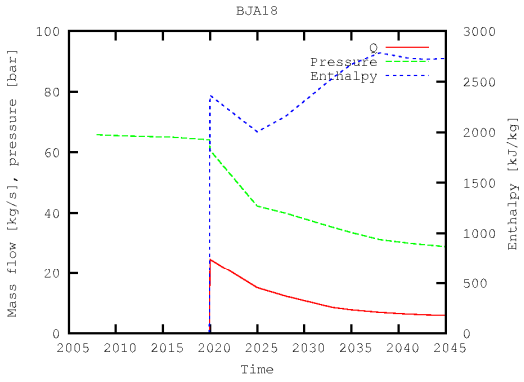
BJA18
Q
Pressure
Enthalpy
Mass flow [kg/s], pressure [bar]
Enthalpy [kJ/kg]
Time

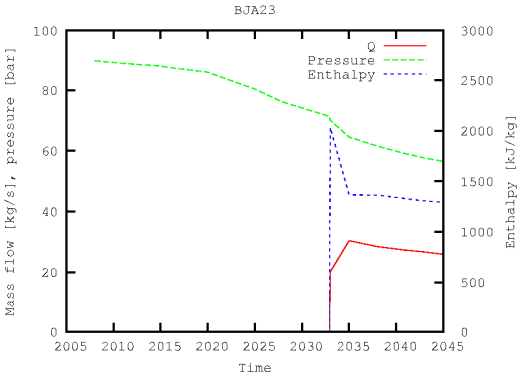
BJA23
Q
Pressure
Enthalpy
Mass flow [kg/s], pressure [bar]
Enthalpy [kJ/kg]
Time

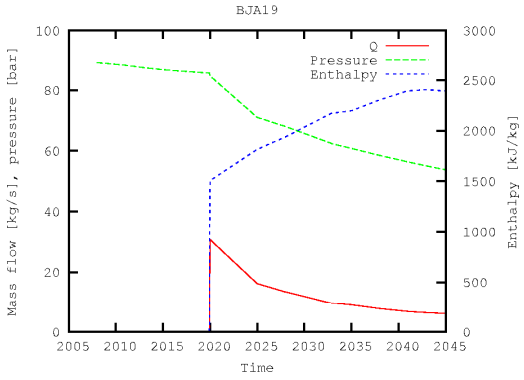
BJA19
Q
Pressure
Enthalpy
Mass flow [kg/s], pressure [bar]
Enthalpy [kJ/kg]
Time

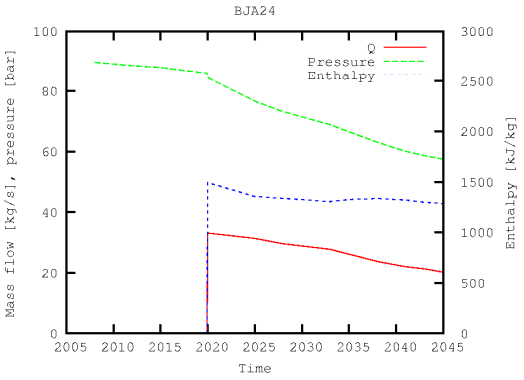
BJA24
Q
Pressure
Enthalpy
Mass flow [kg/s], pressure [bar]
Enthalpy [kJ/kg]
Time

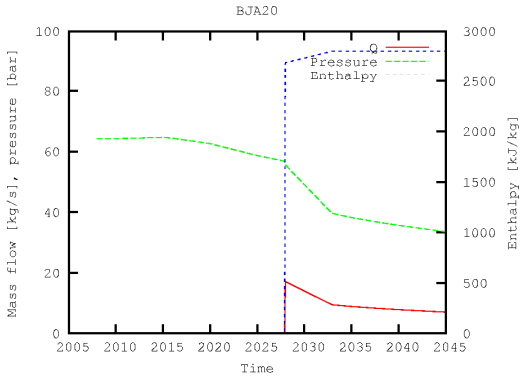
BJA20
Q
Pressure
Enthalpy
Mass flow [kg/s], pressure [bar]
Enthalpy [kJ/kg]
Time

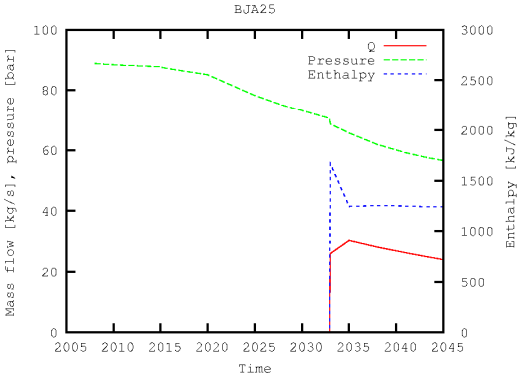
BJA25
Q
Pressure
Enthalpy
Mass flow [kg/s], pressure [bar]
Enthalpy [kJ/kg]
Time

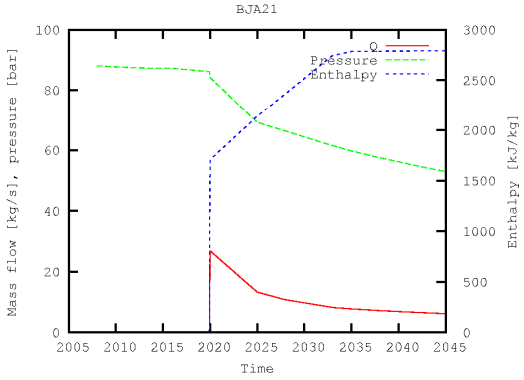
BJA21
Q
Pressure
Enthalpy
Mass flow [kg/s], pressure [bar]
Enthalpy [kJ/kg]
Time

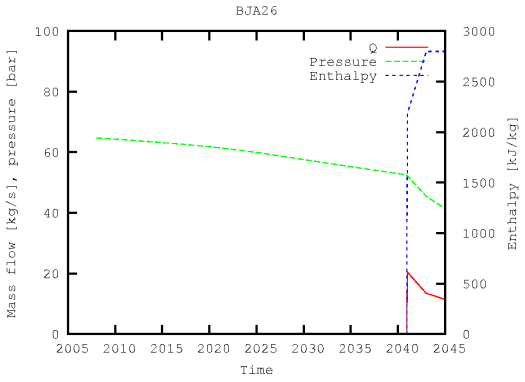
BJA26
Q
Pressure
Enthalpy
Mass flow [kg/s], pressure [bar]
Enthalpy [kJ/kg]
Time
0
20
40
60
80
100
0
500
1000
1500
2000
2500
3000
2005
2010
2015
2020
2025
2030
2035
2040
2045

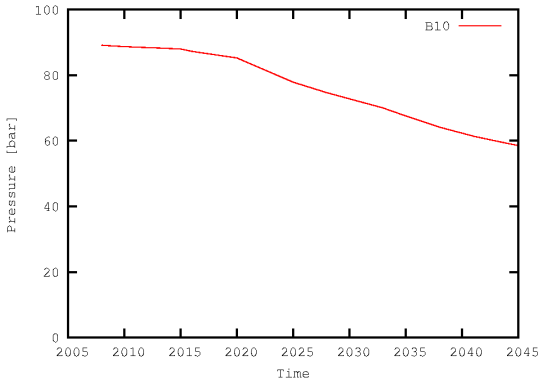
B10
Pressure [bar]
Time
0
20
40
60
80
100
2005
2010
2015
2020
2025
2030
2035
2040
2045

APPENDIX G: Reservoir in 2045 for the 90 MWe scenario

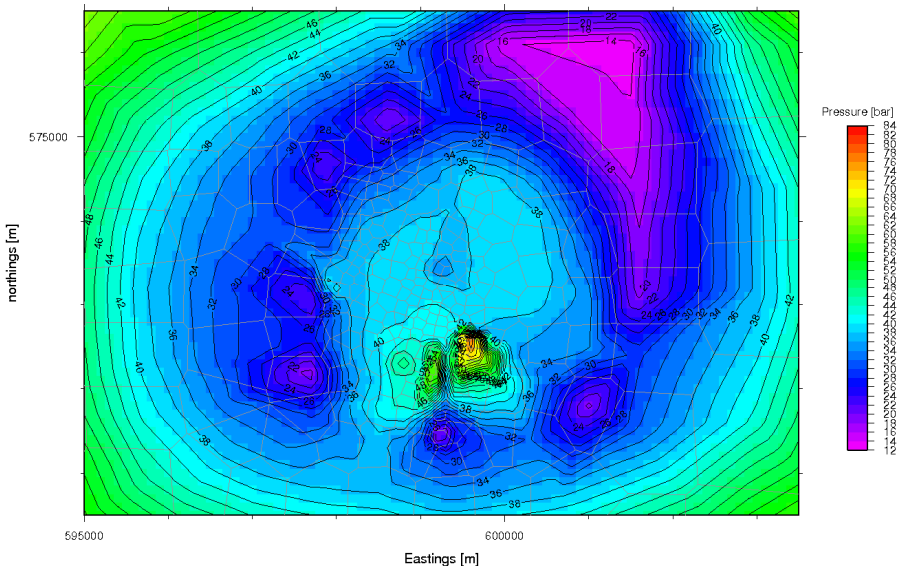

FIGURE 1: Pressure in layer D

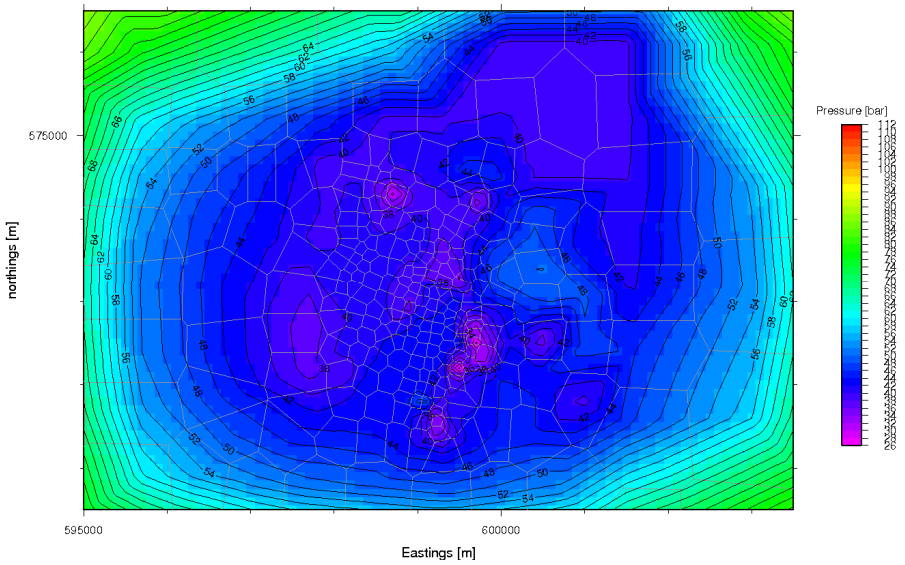

FIGURE 2: Pressure in layer E

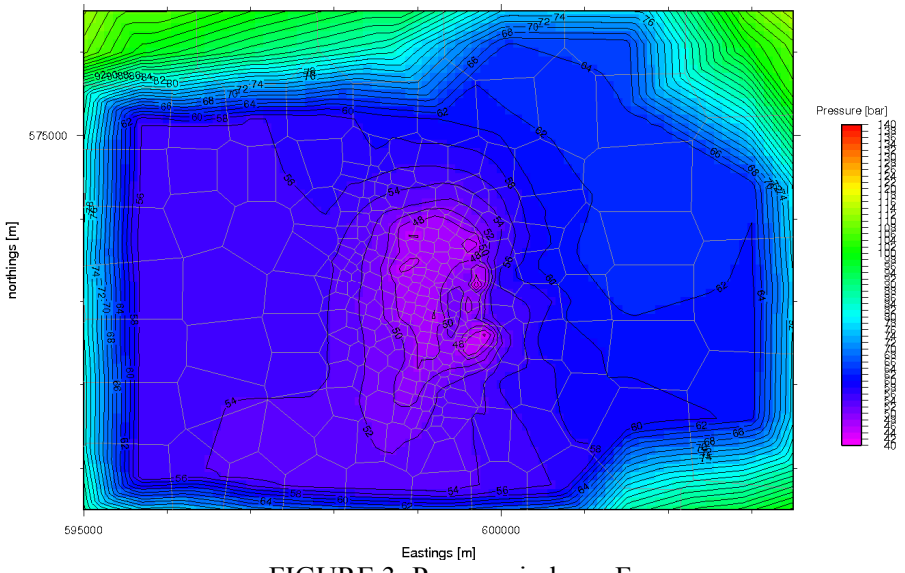

FIGURE 3: Pressure in layer F

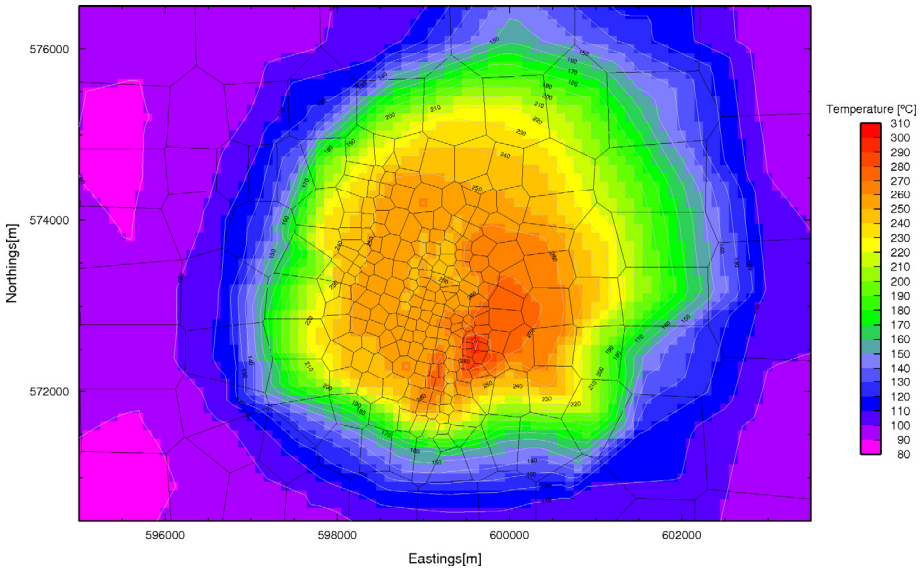

FIGURE 4: Temperature in layer D

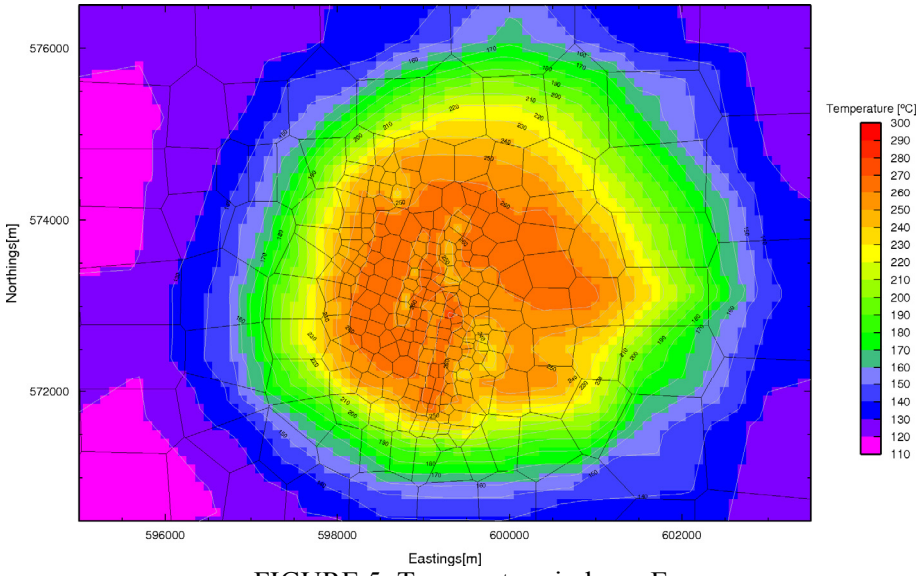

FIGURE 5: Temperature in layer E

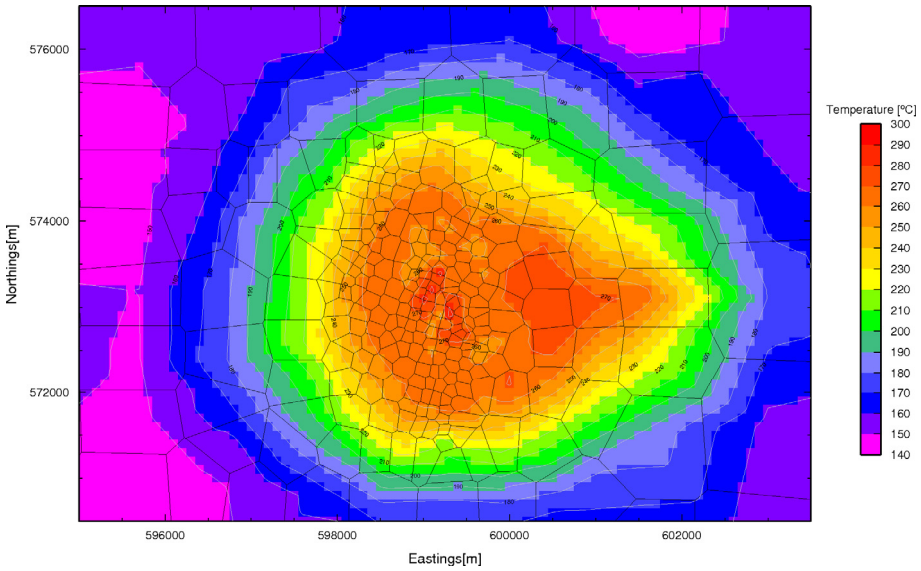

FIGURE 6: Temperature in layer F

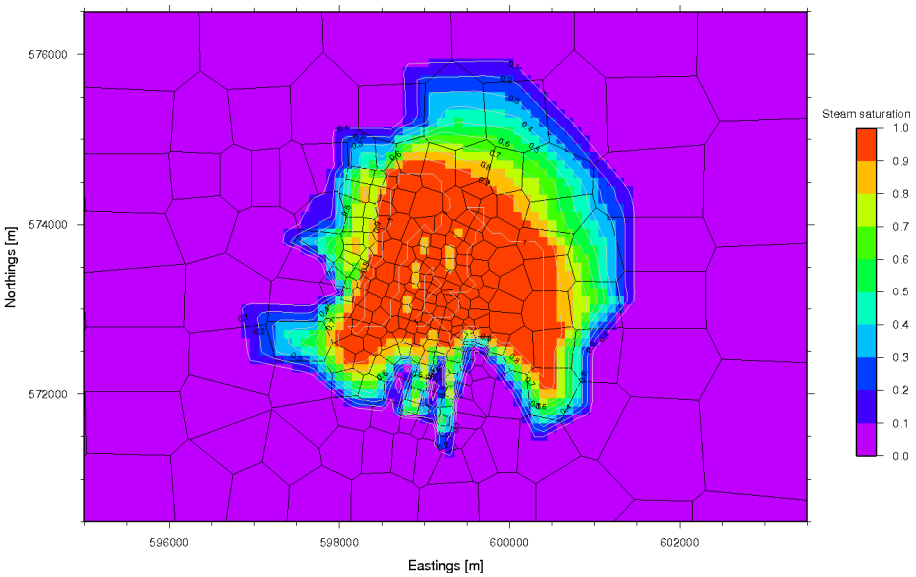

FIGURE 7: Steam saturation in layer D

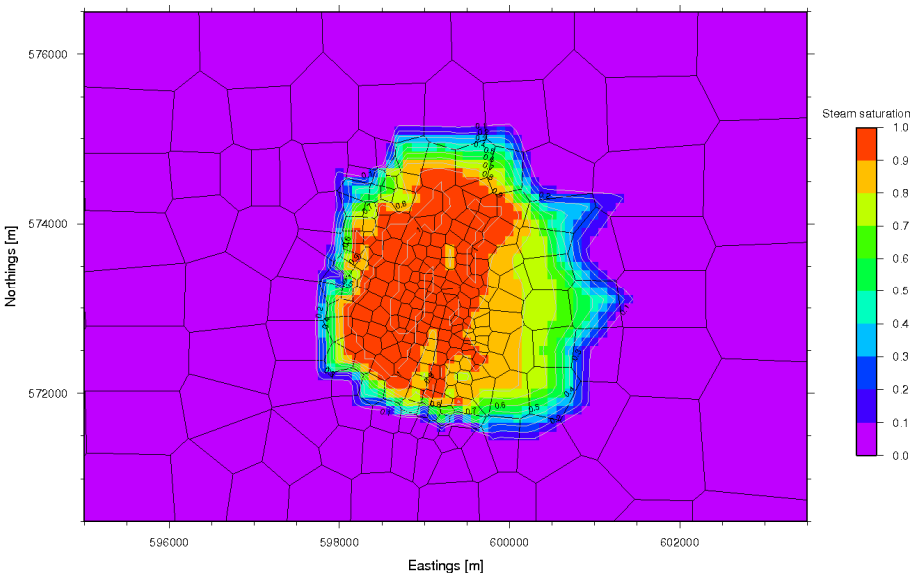

FIGURE 8: Steam saturation in layer E

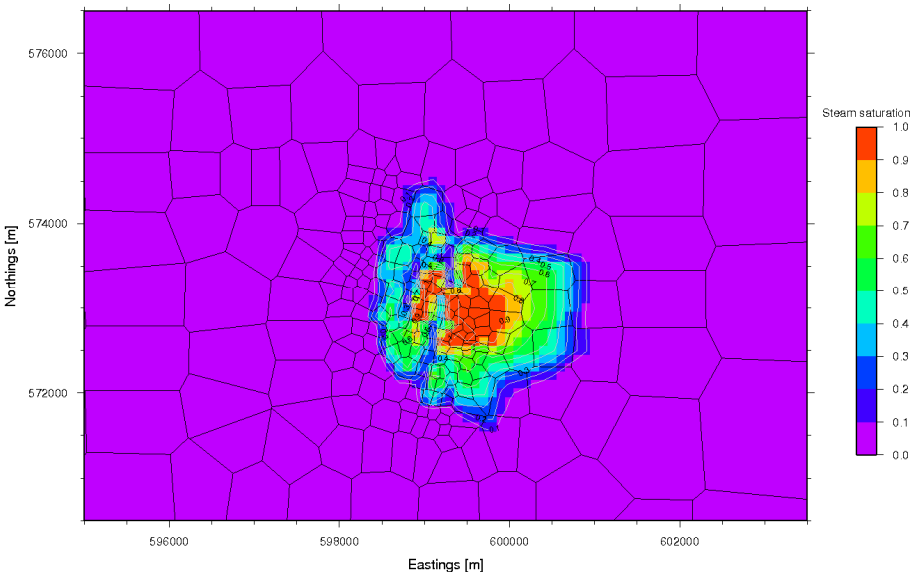

FIGURE 9: Steam saturation in layer F

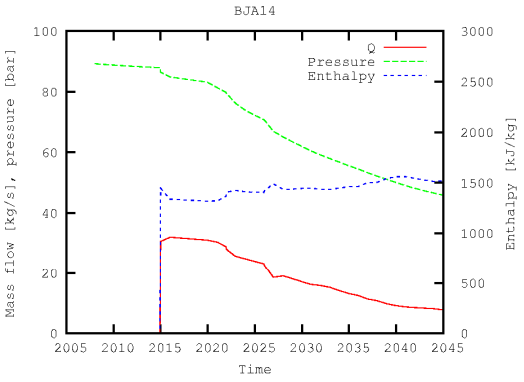
BJA14
Q
Pressure
Enthalpy
Mass flow [kg/s], pressure [bar]
Enthalpy [kJ/kg]
Time

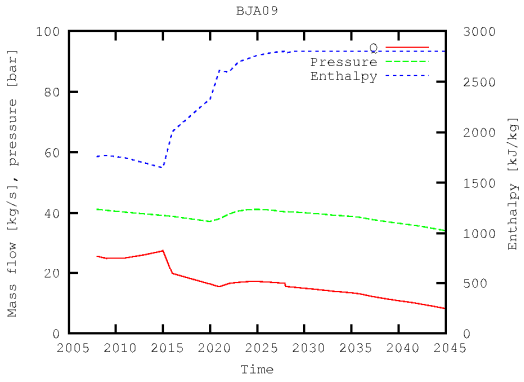
BJA09
Q
Pressure
Enthalpy
Mass flow [kg/s], pressure [bar]
Enthalpy [kJ/kg]
Time

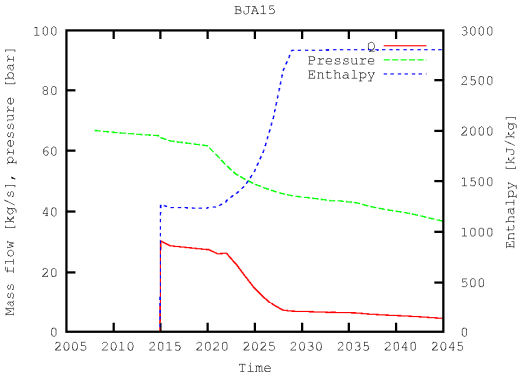
BJA15
Q
Pressure
Enthalpy
Mass flow [kg/s], pressure [bar]
Enthalpy [kJ/kg]
Time

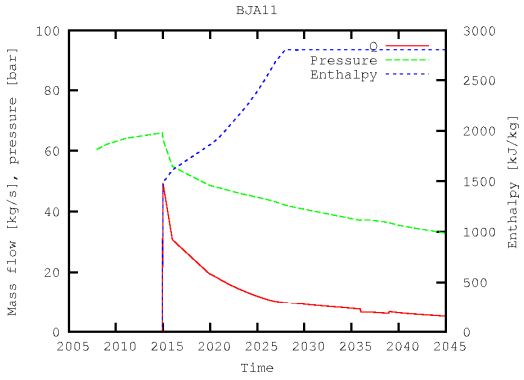
BJA11
Q
Pressure
Enthalpy
Mass flow [kg/s], pressure [bar]
Enthalpy [kJ/kg]
Time

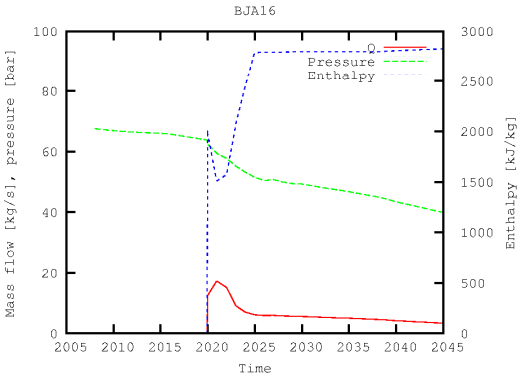
BJA16
Q
Pressure
Enthalpy
Mass flow [kg/s], pressure [bar]
Enthalpy [kJ/kg]
Time

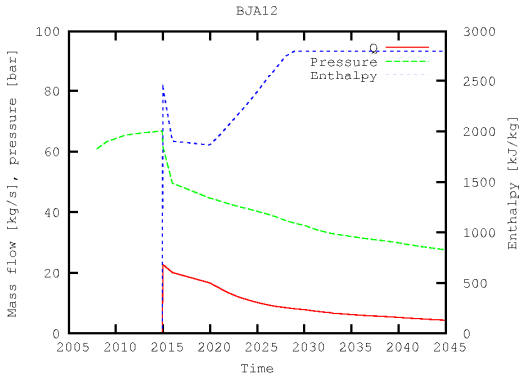
BJA12
Q
Pressure
Enthalpy
Mass flow [kg/s], pressure [bar]
Enthalpy [kJ/kg]
Time

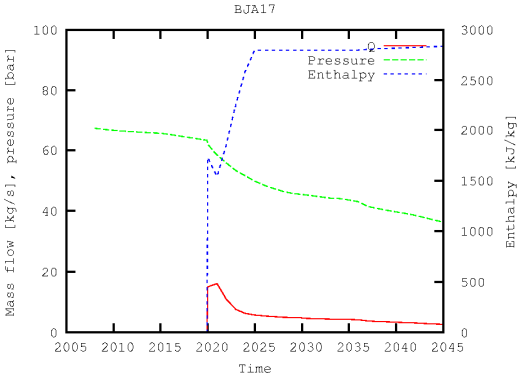
BJA17
Q
Pressure
Enthalpy
Mass flow [kg/s], pressure [bar]
Enthalpy [kJ/kg]
Time

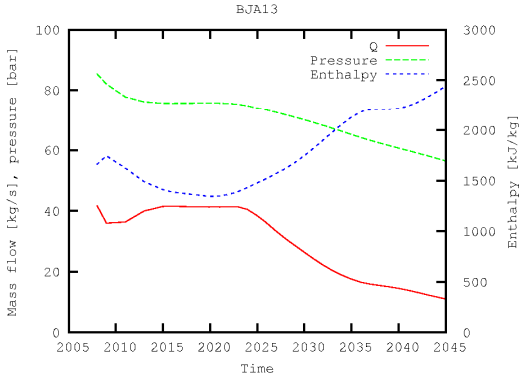
BJA13
Q
Pressure
Enthalpy
Mass flow [kg/s], pressure [bar]
Enthalpy [kJ/kg]
Time

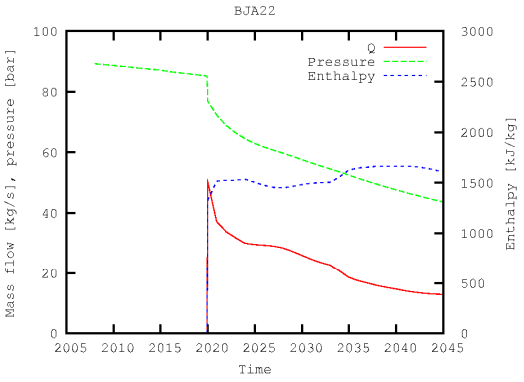
BJA22
Q
Pressure
Enthalpy
Mass flow [kg/s], pressure [bar]
Enthalpy [kJ/kg]
Time

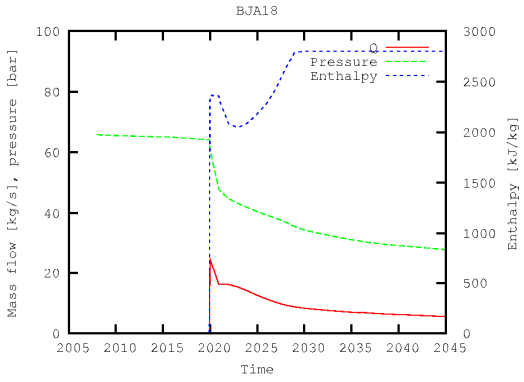
BJA18
Q
Pressure
Enthalpy
Mass flow [kg/s], pressure [bar]
Enthalpy [kJ/kg]
Time

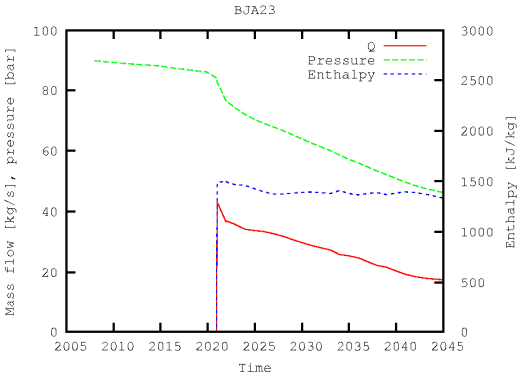
BJA23
Q
Pressure
Enthalpy
Mass flow [kg/s], pressure [bar]
Enthalpy [kJ/kg]
Time

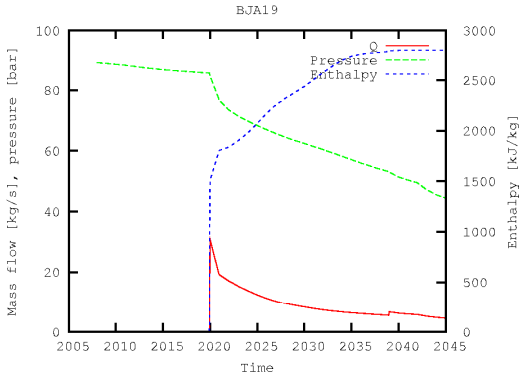
BJA19
Q
Pressure
Enthalpy
Mass flow [kg/s], pressure [bar]
Enthalpy [kJ/kg]
Time

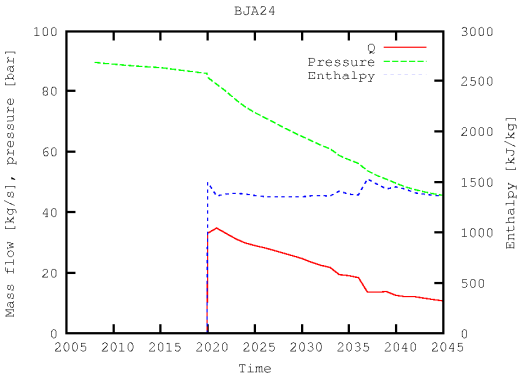
BJA24
Q
Pressure
Enthalpy
Mass flow [kg/s], pressure [bar]
Enthalpy [kJ/kg]
Time

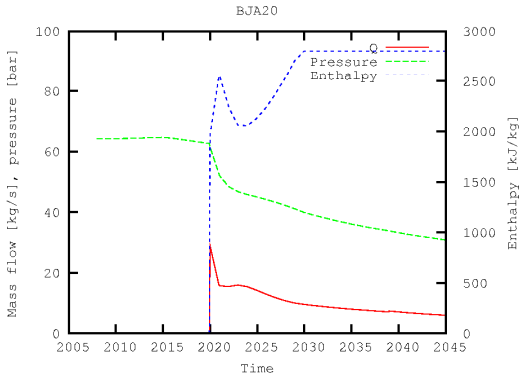
BJA20
Q
Pressure
Enthalpy
Mass flow [kg/s], pressure [bar]
Enthalpy [kJ/kg]
Time

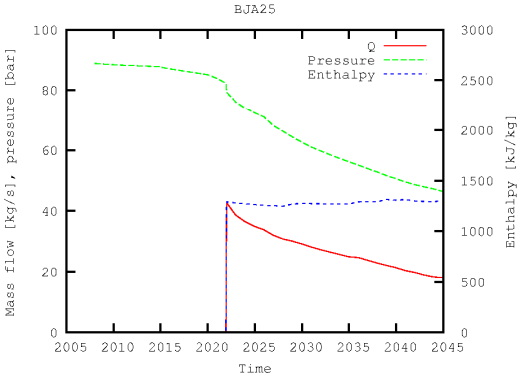
BJA25
Q
Pressure
Enthalpy
Mass flow [kg/s], pressure [bar]
Enthalpy [kJ/kg]
Time

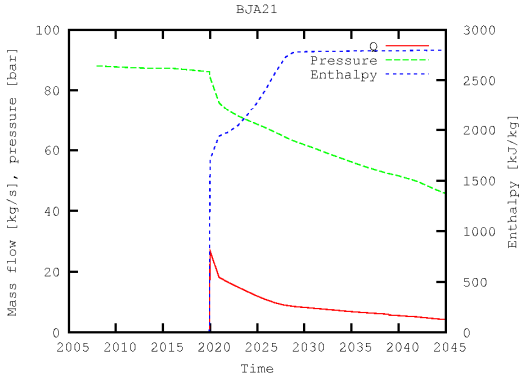
BJA21
Q
Pressure
Enthalpy
Mass flow [kg/s], pressure [bar]
Enthalpy [kJ/kg]
Time

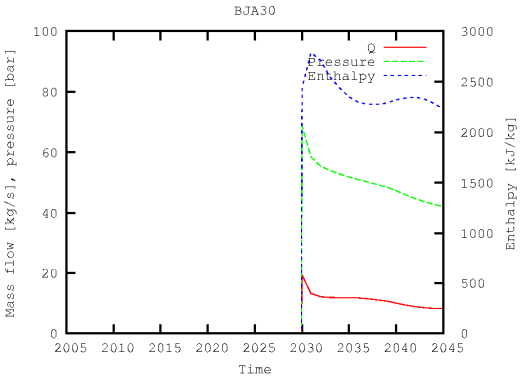
BJA30
Q
Pressure
Enthalpy
Mass flow [kg/s], pressure [bar]
Enthalpy [kJ/kg]
Time

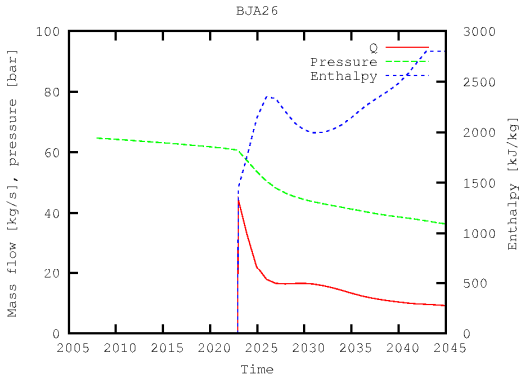
BJA26
Q
Pressure
Enthalpy
Mass flow [kg/s], pressure [bar]
Enthalpy [kJ/kg]
Time

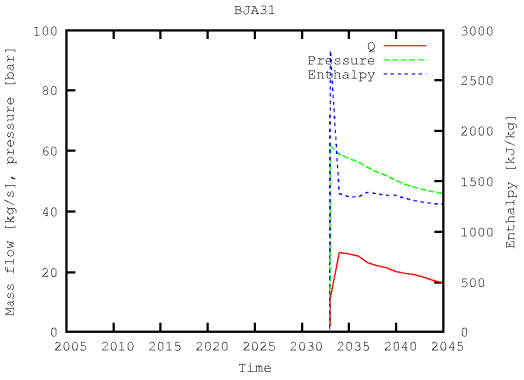
BJA31
Q
Pressure
Enthalpy
Mass flow [kg/s], pressure [bar]
Enthalpy [kJ/kg]
Time

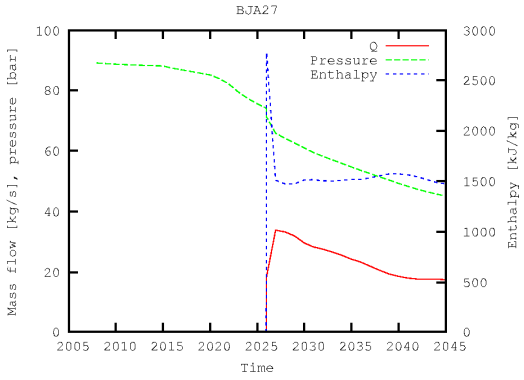
BJA27
Q
Pressure
Enthalpy
Mass flow [kg/s], pressure [bar]
Enthalpy [kJ/kg]
Time

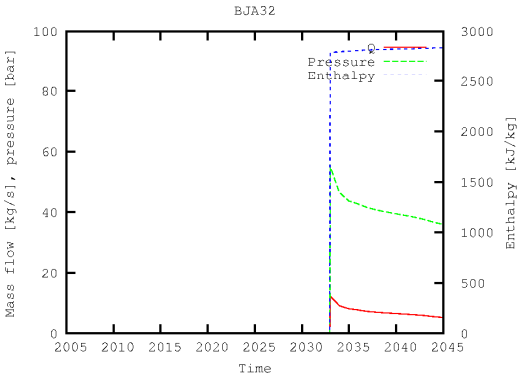
BJA32
Q
Pressure
Enthalpy
Mass flow [kg/s], pressure [bar]
Enthalpy [kJ/kg]
Time

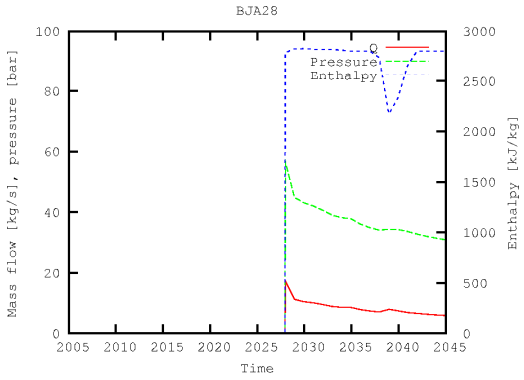
BJA28
Q
Pressure
Enthalpy
Mass flow [kg/s], pressure [bar]
Enthalpy [kJ/kg]
Time

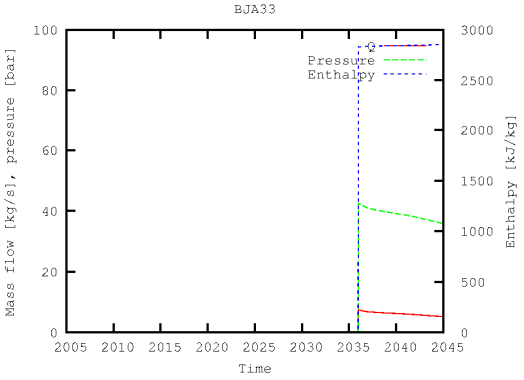
BJA33
Q
Pressure
Enthalpy
Mass flow [kg/s], pressure [bar]
Enthalpy [kJ/kg]
Time

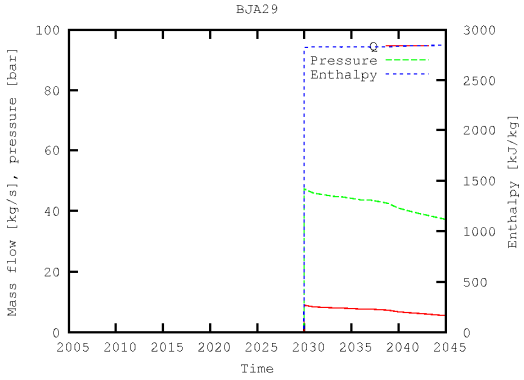
BJA29
Q
Pressure
Enthalpy
Mass flow [kg/s], pressure [bar]
Enthalpy [kJ/kg]
Time

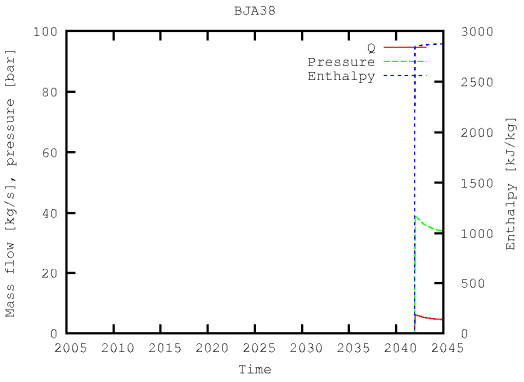
BJA38
Q
Pressure
Enthalpy
Mass flow [kg/s], pressure [bar]
Enthalpy [kJ/kg]
Time

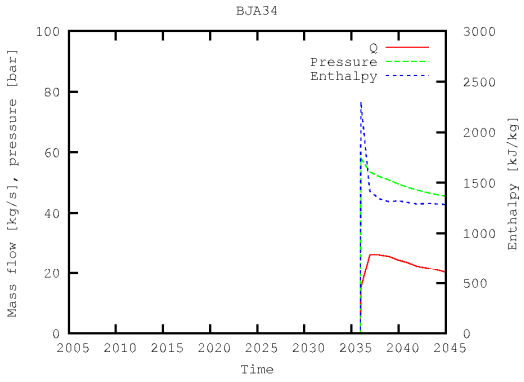
BJA34
Q
Pressure
Enthalpy
Mass flow [kg/s], pressure [bar]
Enthalpy [kJ/kg]
Time

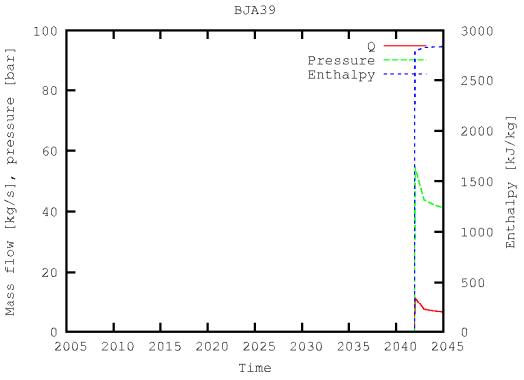
BJA39
Q
Pressure
Enthalpy
Mass flow [kg/s], pressure [bar]
Enthalpy [kJ/kg]
Time

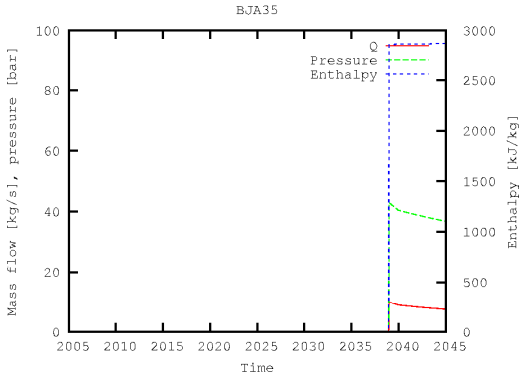
BJA35
Q
Pressure
Enthalpy
Mass flow [kg/s], pressure [bar]
Enthalpy [kJ/kg]
Time

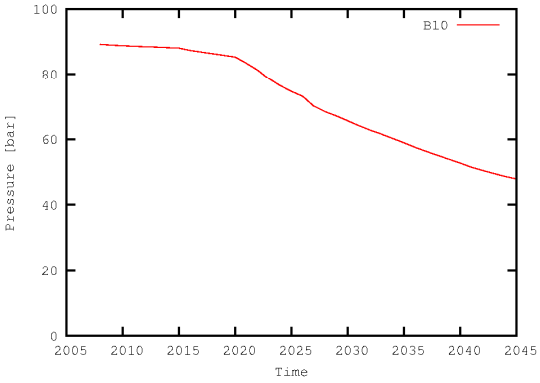
B10
Pressure [bar]
Time

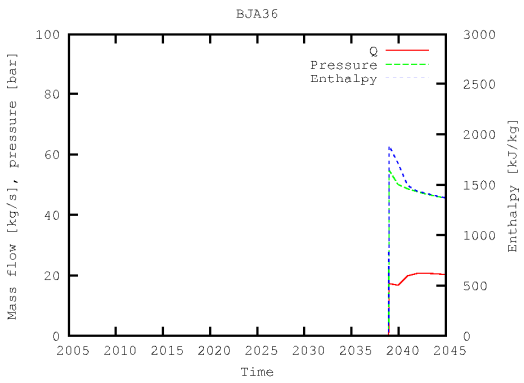
BJA36
Q
Pressure
Enthalpy
Mass flow [kg/s], pressure [bar]
Enthalpy [kJ/kg]
Time

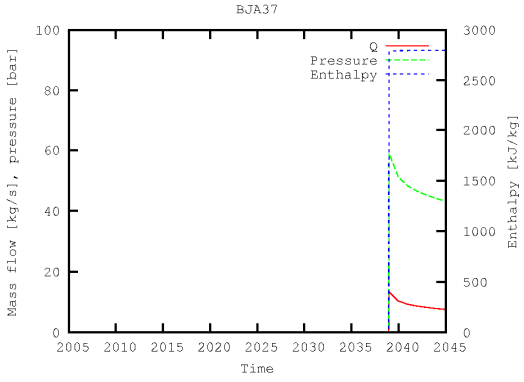
BJA37
Q
Pressure
Enthalpy
Mass flow [kg/s], pressure [bar]
Enthalpy [kJ/kg]
Time